

QUASAR-MODE FEEDBACK IN NEARBY TYPE 1 QUASARS: UBIQUITOUS KILOPARSEC-SCALE
OUTFLOWS AND CORRELATIONS WITH BLACK HOLE PROPERTIES

DAVID S. N. RUPKE

Department of Physics, Rhodes College, Memphis, TN 38112, USA; Research School of Astronomy and Astrophysics, The Australian
National University, Canberra, ACT 2611, Australia

KAYHAN GÜLTEKIN

Department of Astronomy, University of Michigan, Ann Arbor, MI 48109, USA

SYLVAIN VEILLEUX

Department of Astronomy and Joint Space-Science Institute, University of Maryland, College Park, MD 20742, USA

Resubmitted to ApJ 13 Sep 2017

ABSTRACT

The prevalence and properties of kiloparsec-scale outflows in nearby Type 1 quasars have been the subject of little previous attention. This work presents Gemini integral field spectroscopy of ten Type 1 radio-quiet quasars at $z < 0.3$. The excellent image quality, coupled with a new technique to remove the point spread function using spectral information, allow the fitting of the underlying host on a spaxel-by-spaxel basis. Fits to stars, line-emitting gas, and interstellar absorption show that 100% of the sample host warm ionized and/or cool neutral outflows with spatially-averaged velocities ($\langle v_{98\%} \rangle \equiv \langle v + 2\sigma \rangle$) of 200–1300 km s^{−1} and peak velocities (maximum $v_{98\%}$) of 500–2600 km s^{−1}. These minor-axis outflows are powered primarily by the central AGN, reach scales of 3–12 kpc, and often fill the field of view. Including molecular data and Type 2 quasar measurements, nearby quasars show a wide range in mass outflow rates ($dM/dt = 1$ to >1000 M_⊙ yr^{−1}) and momentum boosts [$(c \, dp/dt)/L_{\text{AGN}} = 0.01 - 20$]. After extending the mass scale to Seyferts, dM/dt and dE/dt correlate with black hole mass ($dM/dt \sim M_{\text{BH}}^{0.7 \pm 0.3}$ and $dE/dt \sim M_{\text{BH}}^{1.3 \pm 0.5}$). Thus, the most massive black holes in the local universe power the most massive and energetic quasar-mode winds.

Keywords: galaxies: evolution — quasars: general — quasars: supermassive black holes — ISM: jets and outflows

1. INTRODUCTION

An increasingly large body of evidence points to the presence of wide-angle, galaxy-scale outflows of gas and dust in the host galaxies of many nearby Type 2 quasars (Westmoquette et al. 2012; Rupke & Veilleux 2013a,b; Veilleux et al. 2013a; Ciccone et al. 2014; Harrison et al. 2014; McElroy et al. 2015; Bae et al. 2017; González-Alfonso et al. 2017; Wylezalek et al. 2017). These galactic winds, driven by the radiative and mechanical luminosity of the central engine, expel gas from the nucleus, and thereby from the sites of ongoing star formation and black hole accretion. Increasingly, this evidence comes from 3D observations at optical, near infrared, and millimeter wavelengths. Such data are ideal for distinguishing the wind from the host galaxy and constraining its structure and power source.

Quasar-mode feedback is an essential element of modern simulations and semi-analytic models of galaxy formation and evolution (e.g., Silk & Rees 1998; King 2003; Di Matteo et al. 2005; Somerville et al. 2008; Booth & Schaye 2009; Richardson et al. 2016). It may quench galaxies (Zubovas & King 2012; Wylezalek & Zakamska 2016; Pontzen et al. 2017), shape the stellar mass function (Somerville et al. 2008; Schaye et al. 2015; Taylor & Kobayashi 2015; Kaviraj et al. 2017), shape galaxy morphology (Dubois et al. 2016), impact the distribu-

tion of the Ly α forest (Gurvich et al. 2017), and regulate BH accretion (Hopkins et al. 2016; Volonteri et al. 2016). Though such outflows are harder to detect at high z than at low z , observations are beginning to suggest that quasar-driven winds could be common at the epochs of peak star formation and BH accretion (Perna et al. 2015; Brusa et al. 2015; Carniani et al. 2015, 2016; Leung et al. 2017). At high z but low AGN luminosity, the impact of winds may be less, though the data are sparse (Yesuf et al. 2017).

Mrk 231, the nearest Type 1 quasar, has become a poster-child for quasar-mode feedback (e.g., Fischer et al. 2010; Feruglio et al. 2010; Rupke & Veilleux 2011; Feruglio et al. 2015; Morganti et al. 2016). However, larger studies of kpc-scale outflows in Type 1 quasars are few. At low redshift ($z < 0.3$), one study of Type 1 quasars using integral field spectroscopy (IFS) has found extended narrow line regions (NLRs) photoionized by the central active galactic nucleus (AGN) but a paucity of galaxy-scale ionized outflows (Husemann et al. 2013, 2014). IFS studies of nearby Type 2 quasars, however, point to a very high incidence (as high as 80–100%) of ionized gas outflows with sizes of order 1–10 kpc (Rupke & Veilleux 2013b; Harrison et al. 2014; McElroy et al. 2015; Bae et al. 2017). This is a puzzling discrepancy in light of the AGN unification scheme, which suggests that the presence and properties of large-scale outflows should be identical in Type 1 and 2 quasars.

Table 1
Sample

Galaxy (1)	Other name (2)	z (3)	$\log(L_{\text{bol}}/L_{\odot})$ (4)	AGN Frac. (5)	$\log(M_{\text{BH}}/M_{\odot})$ (6)	σ (km s $^{-1}$) (7)	$\log[P_{\text{radio}}/(W \text{ Hz}^{-1})]$ (8)
I Zw 1	PG0050+124, F00509+1225	0.0608	12.07	$0.93^{+0.07}_{-0.10}$	$8.53^{+0.5}_{-0.5}$	188 ± 36	22.7
F05189–2524	...	0.04288	12.22	$0.71^{+0.29}_{-0.21}$	$8.32^{+0.5}_{-0.5}$	201 ± 64	23.1
F07599+6508	...	0.1483	12.58	$0.75^{+0.25}_{-0.39}$	$8.59^{+0.5}_{-0.5}$...	24.4
Mrk 231	F12540+5708	0.0422	12.60	$0.71^{+0.07}_{-0.07}$	$8.58^{+0.5}_{-0.5}$	233 ± 113	24.1
F13218+0552	...	0.2047	12.68	$0.83^{+0.17}_{-0.21}$	$8.55^{+0.5}_{-0.5}$...	23.8
F13342+3932	...	0.1797	12.49	$0.69^{+0.23}_{-0.24}$	$9.12^{+0.5}_{-0.5}$...	23.8
PG1411+442	...	0.0898	11.78	$1.00^{+0.00}_{-0.00}$	$8.54^{+0.46}_{-0.48}$	216 ± 31	22.3
PG1613+658	Mrk 876	0.12925	12.29	$0.82^{+0.11}_{-0.09}$	$8.34^{+0.47}_{-0.52}$...	23.1
PG1700+518	F17002+5153	0.2902	13.12	$0.80^{+0.16}_{-0.19}$	$8.79^{+0.52}_{-0.45}$...	24.8
F21219–1757	...	0.1127	12.17	$0.78^{+0.15}_{-0.13}$	$8.61^{+0.5}_{-0.5}$	121 ± 11	23.7

Note. — Column 3: Redshift, measured from the current data. Column 4: Galaxy bolometric luminosity (Veilleux et al. 2009b). Column 5: “AGN fraction”, or fraction of the bolometric luminosity of the galaxy due to an AGN (Veilleux et al. 2009b). The error bars reflect the full range of values derived from six mid-infrared diagnostics. Column 6: Black hole mass, taken from reverberation mapping (Bentz & Katz 2015) where possible, or *HST* photometric measurements otherwise (Veilleux et al. 2009a). Errors from reverberation mapping have the uncertainty in the virial coefficient f added in quadrature ($\delta f = 0.44$; Woo et al. 2010). Photometric error bars are from the scatter in the $M_{\text{BH}}-L_H$ relationship from which the masses were determined (Marconi & Hunt 2003). Column 7: Stellar velocity dispersions (Dasyra et al. 2006a, 2007; Rothberg et al. 2013; Grier et al. 2013). The large error bars for F05189–2524 and Mrk 231 are due to conflicting optical and infrared measurements (Dasyra et al. 2006a; Rothberg et al. 2013); the mean of the two measurements is shown, and the error bar is half the difference between the measurements. Column 9: 1.4 or 1.5 GHz radio power; from Barvainis & Lonsdale (1997) [PG1411+442], Carilli et al. (1998) [Mrk 231], Condon et al. (1990) [F05189–2524], Condon et al. (1998) [F07599+6508, F13218+0552, F13342+3932, F21219–1757], or Kukula et al. (1998) [I Zw 1, PG1613+658, PG1700+518].

Results at somewhat higher redshifts ($z \sim 0.6$) provide a more consistent picture. Large-scale ionized gas outflows are powerful and ubiquitous in both Types 1 and 2 (Liu et al. 2013a,b, 2014). The properties of these higher-redshift systems depend on the details of the removal of unresolved emission (Husemann et al. 2016), though clearly outflows are present in many cases.

The properties of quasar-mode AGN outflows (velocity, mass outflow rate) correlate with bolometric AGN luminosity (Sturm et al. 2011; Spoon et al. 2013; Veilleux et al. 2013a; Rupke & Veilleux 2013b; Cicone et al. 2014; Stone et al. 2016; González-Alfonso et al. 2017; Sun et al. 2017; Fiore et al. 2017). The gas depletion timescales are short in the most luminous AGN, suggesting that feedback is most effective in these systems (Cicone et al. 2014; González-Alfonso et al. 2017). Direct observational evidence for quasar-mode AGN feedback on star formation in galaxies is still inconclusive, though suggestive correlations exist (e.g., Farrah et al. 2012; Wylezalek & Zakamska 2016; Baron et al. 2017).

This study presents detailed observations of a nearby ($z < 0.3$) sample of Type 1 quasars observed with Gemini IFS. In particular, this sample has considerable ancillary data (§ 2.1), including black hole mass measurements, by which to study the dependence of outflow properties on black hole properties. Studies of large-scale outflows in Type 1 quasars have been neglected because of the impact on the data of the bright nuclear point source. § 2.3 details a new technique for spectral removal of the quasar point spread function (PSF), which allows fitting of stellar host properties on a spaxel-by-spaxel basis across the field of view (FOV). The subsequent fitting of strong emission lines and the Na I D absorption feature are described, and maps of the quasar and host galaxy, strong emission line properties, and absorption line properties are shown for each quasar. The ubiquitous presence and basic properties of the detected outflows are described in § 3.1; global properties are computed and compared

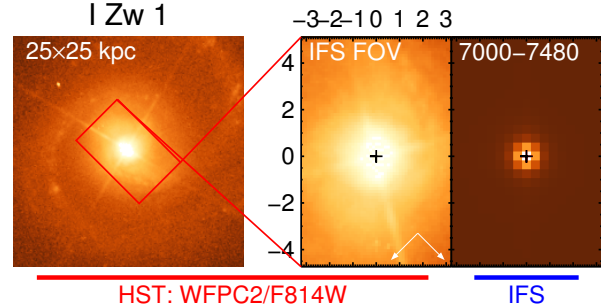


Figure 1. Images of each galaxy. (left) *HST* image showing the galaxy’s large-scale structure, labeled with the instrument and filter. The GMOS FOV is indicated by a red box. (middle) *HST* image cutout matching the GMOS FOV. When the nuclear point source is not saturated, the next panel to the right shows the same image smoothed with a Gaussian kernel to match the ground-based seeing and rebinned to the GMOS spaxel size. North and East are indicated by the white arrows. The black cross in each panel is the *HST* point used to co-register the *HST* and IFS images. This point can differ by up to $0''.03$ from the fitted centers of the smoothed *HST* or GMOS data cubes, which are shown as red crosses. Differences result from the host contribution to the ground-based PSF (in F05189–2524, F13218+0552, and F13342+3932; § 2.3.1). (right) GMOS image, summed over the range (in Å, listed in the panel) that overlaps the *HST* filter transmission profile. The black cross is the location of the quasar, determined from unsaturated *HST* images (F05189–2524, F13218+0552, and F13342+3932) or from the quasar PSF image extracted from the IFS fitting (in the other cases; see Figure 5). The axes give galactocentric coordinates in kpc. The unsmoothed *HST* scaling is asinh (Lupton et al. 1999). The smoothed *HST* and GMOS scales are linear. (The complete figure set (10 images) is available.)

to black hole properties in §§ 3.2–3.3. The wind power source is analyzed in § 4.1, and the implications for wind models and AGN feedback are discussed in §§ 4.2–4.3. § 5 summarizes the paper.

2. THE DATA

2.1. Sample

Table 2
Observations

Galaxy (1)	PID (2)	Dates (3)	Grating (4)	t_{exp} (5)	PSF (6)	Range (7)	PA (8)	FOV (9)
I Zw 1	GN-2015A-DD-9	10jul2015	B600	4×1800s	0''.6	4610–7490 Å	225°	5''.1×7''.8
F05189–2524	GS-2011B-Q-64	03dec,13dec,31dec2011	B600	6×1800s	0''.6	4560–7430 Å	0°	5''.2×5''.0
F07599+6508	GN-2007A-Q-12	08apr2007	R831	3×1440s	0''.5	6520–8640 Å	180°	3''.0×4''.5
Mrk 231	GN-2013A-Q-51	16jun,17jun2013	B600	5×1800s	0''.8	5620–6950 Å	215°	6''.3×7''.5
F13218+0552	GN-2012A-Q-15	02apr,08apr2012	B600	8×1800s	0''.8	5340–8230 Å	315°	3''.9×4''.5
F13342+3932	GN-2012A-Q-15	17may2012	B600	8×1800s	0''.6	5340–8230 Å	313°	4''.2×5''.1
PG1411+442	GN-2015A-DD-9	22jul,23jul2015	B600	4×1800s	0''.8	4610–7480 Å	335°	3''.9×4''.5
PG1613+658	GN-2012A-Q-15	22apr,24apr2012	B600	6×1800s	0''.9	5340–8220 Å	135°	5''.1×7''.8
PG1700+518	GN-2003B-C-5	23sep2003	B600	2×1800s	0''.7	4320–7190 Å	14°	3''.0×4''.2
F21219–1757	GS-2005B-Q-50	09sep2005	B600	2×1800s	0''.9	4060–6860 Å	0°	2''.7×4''.5

Note. — Column 2: Program ID. Column 3: UT dates of observations (in DDmmYYYY format). Column 4: Grating. Column 5: Number of exposures × length of each exposure. Column 6: FWHM of quasar PSF in the data cube, except for F05189–2524, in which the number is an estimate of the seeing from observing logs. Column 7: Observed wavelength range of combined data cube. Column 8: E of N position angle of IFU during observations. Column 9: Size of combined FOV.

The present low-redshift sample ($z < 0.3$) was selected from the larger QUEST sample (Quasar and ULIRG Evolution Study; [Veilleux et al. 2006](#); [Schweitzer et al. 2006](#); [Netzer et al. 2007](#); [Veilleux et al. 2009a,b](#)). The QUEST sample consists of local ultraluminous infrared galaxies (ULIRGs) from the 1 Jy sample ([Kim & Sanders 1998](#)) and optically-selected Palomar-Green quasars ([Schmidt & Green 1983](#)). Properties of the Gemini subsample of QUEST are listed in Table 1. The heterogeneous selection of this subsample was due to the combination of three archival datasets with seven observations designed to meet the current science goals. For the sources observed for this program, selection was based on a combination of observability, proximity (to maximize spatial resolution), and diversity in galaxy properties.

All of the quasars in the sample are traditional Type 1s except for F05189–2524. However, this quasar has a broad line region (BLR) observed in the near infrared ([Veilleux et al. 1999b](#)); thus a portion of the BLR is unobstructed by the obscuring medium. Three are broad-absorption-line (BAL) quasars: F07599+6508, Mrk 231, and PG1700+518. All three are also low-ionization BALs (LoBALs), with broad absorption observed in Mg II ([Smith et al. 1995](#); [Turnshek et al. 1997](#); [Veilleux et al. 2016](#)) and Na I D ([Boroson & Meyers 1992](#); [Rupke et al. 2005a](#)).

The average value of L_H/L_H^* in the sample is 2.8 ([Veilleux et al. 2006, 2009b](#)), which corresponds to a halo mass of $\log(M_{\text{halo}}/M_\odot) \sim 12.8$ based on abundance matching ([Moster et al. 2013](#)) and a baryon fraction $f_b = 0.17$. Thus, the sample probes well above the halo mass at which the stellar-to-halo mass fraction peaks; i.e., the region in which AGN feedback is thought to be necessary in quenching star formation (e.g., [Somerville et al. 2008](#)).

2.2. Observations and Data Reduction

The ten quasars were observed with the Integral Field Unit in the Gemini Multi-Object Spectrograph (GMOS; [Allington-Smith et al. 2002](#); [Hook et al. 2004](#)) on the Gemini North and South telescopes. Details of each observation are listed in Table 2. All observations used the 1-slit mode, and 9/10 used the B600 grating; this

setup yields an approximately constant resolution element of full width at half-maximum (FWHM) 1.5 Å. All observations were dithered to increase the FOV. The resulting total FOV is centered on the quasar in each case except for PG1700+518. The wavelength range for the typical setup included most strong emission lines ($H\alpha$, $H\beta$, [O III] 4959, 5007 Å, [N II] 6548, 6583 Å, [S II] 6717, 6731 Å, [O I] 6300, 6364 Å). For two archival setups (PG1700+518 and F21219–1757) and a new Mrk 231 observation, the grating was tilted blueward, including only [O II] 3727, 3729 Å through [O III] 4959, 5007 Å. All cubes but one (PG1700+518) also included the Na I D 5890, 5896 Å absorption doublet. Image quality of the reduced data cubes, as determined from a PSF fit (§ 2.3.1), was 0''.5–0''.9. (Separate exposures for a given quasar were convolved to match the worst seeing in the data.)

The Gemini IRAF package (v1.12) was used to reduce the data, supplemented by revision 114 of the IFUDR GMOS package and IFSRED ([Rupke 2014a](#)). Data cubes were visualized with QFitsView ([Ott 2012](#)). In addition to the steps described in [Rupke & Veilleux \(2013b\)](#) and [Rupke & Veilleux \(2015\)](#), scattered light was removed from the flat fields and the data prior to extraction. Because of the strong nuclear point source in most cubes, scattered light removal was crucial for accurate continuum and emission-line fitting.

Scattered light could not be completely removed from two systems: I Zw 1 and PG1411+442. The dithering strategy adopted in these cases put the quasar near the edge of the field of view along the short axis of the IFU. Consequently, the quasar light was concentrated near either the edge or center of fiber blocks in the raw data. Because scattered light subtraction relies on extrapolating from interblock regions, the off-centered quasar light in the blocks meant that this extrapolation was imperfect. The result is an under-subtraction of the scattered light, and is visible as a vertical stripe emerging from the point source in the reconstructed host galaxy image (§ 2.3.1).

Each final data cube was rebinned to a spaxel size of 0''.3×0''.3, which balanced sensitivity and sampling of the seeing disk (the sampling was Nyquist or better in almost

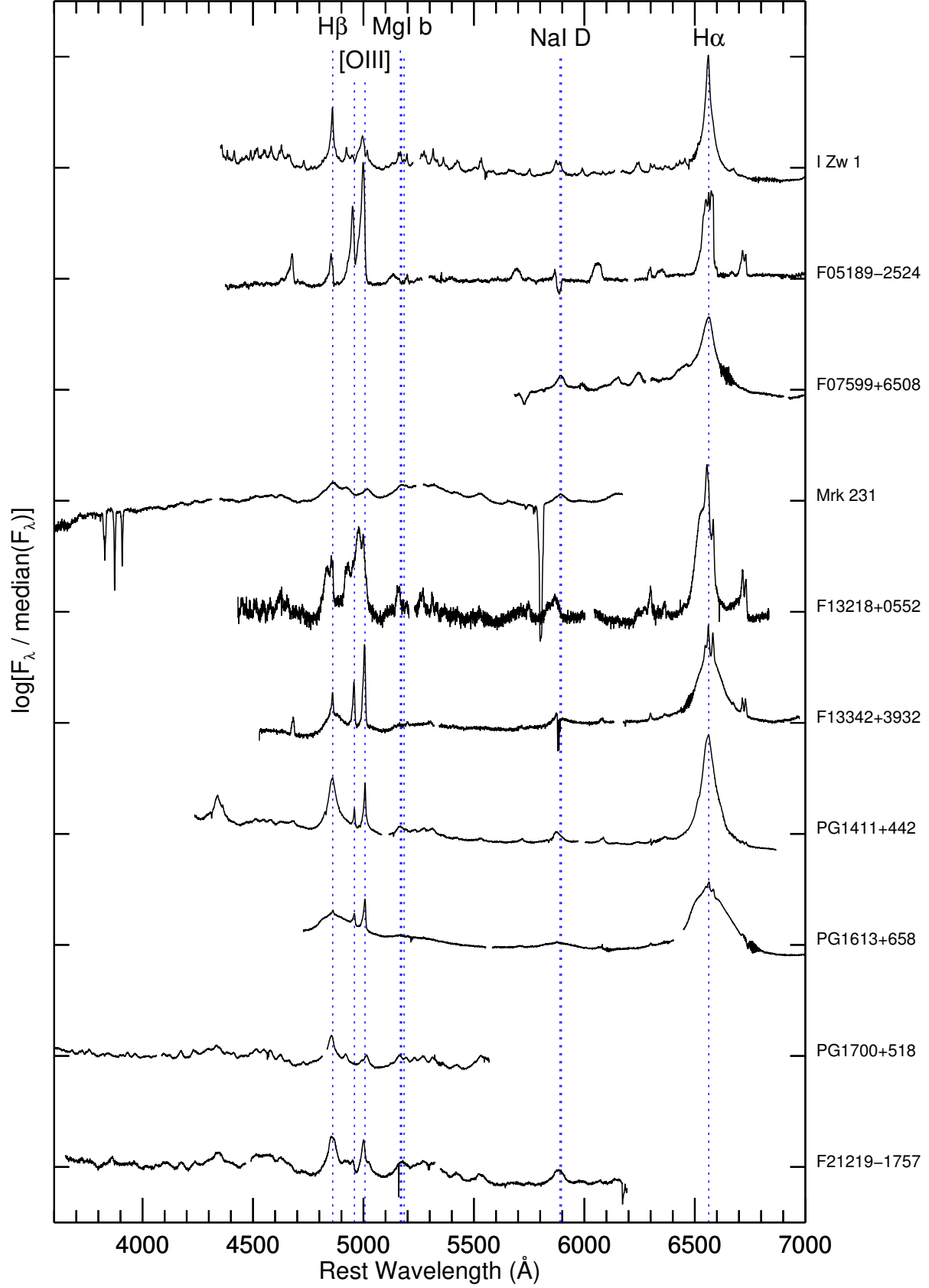


Figure 2. Quasar spectra, derived from the central spaxel in the $0''.1$ spaxel data cubes. These are used as fit inputs, and are represented by I_{quasar}^0 in § 2.3.1 and equation 2.

every case).

2.3. Data Analysis

The spectrum in each spaxel was modeled with IFS-FIT (Rupke 2014b), which utilizes PPXF (Cappellari 2012) for starlight fitting and MPFIT (Markwardt 2012) for other continuum and emission line fitting. In brief, IFSFIT masks emission line regions, fits the continuum, and then simultaneously fits all emission lines in the continuum-subtracted spectrum. Subsequently, interstellar absorption lines are modeled.

2.3.1. Separation of Quasar and Host Galaxy Light

In most of this sample, the luminous AGN, or quasar, outshines the host galaxy. *HST* *H*-band data show that the quasar light fraction is 0.45–0.89 (Veilleux et al. 2006, 2009a). Heavy nuclear obscuration in F05189–2524, and to a lesser degree in F13218+0552 and F13342+3932, lower this fraction in the optical. At *HST* resolution, the quasar contributes 45% of the *H*-band light of F05189–2524 but <1% of its *I*-band light (Kim et al. 2013), consistent with the appearance of a BLR only in the near infrared (Veilleux et al. 1999b). On visual inspection of optical *HST* images (Figure 1) F13218+0552 and F13342+3932 show a small quasar light fraction, while six other quasars dominate their hosts. The final quasar, F21219–1757, has no optical *HST* image.

To visually compare *HST* and IFS data, the cubes were summed over wavelengths that overlap with the *HST* filter range (Figure 1). For the three systems with small quasar light fraction in the optical, the *HST* images were also Gaussian-smoothed to match the seeing.

In 9/10 cases, the peak IFS spaxel in 0".1 sampling represents a pure quasar spectrum to very good approximation (Figure 2). For F05189–2524, the peak spaxel traces an unresolved point source at optical ground-based resolution (Veilleux et al. 2002, 47% contribution to total light), but it is a combination of quasar light and starlight. It has very strong, high-ionization emission lines from the NLR that are either spatially unresolved or dominated by an unresolved component (including [O III] 4959, 5007 Å, He II 4686 Å, [Fe VII] 5159 Å, [Fe VII] 5721 Å, [Fe VII] 6087 Å, and [Fe X] 6375 Å; Farrah et al. 2005).

A multi-step process is adopted to fit the quasar and host galaxy in each spaxel. This iterative approach is necessary for three reasons.

First, subtracting the starlight accurately is crucial for properly constraining the underlying interstellar component of the Na I D absorption feature. It also produces more accurate recombination-line fluxes by accounting properly for Balmer absorption. In dusty, infrared-luminous galaxies where Na I D is strong, the stellar continuum subtraction is much less important because interstellar absorption dominates the feature. However, in many of these (less dusty) quasars, the stellar and interstellar Na I D absorption are comparable in strength.

Second, simultaneously fitting the quasar, starlight, and emission lines was technically infeasible. The starlight must be fit in PPXF (to allow the velocity and dispersion of the stellar spectrum to be free parameters). In principle the quasar spectrum could also be input into PPXF as a sky spectrum, since the sky spectrum

remains unconvolved with the fitted stellar velocity dispersion. However, PPXF uses Legendre polynomials to correct the stellar fit for imperfectly calibrated data. Linear combinations of polynomials are too flexible because they have the freedom to produce negative continuum values. This is especially a problem in spaxels where the host galaxy contribution is uncertain due to domination by quasar light or the total flux is very low.

Third, there is a range of sensitivity in this dataset. This is partly by design – galaxies were chosen over a range of redshifts. It is also by accident – galaxies that were targeted for this program were observed $\sim 2\times$ longer than galaxies observed for different purposes and retrieved from the archive. There is also intrinsic variation in the strength of the host galaxy starlight compared to the quasar. Galaxies with very high signal-to-noise (S/N) in the stellar continuum (e.g., F05189–2524 and Mrk 231) can be fit using multiple stellar templates. However, the composition of the stellar population could not be constrained on a spaxel-by-spaxel basis in most of the sample. In one system (F07599+6508), the stellar population could not be constrained even in the spatially-integrated spectrum.

A description of the fitting process follows, and it is illustrated in Figure 3. As discussed above, all fitting is performed with IFSFIT. IFSFIT calls PPXF when fitting starlight spectra with stellar population synthesis (SPS) models. In the discussion below, “total” refers to a complete spectrum with all physical components.

1. Fit total spectra with quasar + exponential starlight model + emission lines. Each spaxel n is fit with the sum of a scaled quasar spectrum, a starlight model, and emission lines:

$$I_{\text{total}}^n = I_{\text{quasar}}^n + I_{\text{starlight, exp.model}}^n + I_{\text{emission}}^n. \quad (1)$$

Emission lines are first masked; the quasar and starlight continuum components are fit simultaneously using MPFIT; the continuum is subtracted from the data; and finally the emission lines are fit with MPFIT. The starlight model and quasar scaling in each spaxel are each the sum of four exponentials:

$$I_{\text{total}}^n = \sum_{i=1}^4 I_i^n I_{\text{quasar}}^0 + \sum_{j=1}^4 I_j^n + I_{\text{emission}}^n, \quad (2)$$

where I_{quasar}^0 is the nuclear quasar spectrum (Figure 2); the exponentials are

$$\begin{aligned} I_1^n &= a_1^n e^{-b_1^n \bar{\lambda}} \\ I_2^n &= a_2^n e^{-b_2^n (1-\bar{\lambda})}, \\ I_3^n &= a_3^n (1 - e^{-b_3^n \bar{\lambda}}), \text{ and} \\ I_4^n &= a_4^n (1 - e^{-b_4^n (1-\bar{\lambda})}); \end{aligned}$$

$a_i^n \geq 0$; $b_i^n \geq 0$; $\bar{\lambda} \equiv \frac{\lambda - \lambda_{\min}}{\lambda_{\max} - \lambda_{\min}}$; and $[\lambda_{\min}, \lambda_{\max}]$ is the fit range. Exponentials are used because they are monotonic and can be made positive-definite. The four exponentials allow for all combinations of concave/convex and monotonically increasing/decreasing. Physically, the quasar multipliers correct for spatially-varying errors due to im-

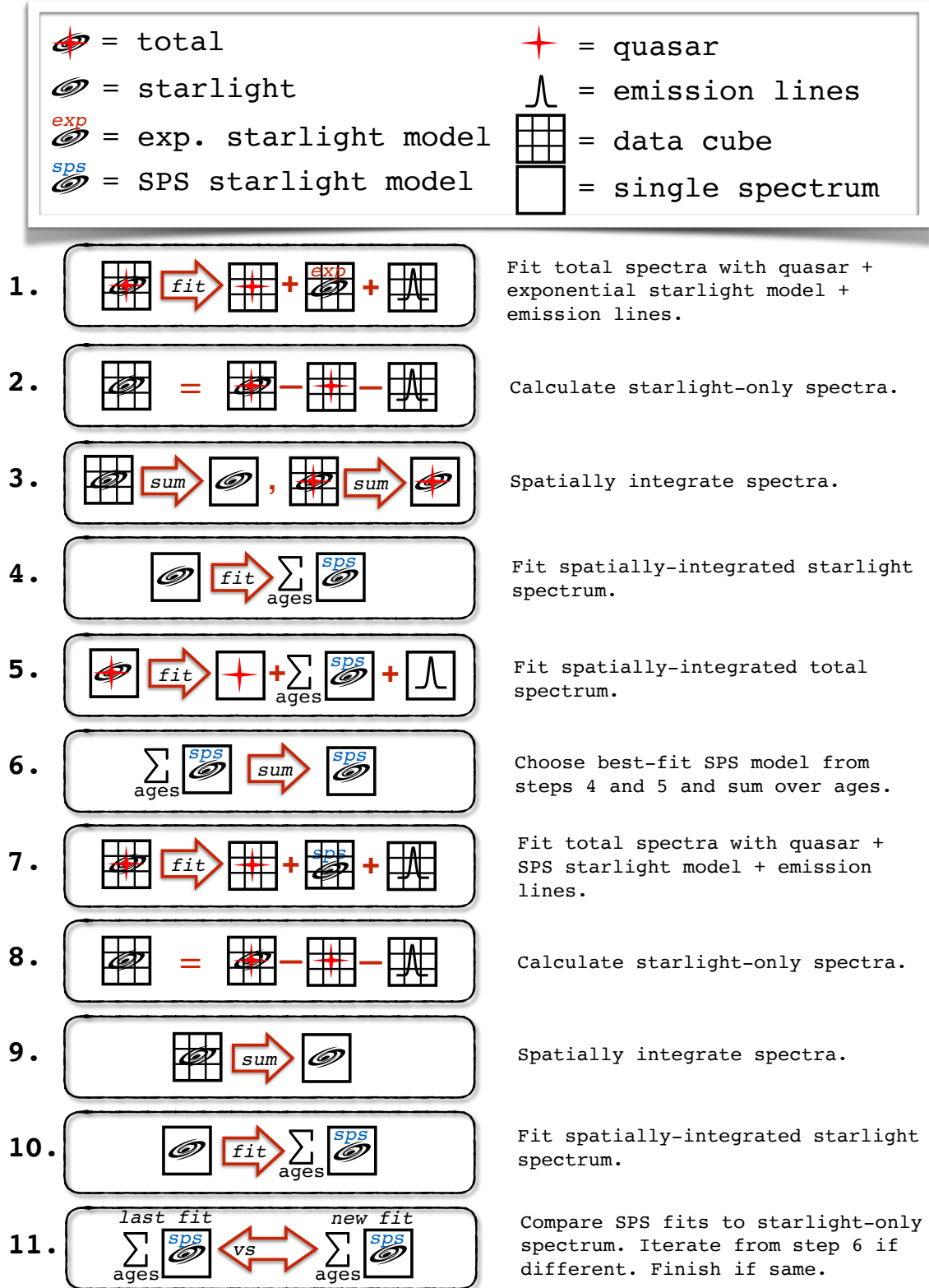


Figure 3. Illustration of the procedure for separating the quasar and host galaxy light (§ 2.3.1).

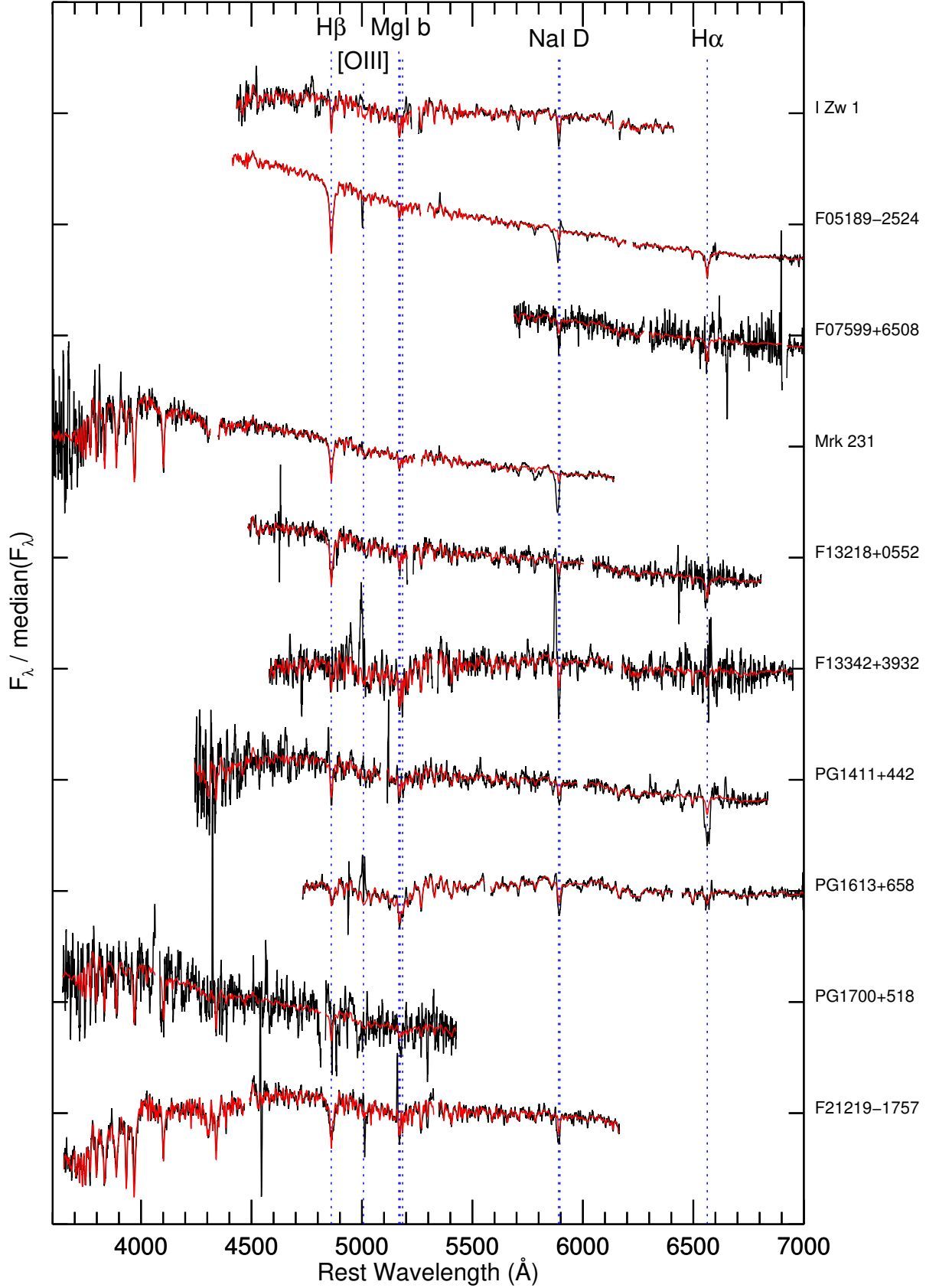


Figure 4. Stellar population synthesis fits (red) to starlight spectra (black) that have been spatially-integrated over the IFS FOV. The quasar light and emission lines have been removed (§ 2.3.1). The data is smoothed by a 10-pixel boxcar to facilitate comparison with the fits.

perfect scattered light removal (or other calibration effects) and for the $\lambda^{-0.2}$ dependence of PSF size on atmospheric seeing. For a Gaussian PSF, the latter effect produces an exponential of the form $e^{-C\lambda^{0.8}}$, which is similar to I_1 .

2. Calculate starlight-only spectra. The quasar and emission-line components are subtracted from the total spectrum in each spaxel. The result is a data spectrum including only starlight:

$$I_{\text{starlight}}^n = I_{\text{total}}^n - I_{\text{quasar}}^n - I_{\text{emission}}^n. \quad (3)$$

3. Spatially integrate spectra. The starlight and total spectra are spatially integrated:

$$I_{\text{starlight}} = \sum_n I_{\text{starlight}}^n \text{ and} \\ I_{\text{total}} = \sum_n I_{\text{total}}^n.$$

4. Fit spatially-integrated starlight spectrum. The spatially-integrated starlight spectrum is fit with the [González Delgado et al. 2005](#) high-resolution SPS models and Legendre polynomials P_l :

$$I_{\text{starlight}} = I_{\text{starlight, SPS model}} + I_{\text{Leg. poly.}} \\ = \sum_t A^t I_{\text{starlight, SPS model}}^t + \sum_{l=0}^{l_{\text{max}}} B_l P_l.$$

The models vary in age, t , but assume Solar metallicity ([Rupke et al. 2008](#)). A Legendre polynomial of order $l_{\text{max}} = 20 - 50$ (small compared to ~ 6200 pixels in wavelength) is used in order to account for imperfections in calibration (e.g., scattered light subtraction) or in the PSF subtraction. These imperfections appear as very shallow, broad ripples in the continuum or as higher-frequency edge effects.

5. Fit spatially-integrated total spectrum. This fit proceeds as in steps 1, 2, and 4, but involves only a single invocation of IFSFIT. After masking emission lines, IFSFIT fits the continuum component of the spatially-integrated total spectrum with a scaled quasar plus exponential model for starlight as in step 1:

$$I_{\text{total,cont.}} = I_{\text{quasar}} + I_{\text{starlight, exp.model}}. \quad (4)$$

IFSFIT then calculates the starlight spectrum as in step 2:

$$I_{\text{starlight}} = I_{\text{total,cont.}} - I_{\text{quasar}}, \quad (5)$$

and fits the result with the sum of SPS and Legendre components as in step 4 above. Finally, the emission lines are unmasked and fit. The endpoint of this fit is represented by

$$I_{\text{total}} = I_{\text{quasar}} + I_{\text{starlight, SPS model}} + I_{\text{emission}}. \quad (6)$$

6. Choose best-fit SPS model from steps 4 and 5 and sum over ages. The fit (from either of the previous two steps) that shows the minimum contribution

from a polynomial is typically chosen. The best-fit SPS model is summed over ages t , ignoring the polynomial component:

$$I_{\text{starlight, SPS model}}^{\text{fixed}} = \sum_t A^t I_{\text{starlight, SPS model}}^t. \quad (7)$$

The “fixed” superscript indicates that this starlight model will not vary in subsequent steps.

7. Fit total spectra with quasar + SPS starlight model + emission lines. Each spaxel is fit as in step 1, but with the (fixed) SPS starlight model from step 6 replacing the exponential model:

$$I_{\text{total}}^n = I_{\text{quasar}}^n + C^n I_{\text{starlight, SPS model}}^{\text{fixed}} + I_{\text{emission}}^n. \quad (8)$$

As in step 5, IFSFIT is invoked only once, but there are intermediate steps (within SPS) before the SPS model is fit. In particular, the entire spectrum in each spaxel is first fit with the quasar, an exponential starlight model, and emission lines. A starlight spectrum is then calculated by removing the best-fit quasar and emission components from the total spectrum, and the starlight-only spectrum is refit with the SPS model. The fixed SPS model, $I_{\text{starlight, SPS model}}^{\text{fixed}}$, is allowed to vary from spaxel to spaxel in velocity, dispersion, and normalization (C^n). The stellar population is thus implicitly assumed to be unvarying across the relatively small GMOS FOV.

8. Calculate starlight-only spectra. Repeat step 2, using the new fit from step 7. The new starlight-only spectrum can differ from the first one because the first fit (step 1) does not properly account for stellar absorption lines, which in turn affects how the emission lines are removed from the total spectrum. The new fit of each spaxel (step 7) accounts for stellar absorption lines.
9. Spatially integrate starlight spectrum. Repeat step 3 using the new starlight spectrum from step 8.
10. Fit spatially-integrated starlight spectrum. Repeat step 4, but now using the new spatially-integrated starlight spectrum from step 9.
11. Compare SPS fits to starlight-only spectrum. Compare the results of steps 4 and 10 by calculating the fractional contribution to the total light of starlight in four age groups. If there is a $\geq 10\%$ difference in any group, begin again with the new SPS model, starting from step 6. Iterate until the current SPS model differs from the previous by $< 10\%$ in each of the four age groups.

For most objects, the first iteration of steps 1–10 resulted in convergence. For three objects, a second iteration was required.

The final SPS fits to the spatially-integrated starlight spectra are shown in Figure 4, and the percent contributions (by flux in the fitted wavelength range) of the stellar populations in four age bins are given in Table 3. The use of the [González Delgado et al. \(2005\)](#) templates imposes an upper rest wavelength limit of 7000 Å to the

Table 3
Stellar Population Synthesis Fits

Galaxy (1)	Ages (Gyr)				poly (6)
	≤ 0.01 (2)	0.01–0.1 (3)	0.1–1 (4)	> 1 (5)	
I Zw 1	38	0	0	23	39
F05189–2524	38	1	36	3	22
F07599+6508	46	0	0	19	35
Mrk 231	59	0	13	11	17
F13218+0552	22	0	34	13	31
F13342+3932	0	0	0	39	51
PG1411+442	26	0	1	26	47
PG1613+658	0	0	0	58	42
PG1700+518	37	0	0	4	59
F21219–1757	6	0	42	19	33

Note. — Columns 2–5: Percent contribution to total flux (in the wavelength range of the fits to integrated host galaxy spectra) from Solar metallicity stellar populations of different ages (§ 2.3.1). Column 6: Percent contribution from linear combination of Legendre polynomials.

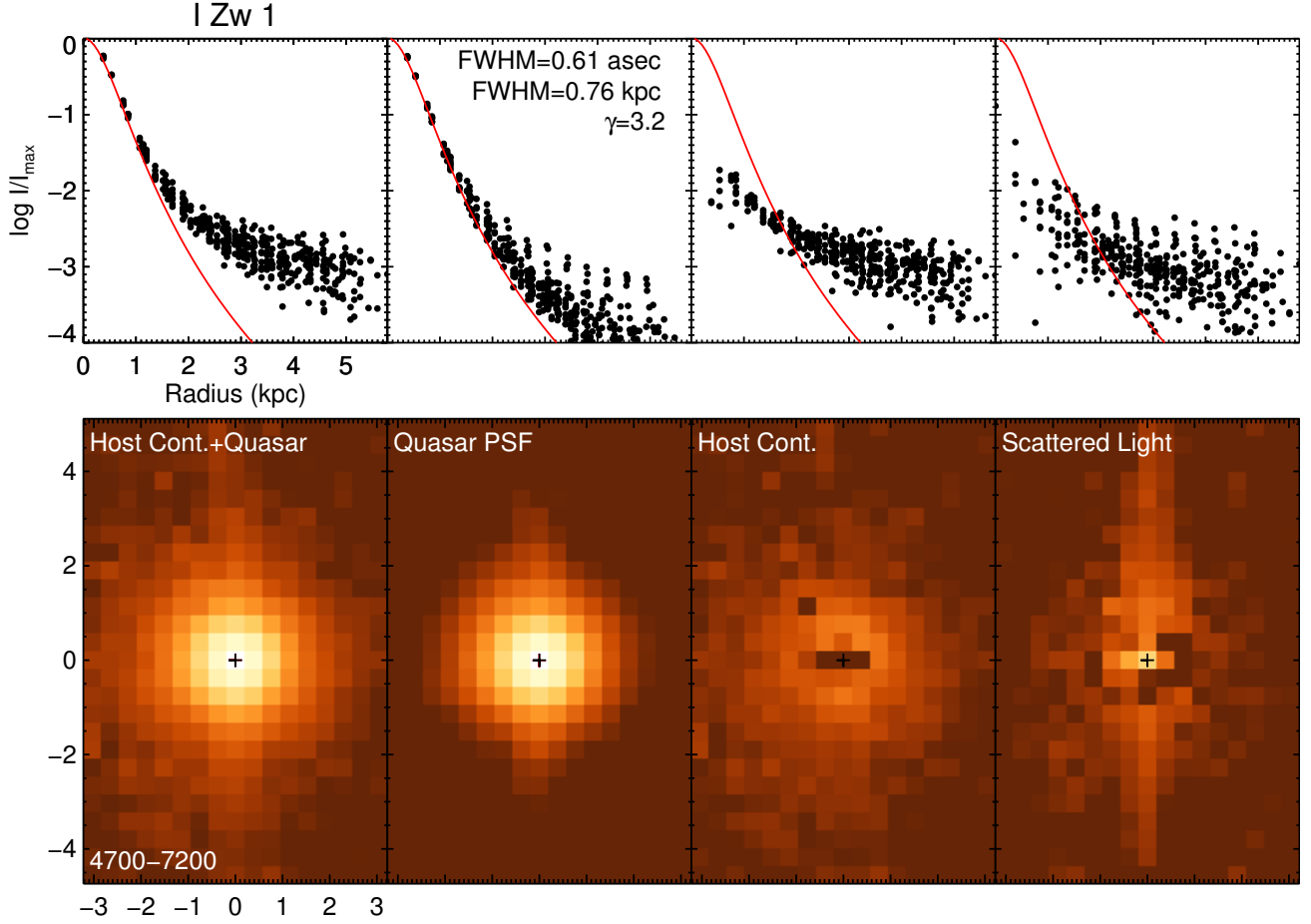


Figure 5. Radial intensity profiles and corresponding images of the galaxy continuum and the continuum components extracted from the fit (§ 2.3.1). In each column, the top panel shows \log of normalized intensity vs. radius. The bottom panel shows the corresponding image on a log intensity scale. The left (or only) column shows host galaxy continuum plus quasar PSF, summed over the fitted wavelength range (listed in the corner of the image). For data where an unresolved quasar spectrum is fit, the middle column shows the summed quasar-only data. The right column then shows the host continuum. A circular 2-D Moffat fit to the quasar PSF is in red on the top row, and the best-fit FWHM and Moffat index are printed in the upper right corner of the top middle panel. In one case, I Zw 1, a fourth column also shows the polynomial component separated from the stellar component and easily identifiable as strong scattered light by the central vertical stripes. In the bottom panels, the black cross locates the quasar center, based either on unsaturated *HST* images (F05189–2524, F13218+0552, and F13342+3932; Figure 1) or fitting of the quasar PSF image (other cases). The red cross is the fitted center of each image. The black and red crosses differ in the total image (left column) in the three cases where the host contributes to the ground-based PSF (Figure 1 and § 2.3.1). The fitted and assumed QSO centers (middle column) are typically identical but differ by $0''.04$ in F05189–2524, reflecting the imperfect PSF template due to host galaxy contamination. (The complete figure set (10 images) is available.)

fits. Reddening of the stellar population, which is almost certainly present, was not included in the fits because of the additional degrees of freedom this requires. Inclusion of reddening would likely result in younger best-fit ages. The luminosity-weighted age mixtures from these fits vary from a combination of ages $\lesssim 10$ Myr with ages $\gtrsim 100$ Myr to populations dominated by ages $\gtrsim 1$ Gyr. The precision of these ages is likely coarse, given the single metallicity, unreddened populations and the lack of ages 10–100 Myr in the best-fit populations. However, the important outcome of these fits is not an accurate set of ages but rather an accurate fit to the underlying stellar continuum, particularly in the Balmer lines and Na I D, at modest spectral resolution, which can be produced by more than one combination of stellar populations.

For the two sources where unsubtracted scattered light was most problematic (§ 2.2; I Zw 1 and PG1411+442), the starlight fits also included a separate very broad component in H α and H β which was limited in wavelength but allowed to vary in flux and width. The scattered light under-subtraction was pronounced in these two broad emission line features because of their intrinsic strength in the quasar spectrum and the particular way in which light is scattered across the 2-D GMOS raw data. Including these free components, which were discarded after fitting, significantly improved the fits.

The wavelength-integrated results of the quasar/galaxy decomposition with IFSFIT are shown in Figure 5. Moffat fits to the quasar PSF are also shown in this figure, which illustrate the effectiveness of the spectral method in recovering a smooth PSF. The exponential model that multiplies the quasar spectrum in each spaxel is shaped primarily by the I_1 term, likely due to its similarity to the theoretical dependence of the seeing-only PSF on wavelength. In every case, the host galaxy (starlight plus emission lines) is visible as an excess over the PSF in the radial profile. In most cases specific features in the host galaxy image are easily recognizable in *HST* images (Figure 1).

The Legendre polynomial components of the fits represent featureless continuum contaminants due to incomplete scattered light removal, imperfect PSF removal, or unfit stellar continuum components. The percent contributions to the total fitted light are in the range 20–50%, with a median of 37%. For the purposes of this analysis, the polynomial component is assumed to be part of the host galaxy, an assumption which is borne out by the qualitative comparisons of the host galaxy reconstructions with *HST* images. However, in one system with strong residual scattered light, I Zw 1, the polynomial component is identifiable as scattered light and is separated from the host emission (Figure 5).

The stellar velocity maps resulting from the starlight fits are shown in Figure 6.

The fidelity of the host galaxy reconstructions is at a minimum within 1–2 spaxels of the nucleus (i.e., within 0.5–1 spatial resolution elements). However, even within this radius, some stellar and line properties can still be extracted accurately (see Figure 6 and the emission- and absorption-line maps presented below), with this accuracy depending on the relative strength of the PSF, the details of scattered light contamination, and the strength of the relevant line features.

2.3.2. Emission Line Fitting

Resolved line emission was detected and fitted in each quasar, though in F21219–1757 the emission was too weak for the line properties to be robustly determined. Every data cube also included unresolved line emission from the NLR; this unresolved emission was present in the point source spectrum. The NLR emission was not removed from the point source spectrum prior to using it as a continuum template, because at the physical resolutions of the target and instrument combinations, the NLR emission is dominated by unresolved components. Tests showed that removing NLR emission from the point source spectrum before fitting yielded very different fits. This was due to the emission line fit in many spaxels being dominated by the unresolved point source component.

Lines were modeled with 1–2 Gaussian velocity components in each spaxel. All strong emission lines were fit with the same velocity components. Only one component was fit in PG1411+442 and F21219–1757, and up to two components were fit in the rest of the sample. The initial guesses for the number of components per spaxel in a given data cube or region of a cube were set by hand beforehand, and were tailored for each cube or region to produce better by-eye fits. Model line profiles were convolved with the spectral resolution before fitting. Each component was automatically checked for significance after the fit and kept only if it exceeded a 3σ flux threshold in at least one strong line. After fitting, each emission line in a velocity component was checked and set to zero flux if the significance of that line was below 2σ .

If two components were fit, the components were sorted into two maps by wavelength or velocity dispersion. For a given galaxy, the first component (c1) has either a longer wavelength or a smaller velocity dispersion than component 2 (c2). The choice of sorting by wavelength or velocity dispersion was applied to the entire cube. The choice depended on which method by eye produced the smoothest rotation signal in c1. If an outflow was present, it was assumed to arise in c2. However, c2 was not assumed to be an outflow in every case. In I Zw 1, c2 has very low velocities and does not show velocity gradients consistent with a coherent outflow. This component is assumed to arise from other effects (e.g., tidal motions).

This method does not assign c1 or c2 to the galaxy-rotation model or “other” model a priori. Rather, c1 and c2 are assigned to galaxy-rotation and other based on what makes the best galaxy-rotation model. This predisposes the analysis to a good disk model rather than having it predisposed toward the other model. When an outflow component is present in c2, there is thus higher confidence that such a feature exists.

Ionized outflow is represented by blueshifted emission lines in c2. It is possible that redshifted emission may in some cases represent the back side of the outflow; however, in most cases c2 is dominated by high-velocity blueshifted motions. The only clear-cut cases of redshifted outflowing emission are PG1613+658 and PG1700+518; in these cases the outflow is taken as the entirety of c2.

Maps of strong emission lines for each galaxy in

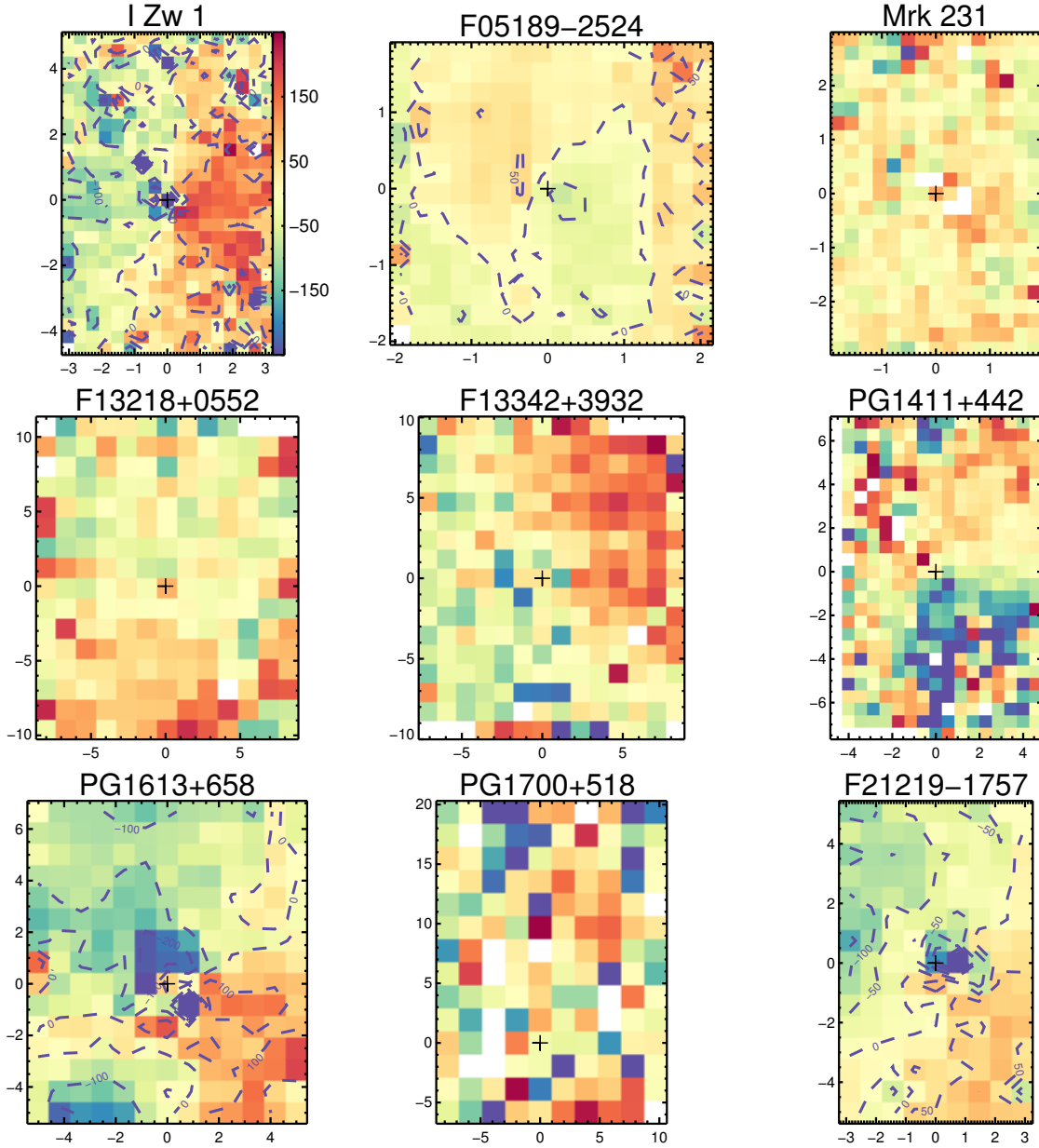


Figure 6. Stellar velocities in each quasar host except F07599+6508, for which the stellar component could not be fit. Axes are in kpc. Contours are shown in cases where the S/N is high enough; contour labels are in km s^{-1} relative to systemic. Rotation is evident except in Mrk 231 and PG1700+518; the former may be near face-on, while the latter data is shallow. There is remarkable spatial coherence within individual maps, despite the quasar PSF dominating the light in most data cubes.

which these lines are detected are shown in Figure 7. [N II] 6583 Å (or [O III] 5007 Å in the cases in which [N II] 6583 Å is not present in the wavelength range) was chosen as a strong representative line. Each figure displays maps of the total line flux; the flux in each component; the velocity dispersion of each component, σ^{c1} and σ^{c2} ; and the central velocity of each component, $v_{50\%}^{c1}$ and $v_{50\%}^{c2}$.

For galaxies in which more than one emission line component was fitted, two other panels appear: a map of the flux density at a representative blueshifted velocity, and a map of the velocity that encompasses 98% of the cumulative velocity distribution in each spaxel, $v_{98\%}^{c2}$. This convention matches that used in some previous IFS studies (Rupke & Veilleux 2011, 2013a,b). The cumulative

percentages are derived in blueshifted spaxels by integrating from the red side of the velocity distribution, such that $v_{98\%}^{c2}$ is representative of a “maximum” blueshifted velocity. In redshifted spaxels, $v_{98\%}^{c2}$ is correspondingly calculated by integrating from the blue side of the line.

Because they are forbidden lines, [N II] and [O III] may reflect outflow or AGN-related physics more than the recombination line maps. The Balmer lines are also more susceptible to errors in stellar or quasar subtraction, since Balmer lines feature strongly in these templates. Nonetheless, maps of the other lines are consistent with the maps shown.

Besides the fluxes and kinematics, other quantities calculated from the emission lines on a spaxel-by-spaxel basis are reddening $E(B - V)$ (Fig. 8), electron density n_e

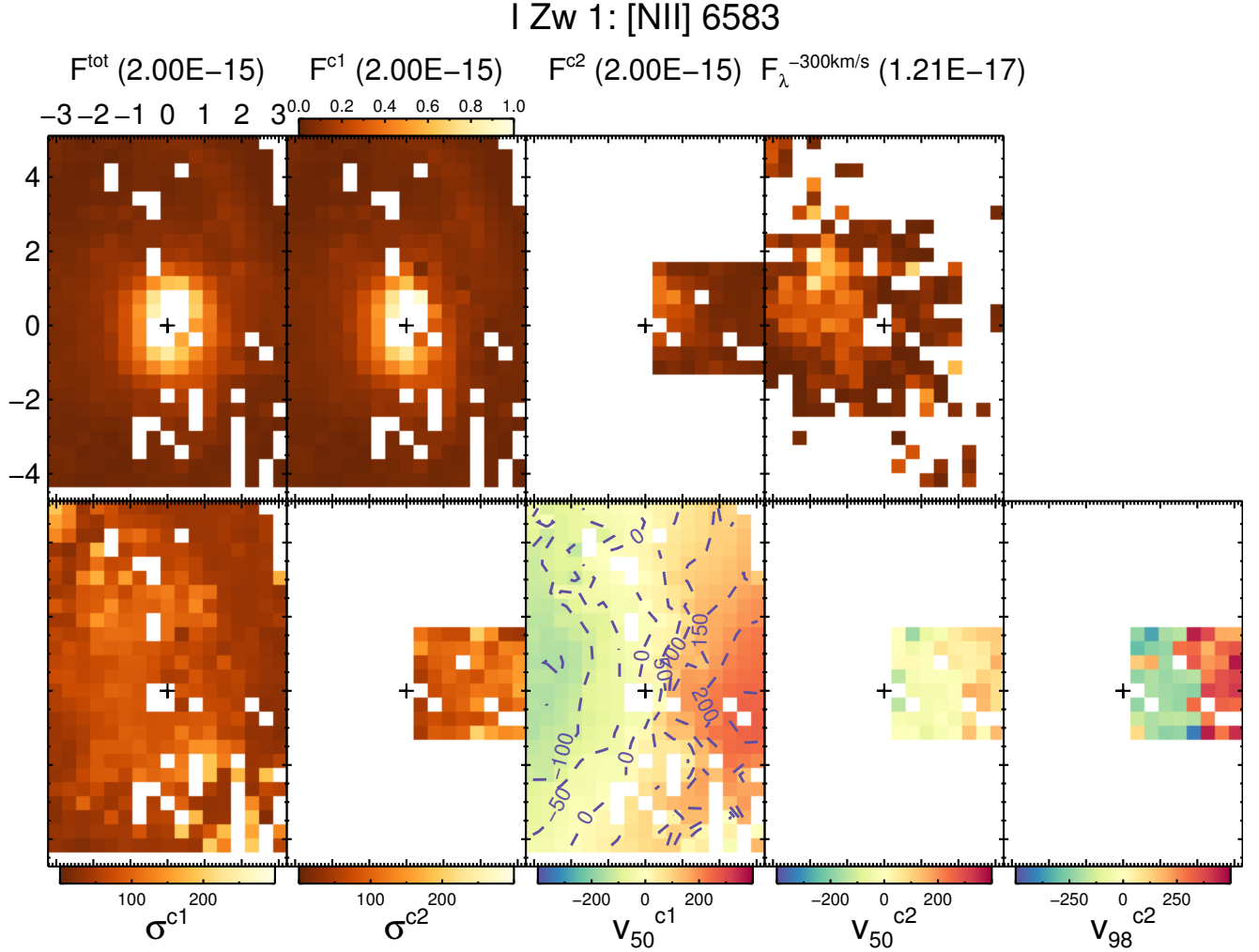


Figure 7. Properties of the [N II] 6583 Å or [O III] 5007 Å emission lines in each quasar. Top panels show total flux and flux per component in units of $\text{erg s}^{-1} \text{cm}^{-2} \text{arcsec}^{-2}$, and flux density at a representative blueshifted velocity (if more than one component is fit) in units of $\text{erg s}^{-1} \text{cm}^{-2} \text{Å}^{-1} \text{arcsec}^{-2}$. The flux scale is from 0 (dark orange) to 1 (white), and the peak flux is listed in each panel title. Bottom panels show velocities: the velocity dispersion σ of each component, the central velocity ($v_{50\%}$) of each component, and $v_{98\%}^{c2}$ if a second component is fit. Color bars show the velocity scales in km s^{-1} . The spatial image scale in kpc is shown on the axes of the upper left panel. Velocity contours are plotted atop $v_{50\%}^{c1}$ in all cases but Mrk 231, for which the contours are too noisy. (The complete figure set (9 images) is available.)

(Fig. 9), and line ratios (Fig. 10). These three quantities are calculated after fluxes have been summed over both components (c1+c2). The measurements for individual components are noisier than for the flux or velocity measurements, and summing over both components produces more spatially-coherent maps. However, the maps of $E(B - V)$, n_e , and line ratios for individual components (c1 or c2) are generally consistent with the c1+c2 maps.

$E(B - V)$ is calculated from the Balmer decrement of the c1+c2 line flux (Fig. 8). Case B at 10^4 K and the Cardelli et al. (1989) extinction curve are assumed. These reddening maps are not used to correct the line maps in Figures 7 and 10 because in many spaxels the reddening is too noisy to be useful (these spaxels are not shown in Figure 8). This is largely due to limited sensitivity to H β in some data cubes.

Electron densities are calculated from the c1+c2 fluxes

and the [S II] 6717 Å/[S II] 6731 Å ratio (Fig. 9). The fit of [S II] 6717 Å/[S II] 6731 Å vs. n_e from Sanders et al. (2016) is used, but it is assumed that the ratio is not sensitive to n_e below 10 cm^{-2} and above $10,000 \text{ cm}^{-2}$ as it asymptotes, and calculated densities outside of this range are set to the lower or upper limit. Spatially-averaged values of n_e in each quasar range from 50 to 410 cm^{-2} , with a median of 150 cm^{-2} .

Flux differences among lines are displayed in standard line ratio plots in Figure 10. Resolved line ratio maps are typically used to distinguish the dominant excitation mechanism (stellar photoionization, shock ionization, or AGN photoionization; Veilleux & Osterbrock 1987; Kewley et al. 2006), to determine the fraction of each mechanism that is ionizing the gas in each spaxel (Rich et al. 2011; Davies et al. 2016a, e.g.), and to measure physical parameters of the ISM and radiation field by comparison to theoretical models (Dopita & Sutherland 1995; Groves

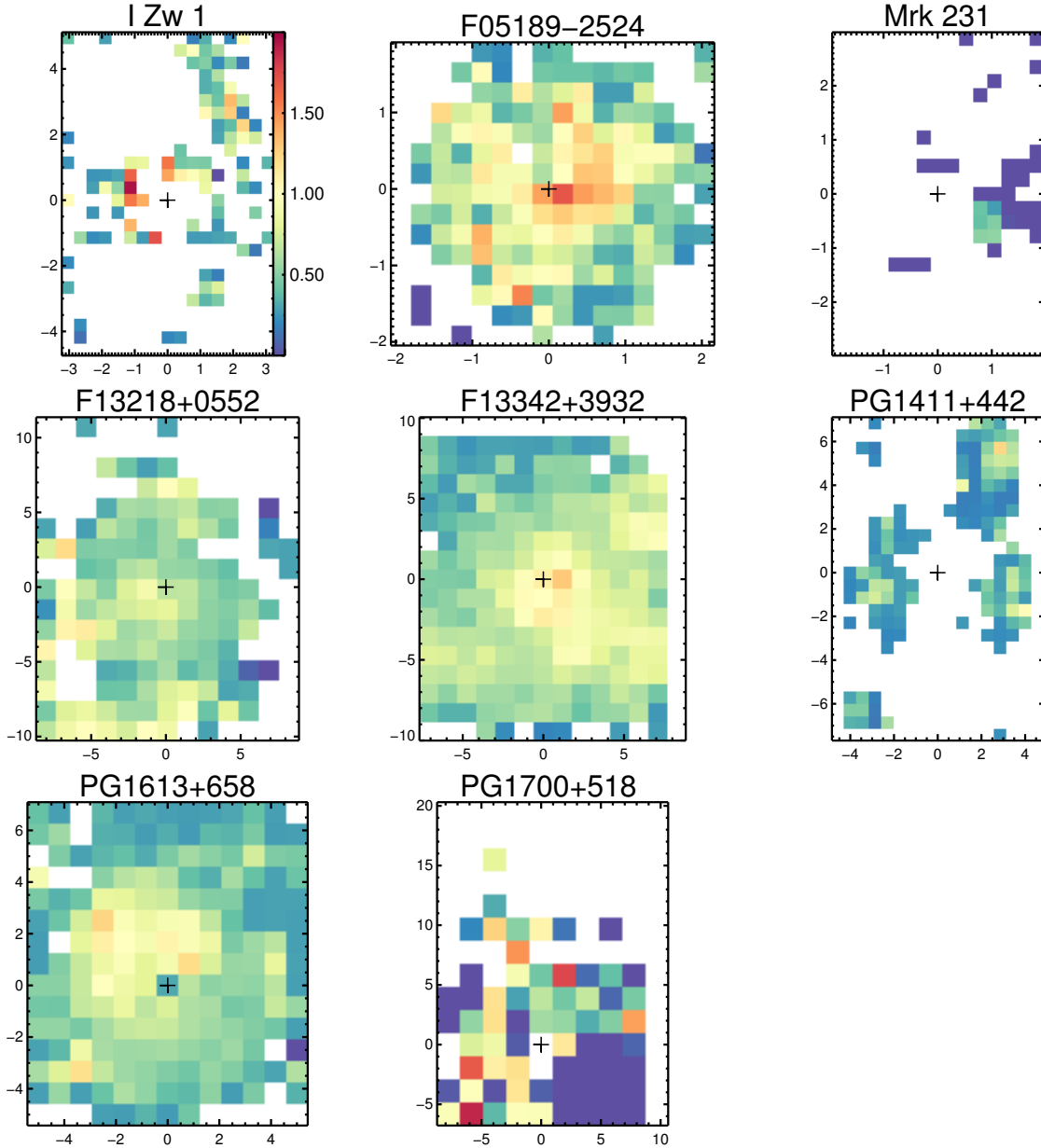


Figure 8. Reddening $E(B - V)$ in quasar hosts with more than one Balmer emission line detection, as measured from the Balmer decrement. Fluxes are summed over components before $E(B - V)$ is calculated. The Cardelli et al. (1989) extinction curve and case B at 10^4 K are assumed. The $H\alpha/h\beta$ flux ratio is used in all cases but Mrk 231 and PG1700+518, in which the $H\beta/H\gamma$ ratio is used. No Balmer lines are detected in F21219-1757. $E(B - V)$ is calculated only in spaxels where two Balmer lines have 2σ detections.

et al. 2004; Dopita et al. 2006). These plots are discussed further in § 3.1.

2.3.3. Absorption Line Fitting

Half of the quasars in this sample show blueshifted resonant absorption from the Na I D doublet in the PSF template spectra (Figure 2). F07599+6508 and Mrk 231 show broad absorption (Boroson & Meyers 1992; Veilleux et al. 2013b, 2016). F05189-2524 (Rupke & Veilleux 2015), F13342+3932, and PG1411+442 (Hamann et al. 2017, in prep.) show narrow absorption. Many also show possible resonant broad emission, which requires high column densities, though it is difficult to distinguish it from nearby He I 5876 Å emission without careful fitting (Thompson 1991).

In this work, the unresolved absorption is fit out as part of the PSF removal and discarded. The goal is instead to measure the resolved, extended absorption and emission that appears as part of the host galaxy spectrum.

The Na I D doublet and He I emission line were fit using the methods of Rupke et al. (2005b, for Na I D absorption) and Rupke & Veilleux (2015, if Na I D emission is present). These techniques robustly separate optical depth and covering factor in absorption, even for a blended doublet and multiple velocity components, by assuming a Gaussian in optical depth. They also handle cases of combined resonant absorption and emission. In all cases but one, the Na I D and He I lines were fit simultaneously, but the He I was constrained where needed by fits to other emission lines. In one case with

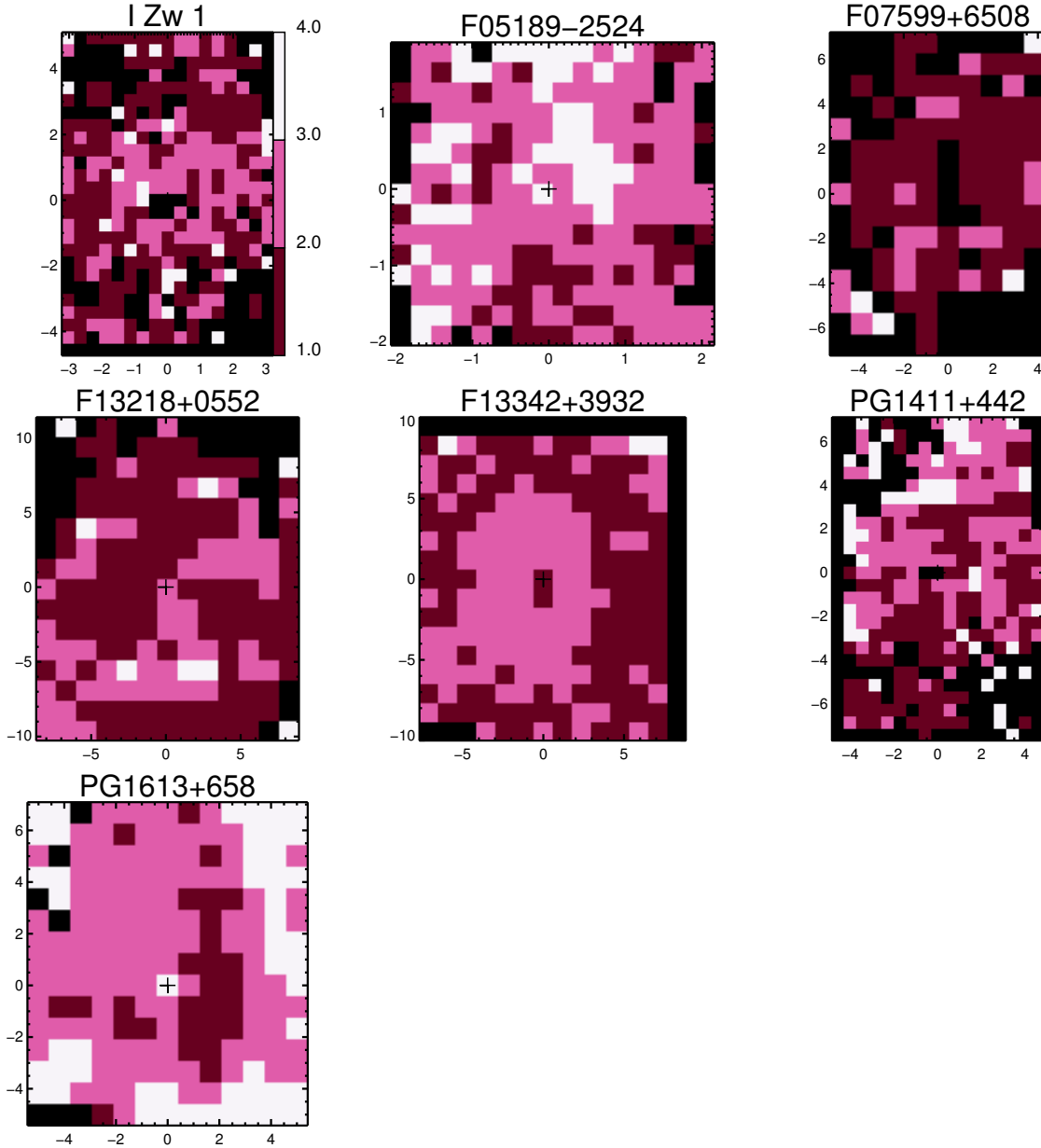


Figure 9. Electron density n_e in quasar hosts with [S II] 6717, 6731 Å measurements. Fluxes are summed over components before n_e is calculated. Density is calculated from the [S II] 6717 Å/[S II] 6731 Å ratio using the parameterization of Sanders et al. (2016). Upper and lower sensitivity limits of 10^1 cm^{-2} and 10^4 cm^{-2} are imposed. n_e is calculated only in spaxels where the two lines have 2σ detections. The colorbar displays ranges of $\log(n_e/\text{cm}^{-2})$.

very high S/N, F05189–2524, the He I line was fit with other emission lines rather than as part of the Na I D fitting.

In both the integrated and the spaxel-by-spaxel fits, one Na I D component was fit in all cases but PG1411+442 (see below), Mrk 231, and F05189–2524. The latter two are the nearest galaxies in this sample and have deep, high-S/N integrations. The F05189–2524 fits are similar to those previously published (Rupke et al. 2005a; Rupke & Veilleux 2015), though here the binning is coarser and the spatially unresolved continuum has been removed to match the treatment of the rest of the sample. The integrated spectrum requires 3 components in absorption, while the spaxel-by-spaxel fit uses 2 com-

ponents. The Mrk 231 fits use deeper data than previously published (Rupke & Veilleux 2011), which enables 2-component fitting.

Two cases of the strongest and highest-S/N absorption (F05189–2524 and Mrk 231) also show redshifted Na I D emission. The F05189–2524 emission is analyzed in Rupke & Veilleux (2015); the deep Mrk 231 data reveals the new Na I D emission, but it is not discussed further here.

For all quasar hosts but one, the host continuum for these fits is assumed to be a combination of the stellar and polynomial components. In one case with strong scattered light, I Zw 1, the polynomial component was successfully identified as scattered light and the contin-

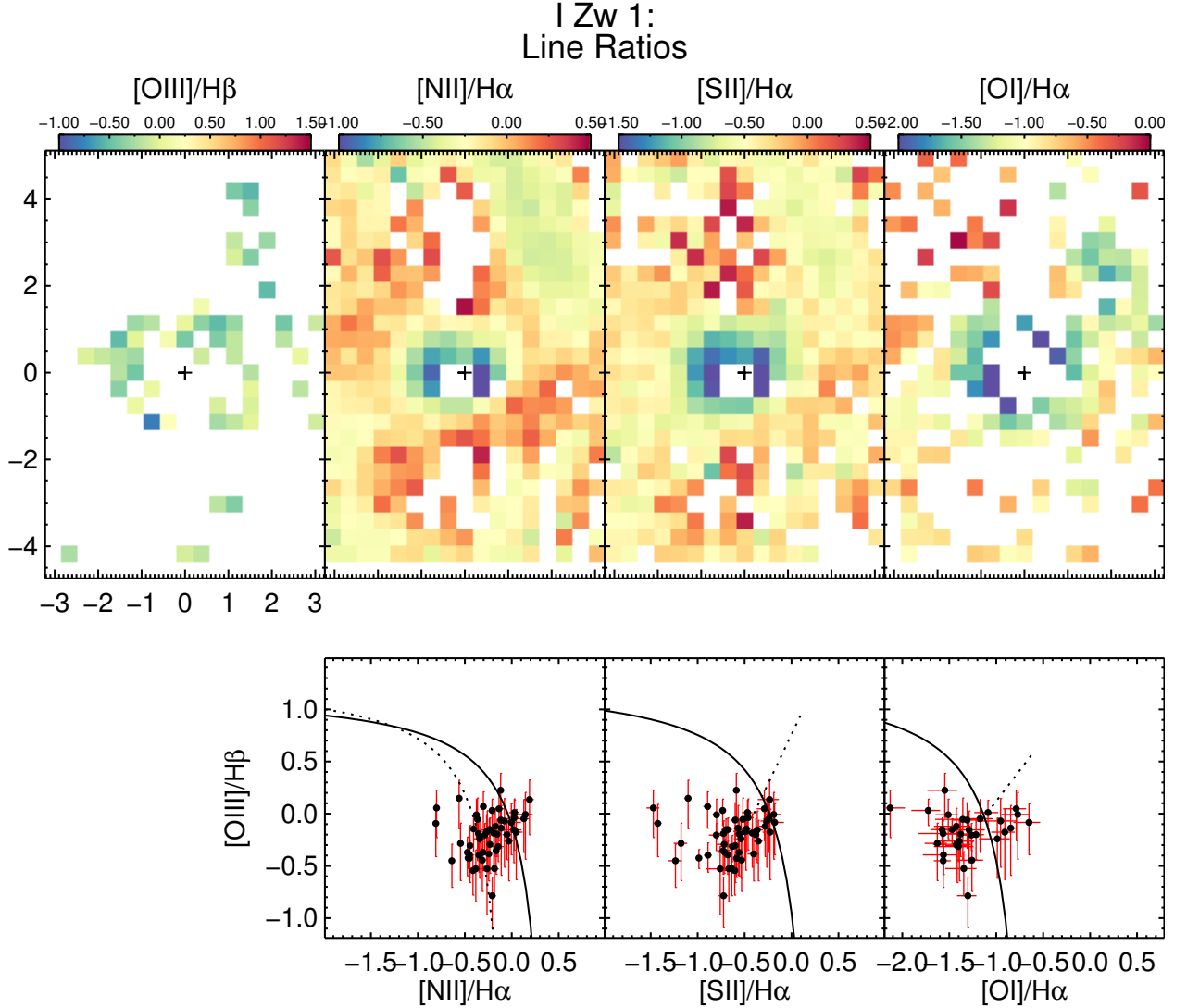


Figure 10. Strong emission line ratios and line ratio diagrams for each quasar. Fluxes are summed over components before the ratios are calculated. The line ratio scales are logarithmic. In the bottom panels, theoretical maximum starburst lines (solid lines; Kewley et al. 2001, 2006), an empirical star forming galaxy locus (curved dashed line; Kauffmann et al. 2003); and a line separating nuclear line ratios from Seyferts and LINERs (straight dashed lines; Kewley et al. 2006) are shown. The line ratios typically reflect a mixing sequence between stellar and AGN ionization, with shocks important in some cases (§ 3.1). (The complete figure set (9 images) is available.)

uum is assumed to be the purely stellar component. (The effect of removing the polynomial component is to increase the resulting values of the covering factor C_f , and consequently to increase the global flow rates; § 3.2.)

Fits to Na I D in the integrated quasar host spectra (Figure 11) reveal extended interstellar absorption in every case except PG1700+518 (for which the Na I D feature is not in the observed wavelength range).

In the spaxel-by-spaxel fits, spaxels with fitted equivalent width $S/N > 5$ were considered significant detections. Of the nine quasar hosts with extended interstellar absorption, eight show this absorption on a spaxel-by-spaxel basis (Figure 12). The maximum extent of this absorption ranges from 1–10 kpc, and the structure of the absorption is varied. Wind structure is discussed further in the next section. Most equivalent widths are in the range 1–10 Å.

Figure 12 also shows the velocity maps of the neutral outflows. In cases where two outflowing absorption line

components are fit, the lines in each spaxel are first combined into a cumulative velocity distribution weighted by optical depth; $v_{50\%}$ and $v_{98\%}$ are calculated with respect to this total distribution. The maps also show the velocity of the peak optical depth, which differs from $v_{50\%}$ for two or more components. Finally, Figure 12 compares the fitted equivalent width with an empirical estimate from simple integration (Rupke & Veilleux 2015); this is a sanity check on the quality of the fits. Generally, the fits tend to recover more signal and are a better estimate of the line properties (Rupke & Veilleux 2015).

PG1411+442 shows a weak but significant high-velocity extended component (-1300 km s^{-1}). Tests of integrated spectra of varying apertures show that this absorption has a maximum extent of 1–2 kpc from the quasar (in projection). The low-velocity absorption extends to larger radii. Thus, two components are fit within five spaxels of the nucleus, and one component outside of this.

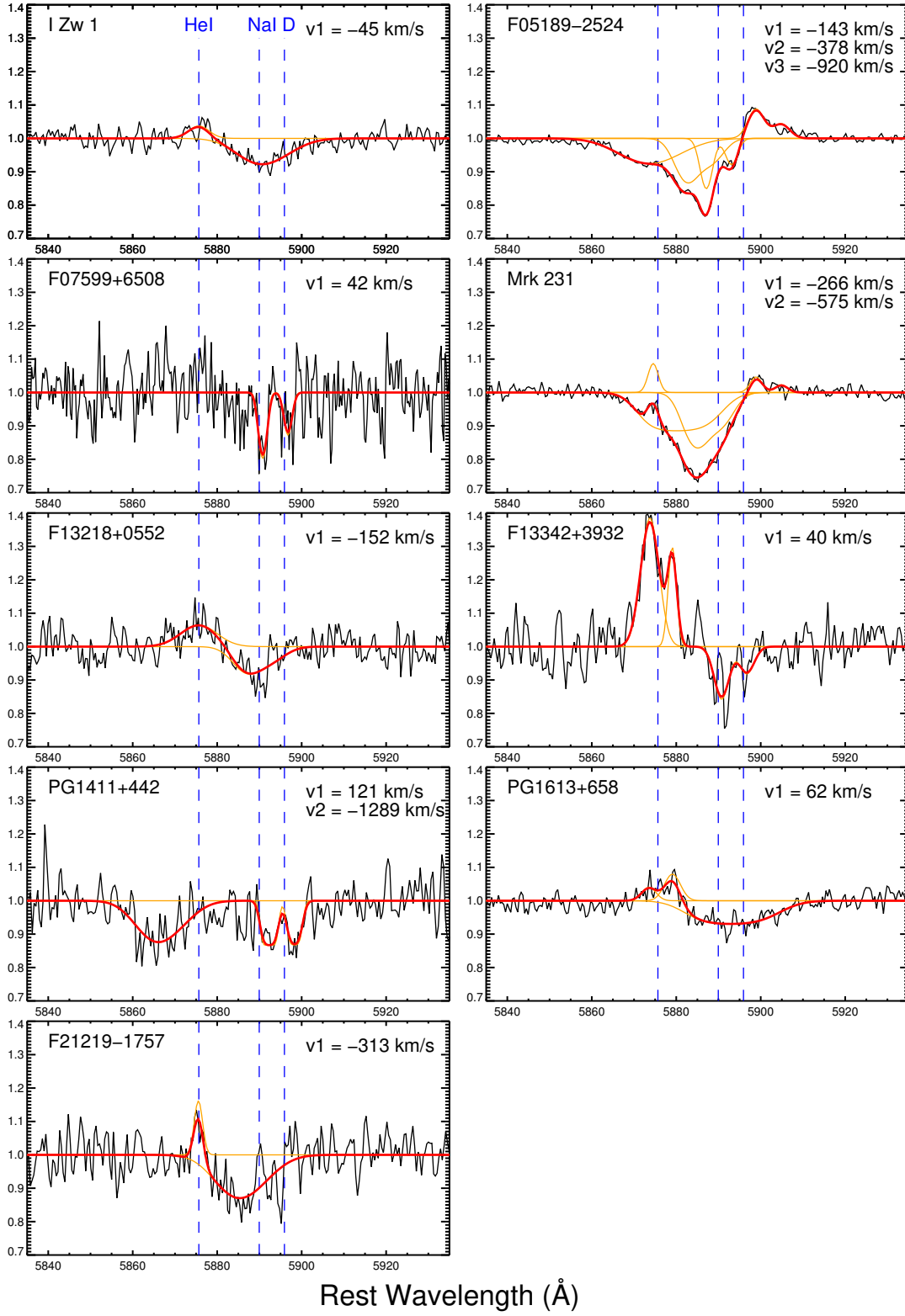


Figure 11. Fits to Na I D absorption and emission and He I 5876 Å emission in starlight spectra integrated over the IFS FOV. The quasar light has been removed from each spectrum (§ 2.3.1). Velocities ($v_{50\%}$) of the absorption components are listed in each panel. Vertical dashed lines are line locations based on the galaxy’s systemic velocity.

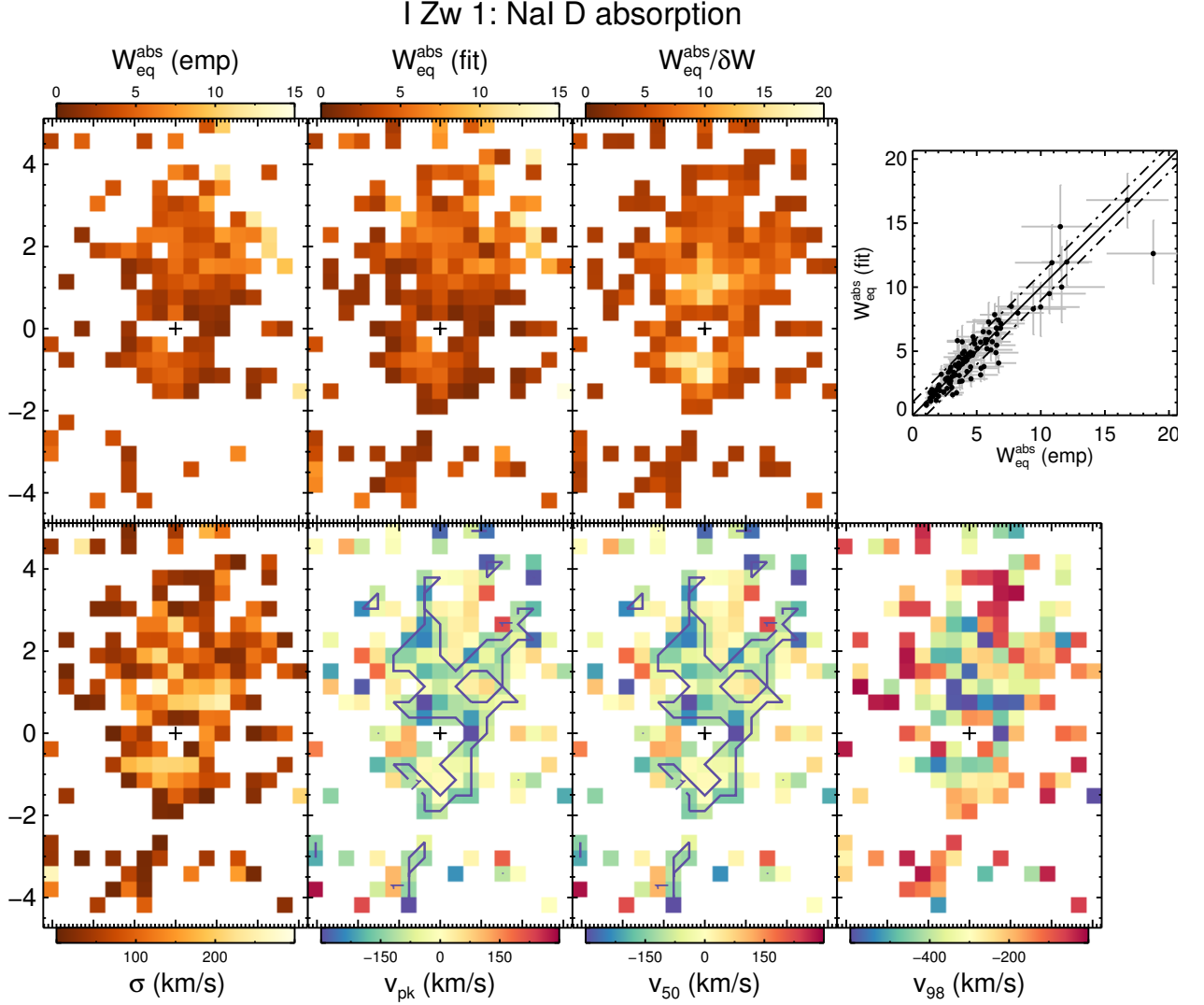


Figure 12. Na I D absorption-line properties in each quasar host in which resolved absorption is observed. Top panels show empirical and fitted observed-frame equivalent widths W_{eq} (in units of Å), fitted W_{eq} signal-to-noise, and the correlation between empirical and fitted measurements. Empirical equivalent widths are calculated from simple integration, while fitted equivalent widths are calculated from line fits. The empirical estimates are a sanity check on the fitted equivalent widths. Bottom panels show velocity maps: velocity dispersion σ , peak velocity (in optical depth space) v_{pk} , $v_{50\%}$, and $v_{98\%}$. In the cases where only one component is fit, $v_{\text{pk}} = v_{50\%}$. In the three cases where two components are fit (F05189–2524, Mrk 231, and PG1411+442), the components are combined in a cumulative distribution based on optical depth and the velocity maps reflect this (§ 2.3.3). Zero-velocity contours divide blueshifted and redshifted spaxels. (The complete figure set (9 images) is available.)

For PG1613+658, the spaxel-by-spaxel accounting for the line does not reveal that it extends in every direction around the nucleus. The extended absorption that is detected on a spaxel-by-spaxel basis is a strong velocity component that arises in front of a small satellite galaxy that is ~ 5 kpc from the quasar in projection (Figure 1), and is redshifted at a velocity similar to the ionized gas disk of the quasar host at that location.

The detected absorption is generally blueshifted; spaxels with $v_{50\%} < 0$ km s $^{-1}$ are assumed to be outflowing. There is some absorption near systemic or slightly redshifted (up to ~ 200 km s $^{-1}$). In three systems (F07599+6508, PG1411+442, and PG1613+658) these make up a substantial fraction of the spaxels with detected absorption. In PG1613+658, this is due to the nearby companion. The same may be true in PG1411+442. In F07599+6508, the origin of the redshifted absorption is unclear.

3. RESULTS

A key result from this study is the set of maps of the properties of emission and absorption lines, as well as the continuum maps, for each galaxy. These maps can be used to constrain properties of the AGN and its host galaxy. However, the scientific focus of this paper is the large-scale outflows in these systems. This section outlines how these maps constrain the properties of ionized and neutral outflows. In it, the outflow properties in the current sample are also compared to host galaxy properties, black hole properties, and to the outflows in other galaxies.

Though a detailed physical interpretation of the disk kinematics of these quasars is not essential to constraining the outflow properties of these data, it is important to assess the presence of disks because of their dominant imprint on the spectra and because their geometry can relate to the outflow orientation. Every quasar in this sample does show evidence for a rotating ionized gas or stellar disk. 9/10 quasars show an ionized gas disk, and in the 10th system (F21219–1757) the surface brightness of the ionized gas is too low (and the S/N too low) to determine its properties. 7/10 quasars show a stellar disk (Figure 6); in two of the other cases (F07599+6508 and PG1700+518) the S/N is again too low to robustly constrain the stellar velocities, while in the 10th case (Mrk 231) the stellar disk is either slowly rotating or nearly face-on, similar to the gas disk. In each case these disks extend to the edges of the FOV. Finally, 3/10 quasars have low-luminosity companions within or at the edge of the FOV (PG1411+442, PG1613+658, and PG1700+518). In at least one case, PG1700+518, this companion may have a significant effect on emission line component c1.

3.1. The Presence, Orientation, and Ionization of Large-Scale Outflows

Of the radio-quiet Type 1 quasars in this sample, all contain large-scale (maximum sizes 3–12 kpc) outflows of ionized and/or neutral gas, as revealed by the presence of broad, blueshifted absorption lines and broad, blueshifted emission lines. If we break the detections down by phase, 70% have ionized outflows, 80% have neutral outflows, and 50% have both. This detection rate

contrasts with the $\sim 10\%$ detection rate of ionized outflows in a previous IFS study of Type 1 quasars (Husemann et al. 2013, hereafter H13), but is consistent with the very high detection rate in nearby Type 2s (Harrison et al. 2014; McElroy et al. 2015; Bae et al. 2017).

For the two objects in common between H13 and this work (I Zw 1 and PG1700+518), there is agreement on the ionized outflow properties. The significant disagreement on the detection rate could thus result from differences in sample selection, as H13 select lower-luminosity AGN. Part, though not all, of the discrepancy could also result from our choice to probe both neutral and ionized gas outflows, rather than just ionized outflows, which could increase the detection rate.

A third possibility is that the different detection rate between our study and H13 results from data quality differences. The data in H13 were taken with the Potsdam Multi-Aperture Spectrophotometer (PMAS) on the 3.5m Calar Alto telescope. The quoted emission-line surface brightness limit of H13 (at lower spatial and spectral resolution) is a factor of 3–4 worse than the best values achieved in the current study ($\sim 5 \times 10^{-17}$ erg s $^{-1}$ cm $^{-2}$ arcsec $^{-2}$; Figure 7). The 0''.5 sampling of PMAS is larger than the 0''.2 GMOS hexagonal spaxels, and the typical seeing of H13 was about twice the current study. The spectral resolution in H13 varied from 2 to 4 \times coarser than the current study. These factors make separating a second (typically broad, faint) outflowing emission line component from a disk component more challenging. The exception is when the outflow dominates the line emission. In PG1700+518, the outflow completely dominates the line emission in [O III], and both studies classify it as a large-scale outflow.

The approximate projected outflow boundaries and orientations are shown in Figure 13. The average outflow position in each phase is calculated in projected Cartesian coordinates; the position weighted by $v_{50\%}^2$, $v_{98\%}^2$, and W_{eq} or flux is also calculated. These different weightings give a sense of the uncertainty in computing the true orientation of the outflow.

Loosely-collimated outflows along their host galaxy's minor axes are common on kpc scales in many starburst and active galaxies observed with IFS (e.g., Rupke & Veilleux 2013b). The observed outflows in these quasars are also typically oriented near their hosts' minor axes. Clear exceptions to this are the outflows in F13218+0552, the neutral outflow in F07599+6508, and the ionized outflows in PG1613+658 and PG1700+518. One expects some exceptions due to projection effects, which will enhance misalignments for systems that are nearly face-on. PG1613+658 and PG1700+518 have outflows misaligned with the minor axis for reasons described below. The outflows in F13342+3932 would at first glance appear to be exceptions as well. However, the highest velocity neutral gas lies right along the minor axis at 1–2 kpc scales, and the largest ionized fluxes are found along the minor axis on the same scales in the opposite direction. This behavior is not captured in the outflow positional averages, as the outflow is spatially dominated by an apparently less collimated flow at larger scales.

The opening angle of an outflow (between 0° and 180°) quantifies its collimation; loosely-collimated outflows have large opening angles. In the bipolar cone

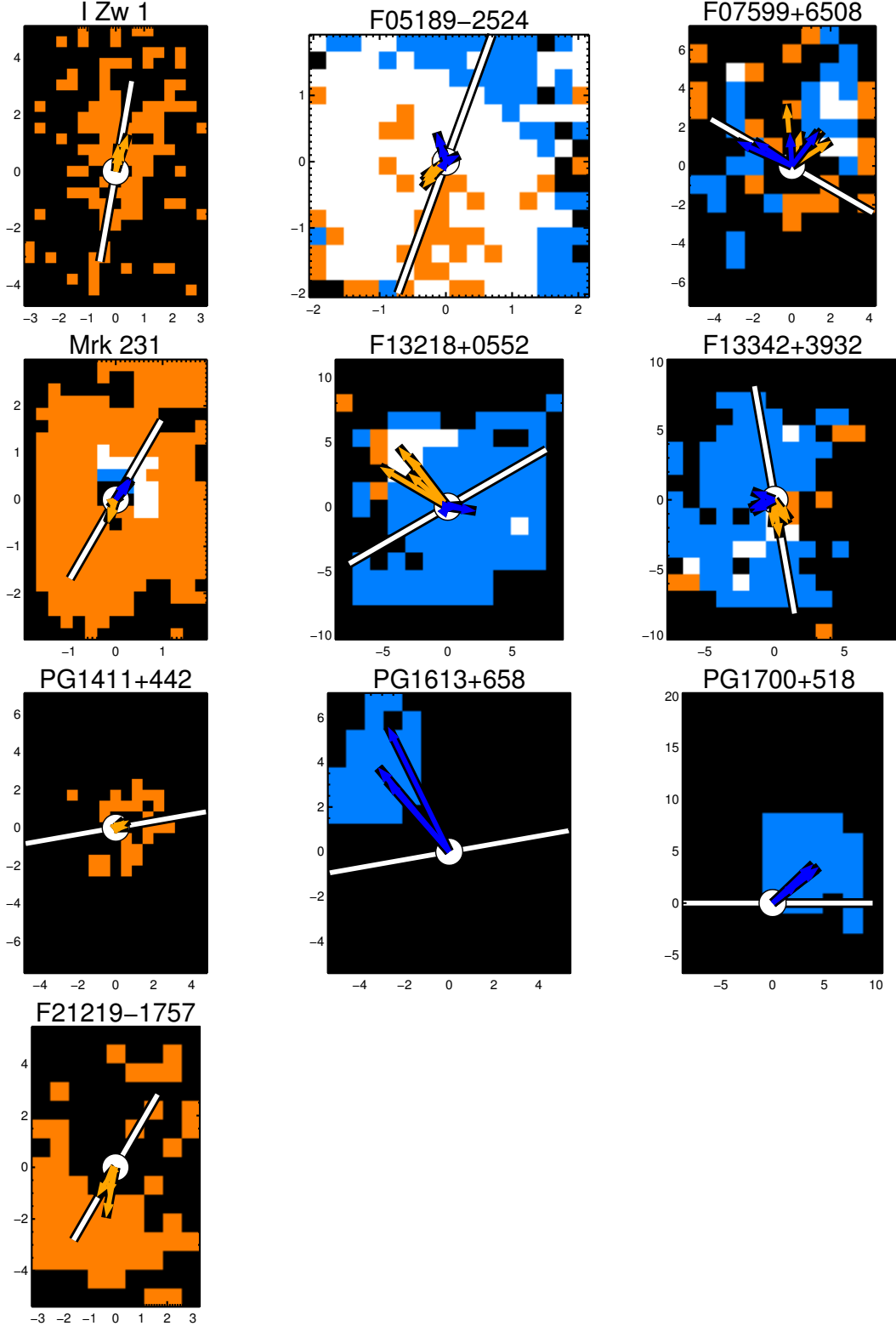


Figure 13. The outflow geometry of each detected outflow (§ 3.1). The neutral outflow is shown in orange, the blueshifted part of the ionized outflow in blue, and the overlap in white. The galaxy nucleus and minor axis are shown as a black-outlined white circle and line, respectively. The average outflow positions are means over all outflow spaxels. Arrows are drawn from the nucleus to this average position. Four averages, each with a different positional weight, are calculated and plotted for each gas phase to illustrate the uncertainty in the outflow position: unweighted, weighted by $v_{50\%}^2$, weighted by $v_{98\%}^2$, and weighted by W_{eq} or flux. Orange (blue) arrows denote the mean neutral (ionized) outflow position. Most outflows are oriented along or near the minor axis in projection, with some exceptions (the neutral outflow in F07599+6508, the outflows in F13218+0552, the ionization cone in PG1613+658, and the jet-driven outflow in PG1700+518 are not along the projected minor axis). It is possible that the outflows in F07599+6508 and F13218+0552 are along the actual minor axis if the minor axis is near the line of sight; some cases like this are expected. The outflows in F13342+3932 might appear to be exceptions to the minor-axis orientation, but are not (see § 3.1).

model, the opening angle is simply the projected two-dimensional angle between the sides of each cone. The broad footprints of the outflows in this sample (Figure 13) suggest loosely-collimated flows with large opening angles (perhaps approaching 180°).

In PG1700+518, the outflow lies along a known radio jet. This quasar is the most distant and radio-luminous in the sample with $z = 0.2905$ and $\log(P_{1.4 \text{ GHz}}) = 24.8 \text{ W Hz}^{-1}$. This places it at the knee of the radio luminosity function of nearby AGN (Condon et al. 2002), but two orders of magnitude below the knee of the $z \sim 0.3$ quasar 1.4 GHz luminosity function (Condon et al. 2013). It is one of two quasars in the sample with a known jet (Kukula et al. 1998; Yang et al. 2012). (The other is Mrk 231; see Morganti et al. 2016 and references therein.)

In PG1613+658, there is an extended NLR or ionization cone, presumably aligned with and collimated by the AGN torus, that is roughly along the galaxy major axis and traced by velocity component 2. It has very high $[\text{O III}]/\text{H}\beta$ values (Figure 10), indicative of AGN photoionization. The flux and bulk velocity of c2 peak about 2 kpc from the nucleus. Though the projected bulk motions (as traced by $v_{50\%}^{c2}$) of this component are similar to the disk motions in component 1, the large values of σ^{c2} and $v_{98\%}^{c2}$ are indicative of an outflow, and it is classified as such. This outflow may arise from the torus being misaligned with the host minor axis. The bulk of the AGN radiation is pointed into the disk, accelerating disk material (as in nearby Seyferts; Fischer et al. 2013). The lack of high bulk motions could mean the outflow is in the plane of the sky, and the decrease in $v_{50\%}^{c2}$ at large radii may mimic NLR deceleration in lower-luminosity systems (Fischer et al. 2013).

There is also an increased velocity dispersion and shock-like line ratios (high $[\text{N II}]/\text{H}\alpha$, $[\text{S II}]/\text{H}\alpha$, and $[\text{O I}]/\text{H}\alpha$) along the galaxy minor axis in PG1613+658, as seen in component 1. These latter effects have been used as tracers of outflows in other resolved studies (Lehnert & Heckman 1996; Ho et al. 2016). However, the dense velocity contours along the minor axis of this system coupled with the >2 kpc PSF means that the disk needs to be carefully modeled to account for beam smearing (Davies et al. 2011). In the absence of this detailed modeling, we do not include these spaxels as part of the outflow.

Strikingly, in the five systems where both neutral and ionized outflows are present, the neutral and ionized outflows are often oriented opposite each other. This ionized/neutral asymmetry is not obvious in other Type 2 quasars (Rupke & Veilleux 2013b). Spatially resolved observations show that Na I D absorption correlates with optical dust obscuration (Rupke & Veilleux 2013b, 2015). An anti-correlation in the outflow between line-emitting gas and dusty gas could reflect asymmetric obscuration in the outflow. On one side, the obscuration along the line of sight is small and the ionized outflow is prominent. On the other, the obscuration is higher and the neutral outflow dominates. One possible cause is the underlying gas disk, though the obscuration correlated with the wind is thought to be in the outflow rather than the disk (Rupke & Veilleux 2015).

The line ratio maps in Fig. 10 (calculated on a spaxel-

by-spaxel basis using fluxes summed over velocity components) are not used to determine whether or not an outflow is present, and a quantitative comparison of how the outflows relate to line excitation is reserved for future work. However, a qualitative understanding of the excitation of the ionized gas provides an overview of possible radiation physics in these outflows. The maps in Figure 7 and in the top panels of Figure 10 often visually reveal correlations between outflows and higher line ratios in many systems. However, this correlation is not one-to-one; for instance, only the redshifted side of the outflow in PG1700+518 has high excitation. And in some cases there is no obvious correlation (Mrk 231).

Line ratio diagrams, seen in the bottom panels of Figure 10, typically show patterns suggestive of stellar and AGN photoionization in a sequence mixing pure stellar photoionization and pure AGN photoionization. This mixing sequence, which moves from the lower left to the upper middle of these diagrams, is due to the fractional contribution of stellar and AGN photoionization varying from one part of the galaxy to another (e.g., Davies et al. 2016a). Stellar photoionization dominates in the lower left, and AGN photoionization in the upper middle, of these diagrams. There is also evidence of a stellar photoionization sequence in metallicity in at least two hosts (I Zw 1 and PG1411+442); this sequence is visible as a curving locus of points from the middle left to the middle bottom (e.g., Kewley et al. 2001). Shock ionization, a common feature of galactic winds (Veilleux & Rupke 2002; Sharp & Bland-Hawthorn 2010; Rich et al. 2011), is intermixed with AGN and stellar ionization in other systems (F05189–2524, F07599+6508, F13218+0552, and PG1613+658), and is dominant in at least one system (F05189–2524). Shock ionization dominates the right-hand side of these diagnostics (Dopita & Sutherland 1995; Rich et al. 2011), and mixing with other ionization mechanisms is revealed as loci of points connecting regions of stellar, AGN, and shock ionization. Finally, evidence of AGN photoionization variations due to changing ionization parameter (Scharwächter et al. 2011; Davies et al. 2016b) are evident in at least one quasar (F13342+3932). These changes are visible as loci of points moving from the upper middle toward the lower right.

3.2. Global Outflow Properties

The key physical quantities that measure the potential impact of an outflow on its host are velocities, size (maximum projected radius R), mass (M), momentum (p), energy (E), and the outflow rates of M , p , and E in each gas phase. In Table 4 we list mean and maximum values of FWHM^{c2} , $v_{50\%}^{c2}$, and $v_{98\%}^{c2}$. The averages are taken over spaxels in the outflowing component(s). The other quantities are listed in Table 5.

Mass, momentum, and energy and their outflow rates are calculated using a time-averaged thin shell model (the single radius free wind, or SRFW, model of Rupke & Veilleux 2013b) in which these quantities depend inversely on the assumed shell radius (Rupke et al. 2005c; Shih & Rupke 2010; Rupke & Veilleux 2013b). The thin shell model is a fiducial model for measuring such quantities. For spatially-resolved data, it has the advantage of being able to associate each point in the plane of the sky with a unique three-dimensional radius, assuming that

Table 4
Outflow Velocity Statistics

Galaxy (1)	Phase (2)	FWHM ^{c2}		$v_{50\%}^{c2}$		$v_{98\%}^{c2}$	
		avg (3)	max (4)	avg (5)	max (6)	avg (7)	max (8)
I Zw 1	neutral	202	654	-120	-326	-297	-635
F05189-2524	neutral	624	1728	-560	-1031	-1165	-2569
...	ionized	592	1591	-423	-989	-926	-1598
F07599+6508	neutral	275	682	-96	-315	-337	-793
...	ionized	310	641	-120	-839	-384	-1327
Mrk 231	neutral	395	1122	-416	-1112	-801	-1784
...	ionized	768	1397	-672	-1036	-1324	-2003
F13218+0552	neutral	189	386	-47	-185	-213	-524
...	ionized	641	1725	-169	-578	-714	-1897
F13342+3932	neutral	322	1027	-104	-432	-387	-1262
...	ionized	386	882	-144	-418	-473	-1167
PG1411+442	neutral	909	2148	-486	-1274	-1044	-1780
PG1613+658	ionized	409	609	-109	-578	-457	-704
PG1700+518	ionized	895	2179	-570	-854	-1331	-2627
F21219-1757	neutral	239	646	-230	-487	-441	-700

Note. — Column 2: Gas phase. Column 3–4: Mean and maximum (over all spaxels) of FWHM of velocity component 2 (c2), in /kms. Column 5–6: Mean and maximum values (over all spaxels) of c2 central velocity, in /kms. For the neutral phase, all components are combined in each spaxel into an optical depth weighted cumulative velocity distribution. The averages are taken over spaxels with $v_{50\%} < 0 \text{ km s}^{-1}$. For the ionized phase, only the c2 is used; with the exceptions of PG1613+658 and PG1700+518, the averages are taken over spaxels with $v_{50\%}^{c2} < 0 \text{ km s}^{-1}$. For PG1613+658 and PG1700+518, spaxels with $v_{50\%}^{c2} > 0 \text{ km s}^{-1}$ are included, but the velocities are multiplied by -1 so that the red and blue outflow components can be combined into a single average. Column 7–8: Mean and maximum of $v_{98\%} \equiv v_{50\%} - 2\sigma$. σ is the average velocity above and below $v_{50\%}$ that encompasses 34% of the cumulative velocity distribution: the area between $v_{50\%} \pm \sigma$ contains 68% of the distribution. As for $v_{50\%}$, the redshifted ionized gas spaxels in PG1700+518 have their distribution flipped in sign and combined with the blueshifted components.

Table 5
Mass, Momentum, and Energy

Galaxy (1)	phase (2)	R_{obs} (kpc) (3)	r_{wind} (kpc) (4)	$\log[f_{H\alpha}/(\text{erg s}^{-1} \text{cm}^{-2})]$ (5)	$\log(M/M_{\odot})$ (6)	$\log[(dM/dt)/(\text{M}_{\odot} \text{ yr}^{-1})]$ (7)	$\log[p/(\text{dyne s})]$ (8)	$\log[(c dp/dt)/L_{\odot}]$ (9)	$\log(E/\text{erg})$ (10)	$\log[(dE/dt)/(\text{erg s}^{-1})]$ (11)
I Zw 1	neutral	5.1	5.5	...	$8.77^{+0.06}_{-0.03}$	$1.38^{+0.10}_{-0.06}$	$49.41^{+0.10}_{-0.06}$	$11.61^{+0.15}_{-0.09}$	$56.79^{+0.12}_{-0.09}$	$42.14^{+0.18}_{-0.12}$
F05189-2524	neutral	2.7	3.0	...	$8.58^{+0.03}_{-0.02}$	$1.98^{+0.05}_{-0.03}$	$49.75^{+0.05}_{-0.03}$	$12.66^{+0.06}_{-0.03}$	$57.52^{+0.06}_{-0.03}$	$43.58^{+0.07}_{-0.04}$
...	ionized	2.8	3.0	-13.21	$7.36^{+0.06}_{-0.14}$	$0.40^{+0.07}_{-0.14}$	$48.16^{+0.07}_{-0.14}$	$10.78^{+0.07}_{-0.14}$	$55.55^{+0.07}_{-0.14}$	$41.32^{+0.07}_{-0.13}$
...	molecular	...	< 1	...	$8.28^{+0.38}_{-0.38}$	$2.43^{+0.03}_{-0.29}$...	$12.72^{+0.08}_{-0.25}$...	$43.20^{+0.10}_{-0.25}$
...	total	$8.77^{+0.16}_{-0.09}$	$2.57^{+0.03}_{-0.19}$	$49.76^{+0.05}_{-0.03}$	$13.00^{+0.05}_{-0.11}$	$57.53^{+0.06}_{-0.03}$	$43.73^{+0.06}_{-0.07}$
F07599+6508	neutral	7.5	8.1	...	$9.27^{+0.09}_{-0.09}$	$1.27^{+0.39}_{-0.12}$	$49.46^{+0.39}_{-0.12}$	$11.20^{+0.19}_{-0.12}$	$57.24^{+0.19}_{-0.12}$	$41.81^{+0.44}_{-0.17}$
...	ionized	7.0	8.1	-15.23	$7.50^{+0.06}_{-0.15}$	$-0.64^{+0.06}_{-0.19}$	$47.56^{+0.06}_{-0.19}$	$9.45^{+0.10}_{-0.33}$	$54.65^{+0.10}_{-0.33}$	$39.95^{+0.12}_{-0.32}$
...	total	$9.27^{+0.09}_{-0.09}$	$1.27^{+0.38}_{-0.12}$	$49.47^{+0.38}_{-0.12}$	$11.21^{+0.19}_{-0.12}$	$57.24^{+0.19}_{-0.12}$	$41.82^{+0.44}_{-0.17}$
Mrk 231	neutral	3.4	3.6	...	$8.84^{+0.02}_{-0.02}$	$2.00^{+0.03}_{-0.02}$	$49.85^{+0.03}_{-0.02}$	$12.54^{+0.05}_{-0.03}$	$57.46^{+0.05}_{-0.03}$	$43.35^{+0.06}_{-0.04}$
...	ionized	2.9	1.3	-14.71	$5.88^{+0.05}_{-0.04}$	$-0.30^{+0.06}_{-0.02}$	$47.10^{+0.06}_{-0.05}$	$10.37^{+0.06}_{-0.05}$	$54.78^{+0.06}_{-0.05}$	$41.18^{+0.06}_{-0.05}$
...	molecular	...	< 1	...	$9.04^{+0.07}_{-0.03}$	$3.04^{+0.02}_{-0.06}$...	$13.34^{+0.05}_{-0.18}$...	$43.92^{+0.11}_{-0.16}$
...	total	$9.25^{+0.05}_{-0.02}$	$3.08^{+0.01}_{-0.06}$	$49.85^{+0.03}_{-0.02}$	$13.40^{+0.05}_{-0.15}$	$57.47^{+0.05}_{-0.03}$	$44.02^{+0.09}_{-0.12}$
F13218+0552	neutral	11.3	12.0	...	$8.68^{+0.26}_{-0.39}$	$0.93^{+0.35}_{-1.09}$	$49.30^{+0.35}_{-1.09}$	$11.08^{+0.39}_{-1.52}$	$56.60^{+0.38}_{-1.01}$	$41.48^{+0.41}_{-1.39}$
...	ionized	11.5	12.0	-13.76	$9.21^{+0.04}_{-0.11}$	$1.03^{+0.04}_{-0.09}$	$49.40^{+0.04}_{-0.09}$	$10.80^{+0.04}_{-0.07}$	$56.18^{+0.04}_{-0.07}$	$40.87^{+0.05}_{-0.06}$
...	total	$9.32^{+0.08}_{-0.11}$	$1.29^{+0.19}_{-0.24}$	$49.65^{+0.19}_{-0.24}$	$11.27^{+0.29}_{-0.44}$	$56.74^{+0.30}_{-0.46}$	$41.58^{+0.36}_{-0.64}$
F13342+3932	neutral	9.2	10.7	...	$8.50^{+0.17}_{-0.07}$	$0.71^{+0.22}_{-0.15}$	$49.03^{+0.22}_{-0.15}$	$10.91^{+0.24}_{-0.22}$	$56.80^{+0.24}_{-0.32}$	$41.83^{+0.27}_{-0.38}$
...	ionized	7.9	10.7	-13.15	$9.17^{+0.03}_{-0.04}$	$1.37^{+0.03}_{-0.04}$	$49.69^{+0.03}_{-0.04}$	$11.38^{+0.03}_{-0.04}$	$56.71^{+0.03}_{-0.04}$	$41.54^{+0.03}_{-0.05}$
...	total	$9.25^{+0.04}_{-0.04}$	$1.46^{+0.05}_{-0.04}$	$49.78^{+0.05}_{-0.04}$	$11.51^{+0.08}_{-0.06}$	$57.06^{+0.15}_{-0.15}$	$42.01^{+0.19}_{-0.21}$
PG1411+442	neutral	2.8	3.2	...	$8.42^{+0.11}_{-0.12}$	$1.68^{+0.15}_{-0.11}$	$49.47^{+0.15}_{-0.11}$	$12.57^{+0.20}_{-0.13}$	$57.41^{+0.19}_{-0.13}$	$43.65^{+0.24}_{-0.17}$
PG1613+658	ionized	7.5	8.0	-14.11	$7.73^{+0.15}_{-0.30}$	$0.04^{+0.16}_{-0.36}$	$48.23^{+0.16}_{-0.36}$	$9.98^{+0.17}_{-0.38}$	$55.18^{+0.17}_{-0.38}$	$40.11^{+0.15}_{-0.32}$
PG1700+518	ionized	9.7	10.0	-12.89	$9.58^{+0.14}_{-0.09}$	$2.36^{+0.14}_{-0.10}$	$50.65^{+0.14}_{-0.10}$	$12.87^{+0.14}_{-0.10}$	$58.16^{+0.14}_{-0.10}$	$43.53^{+0.15}_{-0.11}$
F21219-1757	neutral	5.5	5.9	...	$8.79^{+0.09}_{-0.06}$	$1.56^{+0.12}_{-0.12}$	$49.62^{+0.12}_{-0.12}$	$11.87^{+0.16}_{-0.19}$	$57.04^{+0.16}_{-0.19}$	$42.41^{+0.20}_{-0.25}$

Note. — Column 2: Gas phase. Column 3–4: Maximum observed wind radius (in projection) and assumed wind radius, in kpc. Column 5: Logarithm of the H α flux in the wind, corrected for reddening using the Balmer decrement. For F07599+6508, the extincted flux is listed because the spectrum contains only one Balmer line. Column 6–11: Logarithms of the wind mass, momentum, energy, and their outflow rates, computed using a time-averaged thin shell model that depends inversely on the assumed shell radius (§ 3.2; Rupke et al. 2005c; Shih & Rupke 2010; Rupke & Veilleux 2013b). The ionized gas values depend on electron density as n_e^{-1} . For quasars with [S II] 6717, 6731 Å measurements, n_e is calculated on a spaxel-by-spaxel basis; for others $n_e = 100 \text{ cm}^{-2}$ is assumed (§ 2.3.2). The neutral gas values depends on ionization fraction, Na abundance, metallicity, and Na dust depletion (§ 3.2 and Rupke et al. 2005b). Molecular gas values are from González-Alfonso et al. (2017).

Table 6
Percent of Mass, Momentum, and Energy in Each Phase

Galaxy (1)	Phase (2)	M (3)	dM/dt (4)	p (5)	dp/dt (6)	E (7)	dE/dt (8)
F05189-2524	neutral	64.0	26.1	...	46.6	...	70.2
...	ionized	3.9	0.7	...	0.6	...	0.4
...	molecular	32.1	73.2	...	52.8	...	29.5
F07599+6508	neutral	<98.3	<98.8	<98.8	<98.3	<99.7	<98.6
...	ionized	>1.7	>1.2	>1.2	>1.7	>0.3	>1.4
Mrk 231	neutral	38.6	8.4	...	13.8	...	21.3
...	ionized	0.0	0.0	...	0.1	...	0.1
...	molecular	61.3	91.6	...	86.1	...	78.5
F13218+0552	neutral	22.9	44.4	44.4	65.4	72.6	80.2
...	ionized	77.1	55.6	55.6	34.6	27.4	19.8
F13342+3932	neutral	17.7	18.0	18.0	25.4	55.3	65.7
...	ionized	82.3	82.0	82.0	74.6	44.7	34.3

Note. — Column 2: Gas Phase. Column 3–8: Percent of the mass, momentum, energy, and their outflow rates in each phase. Molecular gas properties are from [González-Alfonso et al. \(2017\)](#). For F07599+6508, the ionized gas measurements are not extinction corrected, so the neutral values are upper limits and the ionized values are lower limits to the true values.

Table 7
Large-Scale Seyfert Galaxy Outflows

Galaxy (1)	Type (2)	dM/dt ($M_{\odot} \text{ yr}^{-1}$) (3)	$\log[(dE/dt)/$ (erg s^{-1})] (4)	$\log(M_{\text{BH}}/$ $M_{\odot})$ (5)	$\log[L_{\text{AGN}}/$ (erg s^{-1})] (6)	σ (km s^{-1}) (7)	References (8)
NGC 1068	2	76	42.87	$6.934^{+0.015}_{-0.015}$	44.95 ± 0.50	176 ± 9	b, C, D, ff, 3, 7
NGC 1266	2	110	41.04	$6.738^{+0.441}_{-0.441}$	43.53 ± 0.30	94 ± 5	a, A, dd, 1
Mrk 79	1	10	40.68	$7.612^{+0.445}_{-0.565}$	44.65 ± 0.18	129 ± 10	d, F, gg, 2, 5
NGC 2992	2	168	42.54	$7.703^{+0.442}_{-0.443}$	44.48 ± 0.50	160 ± 17	d, D, dd, 5, 8
NGC 3783	1.5	3.5	40.99	$7.367^{+0.442}_{-0.492}$	43.70 ± 0.25	110 ± 19	c, D, gg, 2, 5
NGC 4151	1.5	3	41.63	$7.553^{+0.441}_{-0.456}$	43.28 ± 0.28	96 ± 10	b, B, aa, 2, 5
NGC 4253	1	0.78	...	$6.822^{+0.443}_{-0.444}$	43.66 ± 0.21	93 ± 32	c, G, bb, 2, 5
NGC 4388	2	0.02	37.30	$6.929^{+0.010}_{-0.010}$	44.68 ± 0.52	99 ± 9	b, I, ee, 3, 7
Circinus	1	8.0	40.00	$6.230^{+0.092}_{-0.084}$	43.30 ± 0.30	149 ± 18	c, J, cc, 4
NGC 5548	1.5	9.5	41.47	$7.718^{+0.440}_{-0.440}$	44.29 ± 0.35	193 ± 11	b, H, bb, 2, 5
NGC 6814	1.5	10.5	41.05	$7.163^{+0.442}_{-0.493}$	43.24 ± 0.34	106 ± 17	c, D, bb, 2, 5
NGC 7469	1	5.6	40.92	$6.979^{+0.441}_{-0.460}$	44.62 ± 0.20	130 ± 6	b, D, gg, 2, 5
NGC 7582	1	3.4	...	$7.740^{+0.111}_{-0.097}$	43.30 ± 0.30	148 ± 19	b, E, hh, 6

References. — **Seyfert type:** (a) [Davis et al. 2012](#); (b) [Osterbrock & Martel 1993](#); (c) [Véron-Cetty & Véron 2006](#); (d) NED. **Mass outflow rate:** (A) [Alatalo et al. 2015](#); (B) [Crenshaw et al. 2015](#); (C) [García-Burillo et al. 2014](#); (D) [Müller-Sánchez et al. 2011](#); (E) [Riffel et al. 2009](#); (F) [Riffel et al. 2013](#); (G) [Schönell et al. 2014](#); (H) [Schönell et al. 2017](#); (I) [Veilleux et al. 1999a](#); (J) [Zschaechner et al. 2016](#). **Black hole mass:** (aa) [Bentz et al. 2006](#); (bb) [Bentz et al. 2010](#); (cc) [Greenhill et al. 2003](#); (dd) [Gültekin et al. 2009](#); (ee) [Kuo et al. 2011](#); (ff) [Lodato & Bertin 2003](#); (gg) [Peterson et al. 2004](#); (hh) [Wold et al. 2006](#). **Bolometric AGN luminosity:** (1) [Alatalo et al. 2015](#); (2) [Bentz et al. 2013](#); (3) [Liu et al. 2009](#); (4) [Moorwood et al. 1996](#); (5) [Runnoe et al. 2012](#); (6) [Rivers et al. 2015](#); (7) [Schmitt et al. 2003](#); (8) [Ward et al. 1980](#).

Note. — Column 2: Seyfert type. Column 3–4: Mass and energy outflow rates. Error bars are not consistently available for these measurements; we assume 0.3 dex. Most estimates are based on ionized gas measurements. The exceptions are NGC 1068 (molecular and ionized gas measurements have been summed); NGC 1266 (only a molecular gas measurement is available); and Circinus (the molecular gas value is much greater than the ionized gas value). In most cases the ionized values are calculated geometrically and depend on the product of the electron density n_e and filling factor f , which is typically assumed to be $n_e f = 5 \text{ cm}^{-2}$. For consistency we have normalized geometric estimates to this value, except in the case of NGC 5548, for which f is calculated but not published. Some literature ionized gas estimates erroneously do not correct upward for mean particle mass; in these cases we multiply the published rates by 1.4. Column 5: Logarithm of the black hole mass. Errors from reverberation mapping (references aa, bb, and gg) have the uncertainty in the virial coefficient f added in quadrature ($\delta f = 0.44$; [Woo et al. 2010](#)). Column 6: Logarithm of the bolometric AGN luminosity, as determined from the infrared luminosity, 5100 Å luminosity, or [O III] luminosity, in order of preference. In one case, NGC 7582, the only available measurement is from X-rays. Errors for L_{AGN} determined from 5100 Å or [O III] combine the observational error and the scatter in the bolometric correction. Errors for L_{AGN} determined from the infrared or X-rays are not listed; the errors are assumed to be 0.3 dex. Column 7: Velocity dispersion, from HyperLeda ([Makarov et al. 2014](#)) for all sources but NGC 4253 ([Woo et al. 2010](#)) and NGC 1266 ([Cappellari et al. 2013](#)). Column 8: References for data in columns 2–6.

only the near side of the wind is observed. Real winds are almost certainly more complex. However, thick shell models (e.g., Rupke et al. 2005c) require knowledge of the wind’s density and/or radial distribution, which in turn requires more detailed spatial information than is available in the current data.

Some well-resolved winds are able to be fit with bi-conical or bipolar bubble models (e.g., Veilleux et al. 1994; Rupke & Veilleux 2013b; Fischer et al. 2013). Such models tend to better account for wind projection and often lead to higher values of mass, momentum, and energy (Rupke & Veilleux 2013b). There are indications of bipolar flows in at least two objects in our sample (including the PG1613+658 and PG1700+518), and there are further indications of minor axis collimation in others (§ 3.1). However, the canonical sign of bipolar shells, line splitting, is noticeably absent. Detailed model fits of bipolar bubbles or cones would thus need to fully explore the parameter space of possible geometries to address parameter degeneracies. For simplicity and consistency with previous studies and within the sample, the thin shell is used exclusively here. Fits to bipolar models are reserved for future work, possibly using data of higher spatial resolution.

The measurements of M , p , and E may be lower limits to the true values due to the fact that any spatially-unresolved outflow has been removed from the data. Thus, outflows at scales <0.5 kpc in the nearest systems, approaching 2–3 kpc in the most distant systems, are not considered here.

The maximum observed radius of each wind in two-dimensional projection (R_{obs}) is measured in each phase. The observed range of R_{obs} is 3–12 kpc. The (single) three-dimensional radius adopted for the SRFW model, r_{wind} , is a free parameter in the model. Adopting $r_{\text{wind}} = R_{\text{obs}}$ exactly results in edge effects: spaxels with projected radii $R = R_{\text{obs}}$ yield formally infinite velocities when they are deprojected. The radius adopted is thus slightly larger (by ~ 0.5 spaxel) than the observed radius. In most cases $r_{\text{wind}}^{\text{neutral}} = r_{\text{wind}}^{\text{ionized}}$ is adopted. One exception is Mrk 231; while there is blueshifted, AGN-photoionized emission at large radii, the line widths of this $R \sim 3$ kpc emission are very narrow and lie atop the southern arc of star formation in this galaxy. It is thus assumed that these spaxels represent AGN-photoionized gas that is forming stars, rather than an outflow.

The ionized gas flux in each wind (except in F07599+6508, for which there is only one Balmer line in the present data) is corrected using the extinction computed from the Balmer decrement and listed in Table 5. As described in § 2.3.2, Case B at 10^4 K and the Cardelli et al. (1989) extinction curve are assumed. This correction (to the flux in component 2, c2) is done on a spaxel-by-spaxel basis where possible and uses the extinction computed from the combined flux in both components (c1+c2; Figure 8). Spaxels with uncertain extinction values are corrected using the median extinction value in the host.

The outflowing ionized gas mass in each spaxel depends inversely on electron density n_e . The electron density measured in each spaxel (calculated as described in § 2.3.2 and shown in Figure 9) is used to calculate the gas mass. In the few spaxels where the [S II] fluxes are

too uncertain, a value of 100 cm^{-2} is used (near the measured sample median; § 2.3.2). This value is also assumed for the two systems without n_e measurements (Mrk 231 and PG1700+518).

The neutral gas masses are proportional to the measured column density of hydrogen (Rupke et al. 2005c). The hydrogen column density in turn is related to the measured Na column through the ionization fraction, the Na abundance relative to Solar and the galaxy’s metallicity, and the Na dust depletion (Rupke et al. 2005b). Solar metallicity is assumed (Rupke et al. 2008) and the values for ionization fraction, Na abundance, and Na dust depletion are taken from Rupke et al. (2005b).

Five quasar hosts have detections of both neutral and ionized outflows (though one, F07599+6508, does not have extinction-corrected outflow properties). Two hosts, F05189–2524 and Mrk 231, also have molecular phase outflow measurements of critical wind properties. The latest measurements from modeling of multiple OH absorption lines observed with *Herschel* are adopted (González-Alfonso et al. 2017). These molecular outflows have predicted sizes under <1 kpc. Their properties are listed alongside the neutral and ionized properties in Tables 5 and 6.

The four hosts with extinction-corrected ionized outflow measurements and measurements in multiple gas phases show that the ionized gas phase dominates the mass of the wind in 2/4 cases but is negligible in the other two. However, the neutral and molecular phases typically contribute most to the energetics. This illustrates the importance of multiphase observations of winds, even in AGN outflows that are often presumed to be dominated by ionized gas.

3.3. Outflow Properties vs. Black Hole Properties

Observational studies of outflow properties are useful for informing sub-grid prescriptions in cosmological simulations of galaxy formation and evolution if observed outflow properties correlate with host, AGN, or black hole properties. Previous studies have focused on how quasar-mode outflows depend on host or AGN properties (e.g., Sturm et al. 2011; Veilleux et al. 2013a; Spoon et al. 2013; Rupke & Veilleux 2013b; Harrison et al. 2014; Cicone et al. 2014; McElroy et al. 2015; Stone et al. 2016; Sun et al. 2017; Fiore et al. 2017). Since this sample of nearby luminous AGN has substantial ancillary data, and thus useful constraints on the central black hole (Table 1), this paper focuses on the dependence of outflow properties on black hole properties.

To probe this dependence across a significant dynamic range, however, a larger range of black hole mass is required. Table 7 lists the outflow and host galaxy properties in 13 nearby Seyfert galaxies with spatially-resolved outflows. The outflow properties are mostly based on ionized gas measurements of the NLR, except for those in NGC 1068, NGC 1266, and Circinus. The measurements of NGC 1266 and Circinus are of the molecular gas, which dominate the outflow mass and energy budgets. The measurements of NGC 1068 combine ionized and molecular gas. These NLR outflows have scales of 0.1 to a few kpc.

Figure 14 shows total mass outflow rate (summed over all gas phases) versus black hole mass. Error bars on the IFS data reflect statistical uncertainties in line fits to

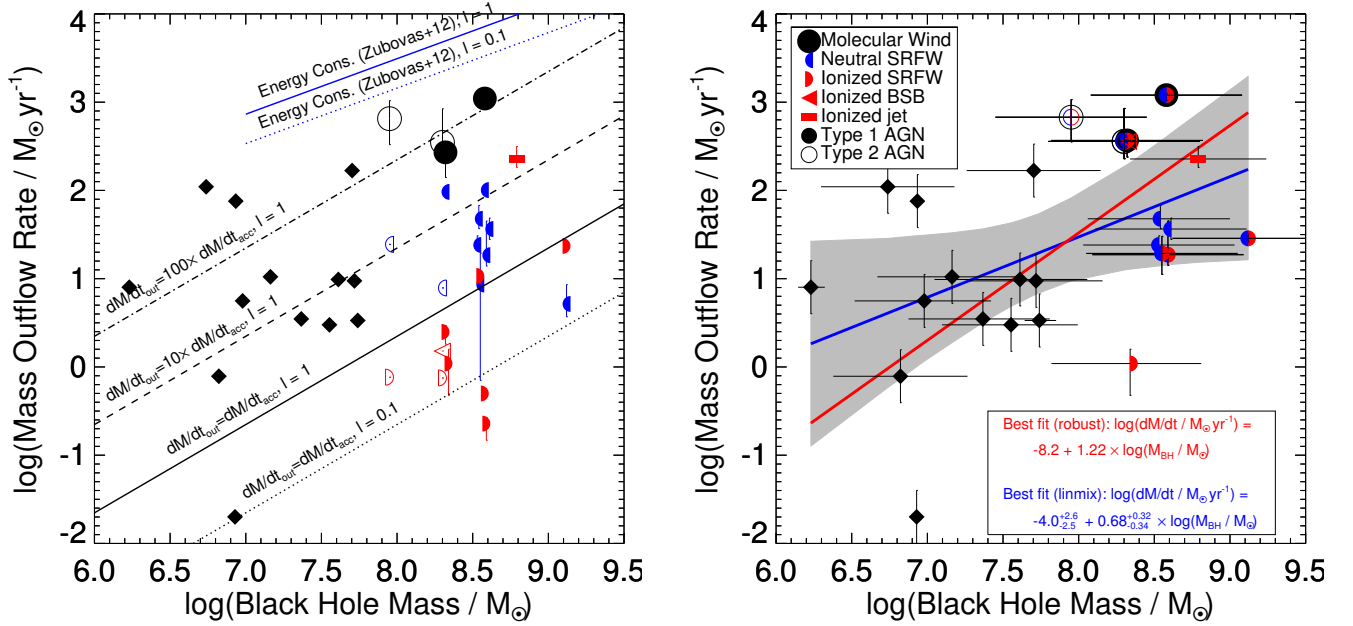


Figure 14. Mass outflow rates as a function of black hole mass for this sample, two Type 2 quasars (Rupke & Veilleux 2013b), and a sample of Seyfert galaxies with resolved outflows (shown as filled black diamonds; Table 7). **(Left)** Individual phases are shown. Ionized gas measurements in the Type 2 quasars and in F07599+6508 are lower limits because an extinction correction has not been performed. Ionized gas masses in the Type 2 quasars have been corrected to $n_e = 100 \text{ cm}^{-2}$ to match the typical value measured in the current sample (§ 2.3.2). Most quasar measurements result from single-radius free wind (SRFW) models, though one galaxy also has masses from a bipolar superbubble (BSB) fit (§ 3.2 and Rupke & Veilleux 2013b). Models for energy-conserving winds driven by high-velocity blast waves (Eddington ratios $l = 0.1$ and 1) are overplotted as blue solid and dotted lines (Zubovas & King 2012), as well as lines of constant values of mass outflow rate divided by accretion rate (for $l = 0.1$ or 1 and 10% efficiency of energy released by accretion) as black dotted, solid, dashed, and dotted-dashed lines. **(Right)** Mass fluxes have been added up across measured phases. Robust and Bayesian fits (the latter including intrinsic scatter with LINMIX_ERR; Kelly 2007) to the correlation between outflow rate and M_{BH} are shown. The contours show 2σ deviations from the median after applying the posterior distributions of slopes and intercepts to the measured dependent variables. The 95.5% range of correlation coefficients and slopes (-0.01 to 0.88 and -0.02 to 1.37 , respectively) shows a correlation at the 2σ level and a significant amount of intrinsic scatter (1.0 dex). Though the Zubovas & King (2012) models overpredict the mass outflow rates by 1–2 orders of magnitude, they do match the best-fit slope (0.63 in theory, 0.68 observed).

individual spaxels (as determined from Monte Carlo simulations in the case of absorption lines and least-square errors in the case of emission lines), which have been propagated and summed in quadrature across all outflowing spaxels. However, unquantified systematic errors (due to, e.g., uncertain 3D spatial distribution) could be larger than the measurement uncertainties.

Because of the significant intrinsic scatter in this plot that is not accounted for by the measurement errors, we estimate the strength and properties of a possible linear relationship using a Bayesian regression that fits the intrinsic scatter and uses a Gaussian mixture model for the intrinsic distribution of independent variables (LINMIX_ERR; Kelly 2007). The default mixture of three Gaussians and the Gibbs sampler are used. The resulting 95.5% (2σ) ranges for the correlation coefficient and slope are -0.01 to 0.88 and -0.02 – 1.37 , respectively, with medians in the posterior distributions of 0.50 and 0.68 . The median intrinsic scatter is 0.98 , meaning there are unaccounted-for variables that contribute significantly or that the error is underestimated. The best-fit linear regression line (using the medians and 1σ deviations from

the median of intercept and slope) is then

$$\log[(dM/dt)/(M_{\odot} \text{ yr}^{-1})] = - (4.0_{-2.5}^{+2.6}) + (0.68_{-0.34}^{+0.32}) \times \log(M_{\text{BH}}/M_{\odot}). \quad (9)$$

A robust fit that does not account for errors and bisects the fit of X on Y and Y on X gives a steeper slope of 1.2.

This statistical test points to a positive correlation between black hole mass and total mass outflow rate in this sample at 95.5% confidence, though the slope of this correlation is poorly constrained (95.5% range 0.0 – 1.4). It also suggests that either unaccounted-for systematic errors or other variables play a significant role in their relationship. For instance, while the relationship among the different gas phases is not fully understood spatially, it may be that adding the phases together means that some phases are counted twice. The ionization correction to the Na I D measurement tries to account for all gas phases, but it is entirely possible that the gas clouds traced by Na I D are not spatially coincident with those detected by ionized or molecular gas tracers. In fact, they are often spatially disjoint (Fig. 13). In this case adding together the masses inferred from different phases is appropriate, since they trace different parts of the wind.

Selection effects may also play a role. Since most or all galaxies host nuclear black holes, they will appear on

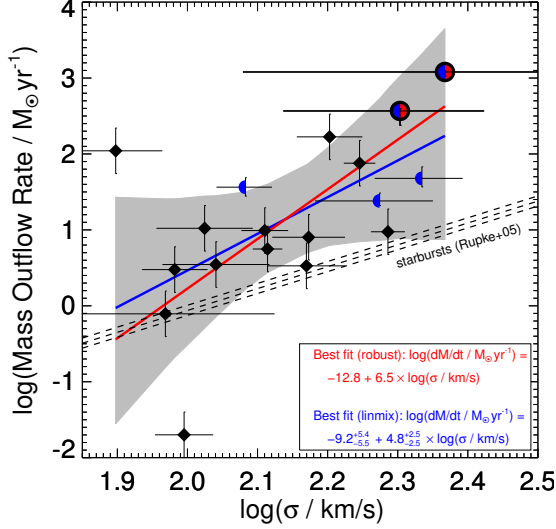


Figure 15. Mass outflow rates as a function of stellar velocity dispersion for quasars and Seyferts. See Figure 14 and § 3.3 for more information. The dashed lines show the relationship between these two quantities for starburst winds (slope 2.9; Rupke et al. 2005c) for three different values of $v_{\text{rot}}/2\sigma$ (0.42, 0.50, and 0.58). The correlation is not significant at the 2σ level, but the best-fit slope is consistent with an extrapolation from the slope of dM/dt vs. M_{BH} and the $M_{\text{BH}}-\sigma$ relation. It is apparent that AGN-driven outflows in massive black holes are driving mass out at greater rates than in pure starbursts.

this plot somewhere. Studies of galaxy-scale outflows in complete, unbiased samples of galaxies will show whether the outflows in this sample are simply the tip of the iceberg (i.e., there is a broad distribution of mass outflow rates extending to zero) or that the mass outflow rates measured here are representative of all AGN with high Eddington ratio.

Because black hole mass correlates with velocity dispersion, mass outflow rate should correlate with stellar velocity dispersion. Stellar velocity dispersion is known for only a subset of the current sample (Table 1). Figure 15 shows that there may be a correlation between these two quantities, but the correlation is not significant at the 2σ level. The 95.5% range of possible correlation coefficients and slopes is -0.08 to 0.97 and -0.7 to 10.6 . The best-fit line is

$$\log[(dM/dt)/(M_{\odot} \text{ yr}^{-1})] = - (9.2^{+5.4}_{-5.5}) + (4.8^{+2.5}_{-2.5}) \times \log[\sigma/(\text{km s}^{-1})]. \quad (10)$$

Based on the correlation between $\log(dM/dt)$ and $\log(M_{\text{BH}})$ and the $M_{\text{BH}}-\sigma$ relation (Gültekin et al. 2009), the slope should be 2.9 ± 1.5 , which is consistent with the fitted slope within the (large) errors.

Energy outflow rates are also published for most of the Seyferts in Table 7. The correlation between dE/dt and M_{BH} or σ (Figure 16) is more significant than the correlations with mass outflow rate. The posterior distributions of correlation coefficients and slopes for dE/dt vs. M_{BH} have a 95.5% range of 0.15 – 0.94 and 0.31 – 2.28 , respectively. For dE/dt vs. σ , these ranges are 0.08 – 0.98

and 1.1 – 17.3 . The best fit lines are

$$\log[(dE/dt)/(\text{erg s}^{-1})] = - (32.0^{+3.7}_{-3.8}) + (1.27^{+0.48}_{-0.47}) \times \log(M_{\text{BH}}/M_{\odot}), \quad (11)$$

and

$$\log[(dE/dt)/(\text{erg s}^{-1})] = - (23.0^{+7.8}_{-8.1}) + (8.7^{+3.7}_{-3.6}) \times \log[\sigma/(\text{km s}^{-1})], \quad (12)$$

the best-fit correlation coefficients are 0.61 and 0.68 , and the intrinsic scatter is 1.4 dex.

4. DISCUSSION

The following section addresses the implications of the outflow properties of the current sample and the observed correlations with black hole properties for the wind power source, quasar wind models, and quasar-mode feedback.

4.1. Wind Power Source

The quasars in this sample host both a starburst and a luminous AGN, and it is important to determine which power source is driving the observed large-scale outflows. Previous work has argued that the Mrk 231 outflow is powered primarily by the AGN (e.g., Fischer et al. 2010; Feruglio et al. 2010; Rupke & Veilleux 2011; Feruglio et al. 2015; Morganti et al. 2016). In PG1700+518 the culprit is clearly the jet spawned by black hole accretion, while in PG1613+658 the outflow is driven by the AGN within the narrow-line region.

In other systems (particularly F05189–2524 and PG1411+442, and to a lesser extent in F13218+0552 and F13342+3932) the velocities ($\langle v_{98\%} \rangle$) exceed those observed in local starbursts (e.g., Rupke et al. 2005c). Previous studies have found that velocities of kpc-scale outflows in AGN reach the highest velocities ($\sim 1000 \text{ km s}^{-1}$ or higher) only at quasar-like luminosities ($\sim 10^{45} \text{ erg s}^{-1}$), and that there is a correlation between outflow velocity and AGN luminosity (Sturm et al. 2011; Spoon et al. 2013; Veilleux et al. 2013a; Rupke & Veilleux 2013b; Harrison et al. 2014; Ciccone et al. 2014; Stone et al. 2016; González-Alfonso et al. 2017; Sun et al. 2017; Fiore et al. 2017). Figure 17 shows how velocity depends on AGN luminosity in IFS observations of ionized and neutral gas velocities in nearby Type 1 and 2 quasars and luminous starbursts (Rupke & Veilleux 2013b and this study). While there is still evidence that the highest outflow velocities only appear in quasars, there are many quasars with velocities comparable to those in starbursts. No correlation is evident. However, the dynamic range in luminosity of the current sample is relatively small.

To further quantify how these outflows relate to their potential power sources, Table 8 lists ratios of wind properties to properties of the star-forming host or AGN.

To compare to the star-forming host, the mass entrainment efficiency η (Rupke et al. 2005c) is computed as dM/dt normalized to the star formation rate, which comes in turn from the AGN fraction in Table 1 and the total infrared luminosity (Veilleux et al. 2009b). The mass, momentum, and energy outflow rates are also compared to predicted rates from the starburst itself (Leitherer et al. 1999; Heckman et al. 2015; González-Alfonso et al. 2017). (The AGN fraction for PG1411+442

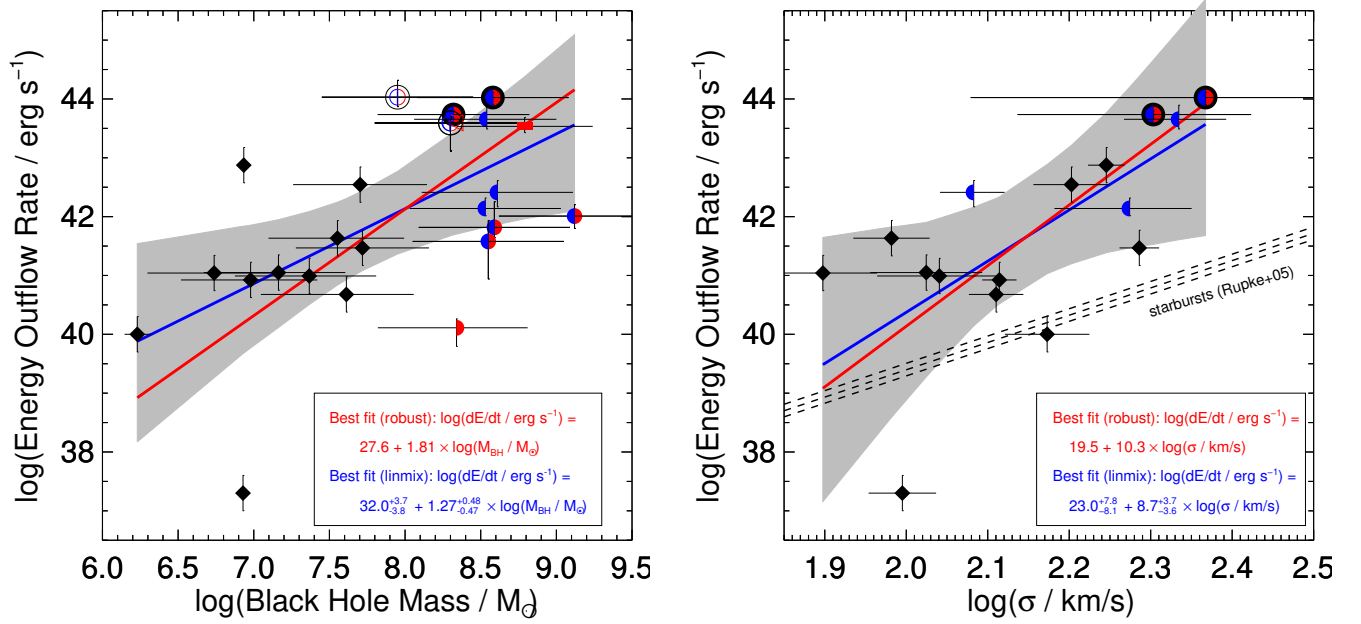


Figure 16. Energy outflow rates as a function of M_{BH} and σ . See Figures 14–15 and § 3.3 for more details. The correlations are significant at greater than 2σ , and the intrinsic scatter is 1.4 dex.

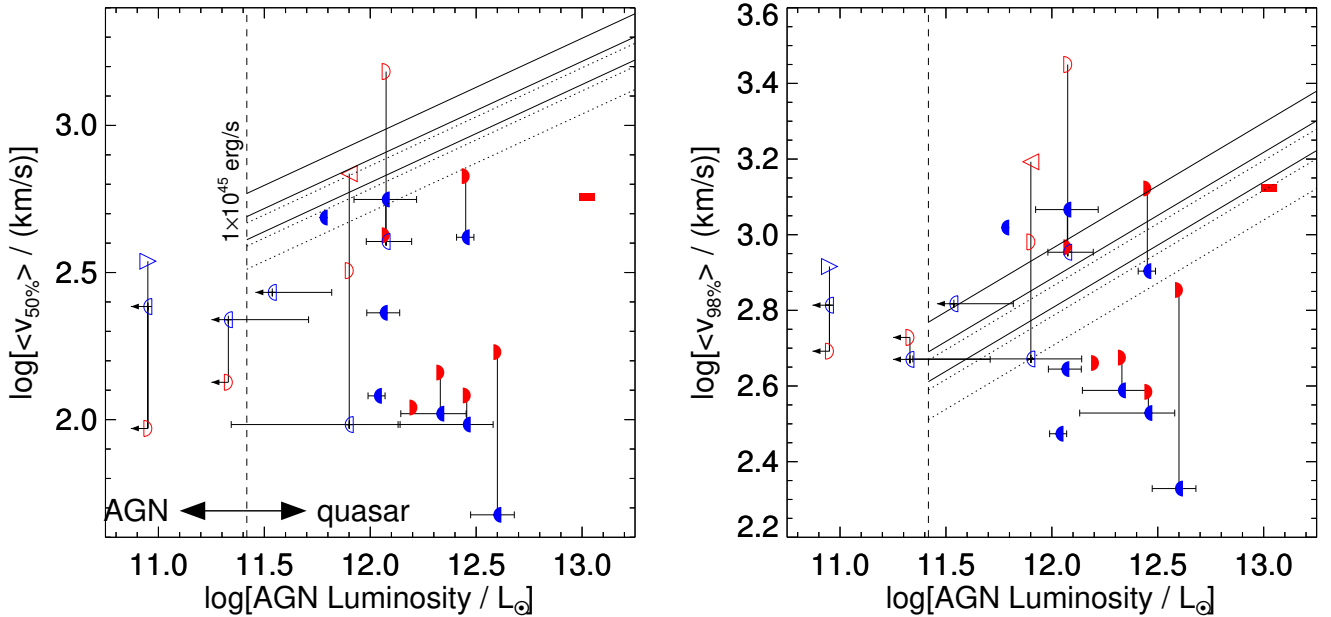


Figure 17. Spatially-averaged velocities ($v_{50\%}$ or $v_{98\%}$) vs. AGN luminosity from ionized and neutral IFS observations of nearby Type 1 and 2 quasars and starbursts (Rupke & Veilleux 2013b and this work). See Figure 14 for an explanation of symbols. Measurements of the same galaxy are connected by vertical solid black lines. The typical quasar threshold is labeled with a vertical dashed line. The prediction of an energy-conserving model from Zubovas & King (2012) is overlaid. Solid lines show predictions for black hole masses of $\log(M_{\text{BH}})=8.0, 8.5,$ and 9.0 ; a galaxy gas mass fraction $f_g = 0.1$ (typical for ULIRGs; Rupke et al. 2008); and ratio of gas density to background density of $f_c = 0.16$ (as in Zubovas & King 2012; see this paper for more details on f_g and f_c). The black hole mass is converted to velocity dispersion using the $M_{\text{BH}}-\sigma$ relation (Gültekin et al. 2009). Dotted lines show $f_g = 0.2$. There is evidence that the highest velocities are only observed in quasars, but not all quasars have high-velocity winds. No correlation is evident. Energy-conserving models can reproduce the highest velocities in many systems, but overpredict average velocities and even the highest velocities in many radio-quiet quasars.

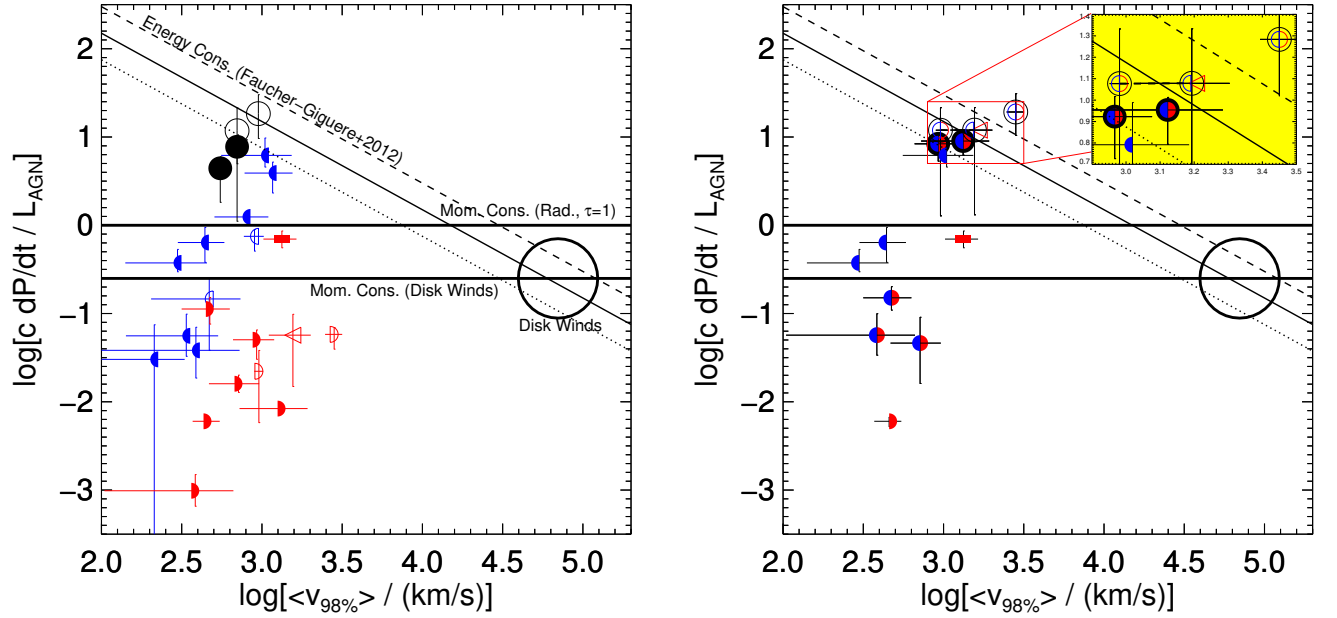


Figure 18. Spatially-averaged velocities ($v_{98\%}$) vs. momentum outflow rate normalized to AGN luminosity. The same galaxies as in Figure 17 are displayed, but the starbursts have been removed. On the left, individual phases are shown. On the right, the gas momenta have been added up across measured phases, and the maximum $\langle v_{98\%} \rangle$ across phases is used. Ionized gas measurements in the Type 2 quasars and in F07599+6508 are lower limits because extinction correction has not been performed. Models for energy-conserving winds driven by blast waves from high-velocity accretion disk winds are overplotted (velocities of $0.1c$, $0.2c$, and $0.5c$; Faucher-Giguère et al. 2012), as well as predictions based on pure momentum conservation from accretion disk winds (the circle shows the locus of representative accretion disk winds; Tombesi et al. e.g., 2015) or from radiation pressure (assuming one photon scattering, though more photon scattering can arise from high infrared opacities). While some Type 1 and 2 systems are consistent with energy-conserving models, half of the quasars have lower momentum boosts by 1 to several orders of magnitude. This suggests either a loss of wind momentum and energy or a different driving mechanism for the quasar wind.

Table 8
Power Sources and Feedback

Galaxy	phase	$\log[(dM/dt)/SFR]$	$\log[(dM/dt)/(dM/dt)_{SB}]$	$\log[(c dp/dt)/(3.5 \times L_{SB})]$	$\log[(dE/dt)/(dE/dt)_{SB}]$	$\log[(dM/dt)/(dM/dt)_{acc}]$	$\log[(c dp/dt)/L_{AGN}]$	$\log[(dE/dt)/L_{AGN}]$
(1)	(2)	(3)	(4)	(5)	(6)	(7)	(8)	(9)
I Zw 1	neutral	0.40	1.38	0.12	-0.28	1.51	-0.43	-3.48
F05189-2524	neutral	0.12	1.10	0.44	0.28	2.08	0.59	-2.08
...	ionized	-1.47	-0.49	-1.45	-1.99	0.49	-1.30	-4.34
...	molecular	0.57	1.55	0.50	-0.10	2.53	0.65	-2.45
...	total	0.70	1.68	0.77	0.43	2.66	0.92	-1.92
F07599+6508	neutral	-0.89	0.09	-1.32	-1.78	0.98	-1.25	-4.23
...	ionized	-2.79	-1.82	-3.07	-3.64	-0.93	-3.01	-6.09
...	total	-0.88	0.10	0.50	-1.78	1.03	-1.25	-4.22
Mrk 231	neutral	-0.24	0.74	-0.06	-0.33	1.72	0.09	-2.68
...	ionized	-2.54	-1.56	-2.23	-2.50	-0.58	-2.08	-4.85
...	molecular	0.80	1.78	0.73	0.24	2.76	0.89	-2.12
...	total	0.84	1.82	0.80	0.34	2.80	0.95	-2.01
F13218+0552	neutral	-1.15	-0.17	-1.37	-2.04	0.50	-1.52	-4.70
...	ionized	-1.05	-0.07	-1.64	-2.65	0.60	-1.80	-5.31
...	total	-0.80	0.18	0.74	-1.94	0.91	-1.33	-4.61
F13342+3932	neutral	-1.44	-0.46	-1.61	-1.77	0.55	-1.42	-4.09
...	ionized	-0.78	0.20	-1.14	-2.05	1.21	-0.95	-4.37
...	total	-0.70	0.28	0.74	-1.58	1.32	-0.82	-3.91
PG1411+442	neutral	2.07	0.79	-1.71
PG1613+658	ionized	-1.46	-0.48	-2.11	-2.83	0.00	-2.22	-5.68
PG1700+518	ionized	0.23	1.21	-0.10	-0.03	1.50	-0.16	-3.07
F21219-1757	neutral	-0.12	0.86	-0.18	-0.71	1.67	-0.20	-3.24

Note. — Column 2: Gas phase. Column 3: Logarithm of mass outflow rate normalized to the star formation rate. Column 4: Logarithm of the mass outflow rate divided by the hot gas mass production rate from a continuous starburst (Leitherer et al. 1999). Column 5: Logarithm of the momentum outflow rate divided by the momentum injection rate from a continuous starburst (Leitherer et al. 1999; Veilleux et al. 2005; Heckman et al. 2015; González-Alfonso et al. 2017). Column 6: Logarithm of the energy outflow rate divided by the mechanical energy production rate from a continuous starburst (Leitherer et al. 1999). Column 7: Logarithm of the mass outflow rate divided by the accretion rate, calculated using a 10% efficiency of radiative energy released by accretion. Column 8: Logarithm of the momentum outflow rate divided by the momentum input rate if the AGN bolometric luminosity accelerates the wind and each photon is intercepted once. Column 9: Logarithm of the energy outflow rate divided by the AGN luminosity.

is formally 100%, so these quantities are not calculated.) η ranges from 0.03 to 7, with a median value of 0.8. This median is a factor of several higher than in the purely neutral phase of starburst-driven winds in ULIRGs (Rupke et al. 2005c). The median increase in wind mass from entrainment, compared to the expected input from starbursts, is a factor of 7, which is again higher than in ULIRG starbursts (Rupke et al. 2005c). 7/9 systems require more momentum than can be input by the starburst (without multiple photon scatterings from the radiation field), and one of the remaining two is AGN-driven (PG1613+658). 3/9 require more energy than produced by the starburst, and 5/9 require more than 20% of the starburst energy (meaning very little energy can be lost to radiation or dissipative shocks). Two systems, F07599+6508 and F13218+0552, have winds that could plausibly be explained by starbursts. Of the four remaining systems that require $< 10\%$ of the starburst energy, one is clearly an AGN outflow (PG1613+658) and in another the ionized outflow rates are lower limits.

This conclusion that the large-scale outflows in this sample are largely powered by the AGN rather than star formation are strengthened by comparing to starbursts of similar mass. Though the errors on the slopes are large, the observed correlations between quasar+Seyfert outflow rates and σ may be steeper than the correlations between $\log(dM/dt)$ or $\log(dE/dt)$ and logarithm of circular velocity, $\log(v_c)$, determined for starbursts (slopes 2.9 ± 0.7 and 4.64 ± 0.8 , respectively; Rupke et al. 2005c). Figures 15 and 16 show the relationship between

$\log(dM/dt)$ and $\log(v_c)$ for starbursts, after applying the definition $v_c^2 \equiv 2\sigma^2 + v_{\text{rot}}^2$. The result is insensitive to the choice of $v_{\text{rot}}/2\sigma$, which is 0.42 on average for ULIRGs (Dasyra et al. 2006b) and 0.58 for the Seyferts in Table 7 (based on HyperLeda data). The observed best-fit steep correlations with σ imply that while NLR outflows in nearby Seyferts are not too different from their starburst counterparts, galaxies hosting luminous black holes are ejecting mass and energy at rates many times those of starburst hosts of similar σ .

The conclusion is that most or all of the observed outflows are AGN-driven; however, star formation could play a role in driving the lowest-velocity and/or lowest-energy outflows.

4.2. Comparison to Quasar Wind Models

Models for the powering of quasar-driven, large-scale outflows can be coarsely grouped into two categories: energy-conserving blast waves powered by small-scale accretion disk winds (e.g., King et al. 2011; Faucher-Giguère et al. 2012; Zubovas & King 2012; Wagner et al. 2013; Hopkins et al. 2016; Gaspari & Sądowski 2017) and momentum-conserving winds driven by multiple photon scatterings in dusty gas with high optical depths in the infrared (e.g., Thompson et al. 2015; Ishibashi & Fabian 2015; Costa et al. 2017). Besides the high observed velocities in quasar-mode winds, both types of models have striven to explain large “momentum boosts”: the momentum outflow rate is factors of a few to a few tens larger than the outflow rate expected from pure radiation pressure driving assuming one photon scattering (Sturm

et al. 2011; Veilleux et al. 2013a; Spoon et al. 2013; Rupke & Veilleux 2013b; Cicone et al. 2014; Stone et al. 2016; González-Alfonso et al. 2017). However, these observational studies have contained few examples of Type 1 quasars.

To facilitate comparison to wind models and to assess feedback (§ 4.3), the outflow rate is compared to the accretion rate, and the momentum and energy outflow rate are compared to the AGN luminosity, in Table 8.

The momentum boosts in the neutral and ionized phases of nearby quasar winds (Table 8 and Figure 18) show a wide dynamic range, from $(c \, dp/dt)/L_{\text{AGN}} = 0.001$ to 6. For comparison, molecular gas measurements for this sample are taken to be total momentum outflow rates and maximum velocities from González-Alfonso et al. (2017). Momentum boosts tend to be higher, but velocities lower, in the molecular phase of individual systems. When all phases are summed, half of the IFS quasar sample shows $(c \, dp/dt)/L_{\text{AGN}} > 1$, with a range of 0.01–20.

Roughly half the sample lies 2–3 orders of magnitude below predictions of the momentum boost from energy-conserving blast wave models (Faucher-Giguère et al. 2012). This implies either that the blast wave is not energy-conserving in these systems, that some other mechanism drives the wind (such as radiation pressure), or that another phase dominates the momentum budget. Measurements of one of these systems, I Zw 1, have not detected a molecular outflow, though the neutral outflow velocities in this system are comparable to the disk velocities and the outflow could be hidden in the core of a molecular line profile (Veilleux et al. 2013a; Cicone et al. 2014).

Comparison of the observed velocities at a given L_{AGN} (Figure 17) with energy-conserving models (Zubovas & King 2012) show that the models can reproduce the spatially-averaged highest velocities in most, though not all, quasars. These models also match the best-fit slope in the dM/dt vs. M_{BH} plane (Figure 14): 0.63 (theory) for 0.68 (observed). However, these models over-predict the average velocity in most systems and the highest velocities in some Type 1 quasars. They also over-predict the observed mass outflow rates by 1–2 orders of magnitude (Figure 14). However, the observed mass outflow boost in AGN-driven winds compared to starburst-only winds (0.01–10; § 4.1) is of the same order of magnitude as predicted by some simulations (Hopkins et al. 2016).

The efficiencies with which the AGNs power these winds are high in the sense that the mechanical energy required is typically a very small fraction of the AGN luminosity. The range of $(dE/dt)/L_{\text{AGN}}$ for both Seyferts and quasars is large, with most sources in the range 0.002% to 2%; such values are low enough for models to successfully drive AGN outflows (e.g., Hopkins & Elvis 2010; Zubovas & King 2012) and are similar to efficiencies assumed in numerical simulations (e.g., Hopkins et al. 2016). There is no correlation of this efficiency measure with M_{BH} (Figure 19), L_{AGN} , or Eddington ratio.

The conclusion is that it is difficult to distinguish among competing models or constrain individual models. However, none of these models make predictions about how outflow properties scale with black hole mass – such predictions would optimally leverage the results of the current study.

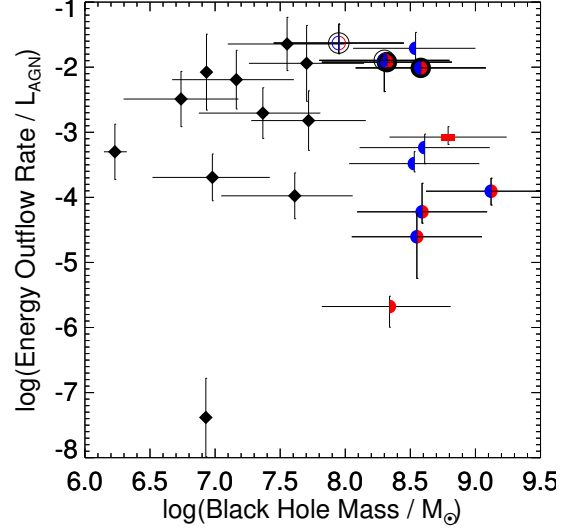


Figure 19. Energy outflow rate divided by (bolometric) AGN luminosity as a function of black hole mass. There is no dependence on M_{BH} , and the values are consistent with (or lower than) values inferred from or assumed by current models and simulations (e.g., Hopkins & Elvis 2010; Zubovas & King 2012; Hopkins et al. 2016). Though the plots are not shown, there is similarly no dependence on L_{AGN} or Eddington ratio.

4.3. Kpc-Scale Quasar-Mode Winds as AGN Feedback

A key remaining question is how these large-scale, quasar-driven outflows will affect the star formation and AGN activity in their hosts. This question is difficult to answer conclusively with the current data.

It is clear that in an absolute sense, the most massive black holes produce the most massive and energetic outflows. High-velocity, high-momentum boost feedback, as observed in part of this sample, may be the most effective at shaping the $M_{\text{BH}}-\sigma$ relation at high black hole masses in simulations, as well (Anglés-Alcázar et al. 2017). In essence, these outflow rates illustrate how well the black hole, through its current accretion rate, is moving away gas that could at some future time feed the black hole. This future potential depends on (1) the uncertain timescales for gas at large radii to inflow to the accretion disk and then to the black hole and (2) what fraction of gas at large radii will actually fall into the black hole at some future time.

A possible relative measure of feedback on the AGN itself is the mass outflow rate divided by the present black hole accretion rate. In the quasar+Seyfert sample, this ratio is mostly in the range 1–1000, which is larger than at radii < 100 pc in the simulations of Hopkins et al. (2016). Figure 20 shows how $(dM/dt)_{\text{out}}/(dM/dt)_{\text{acc}}$ depends on black hole mass and Eddington ratio. There is not a significant correlation with M_{BH} . However, the Seyfert subsample on average has higher $(dM/dt)_{\text{out}}/(dM/dt)_{\text{acc}}$ and lower M_{BH} than the quasar subsample. The correlation with Eddington ratio is almost 2σ (using Bayesian fitting as in § 3.3), with a median slope of -1.0 and a 95.5% range of -2.4 to 0.1. However, the Bayesian test does not account for the fact that the variables are not completely independent, since both depend on L_{AGN} ($dM/dt_{\text{acc}} \sim L_{\text{AGN}}$ and Edding-

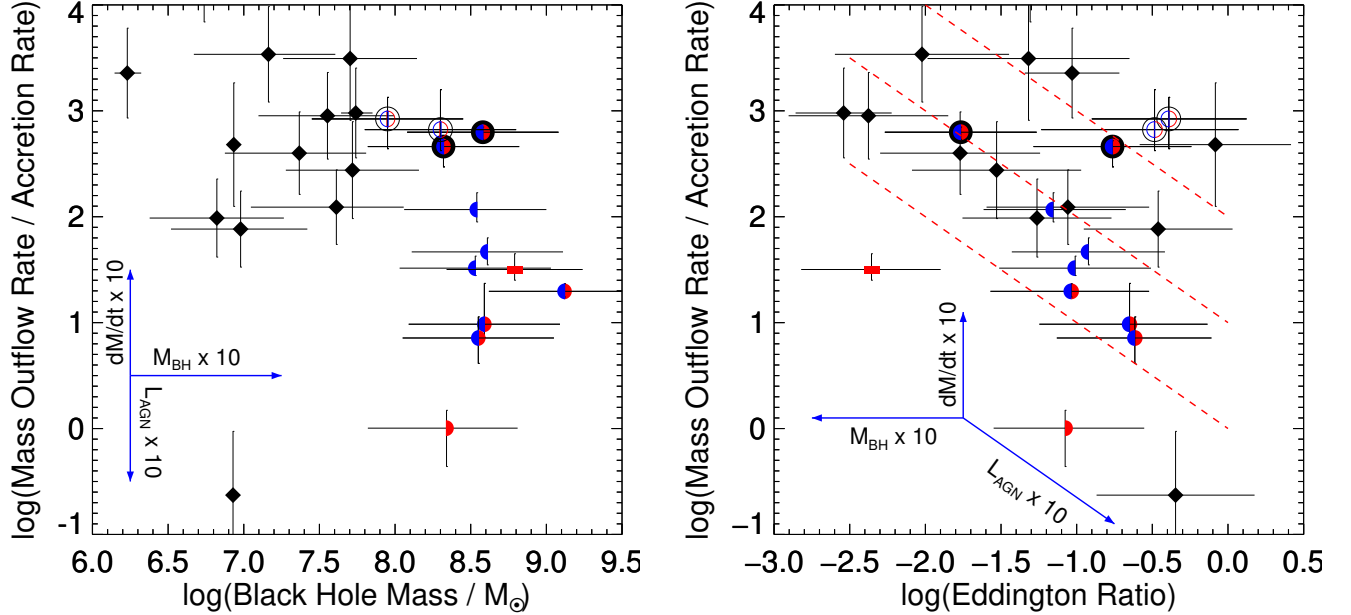


Figure 20. Mass outflow rates, normalized to the accretion rates of individual AGNs (assuming 10% efficiency of radiative energy released by accretion; Table 8), as a function of black hole mass and Eddington ratio. Arrows show how an order of magnitude change in mass outflow rate, black hole mass, or AGN luminosity affects the position of points. The ratio of mass out (on large scales) to mass in (to the black hole) may decrease with increasing black hole mass and increasing Eddington ratio. Another possible interpretation is that the radiative efficiency increases with black hole mass, such that more massive black holes have lower accretion rates for a given luminosity. Finally, in the right panel, dashed lines of constant dM/dt and M_{BH} , but varying L_{AGN} , show that accretion variations (reflected in changes in L_{AGN}) on timescales much shorter than the outflow dynamical time could explain some of the scatter or apparent correlation.

ton ratio is proportional to L_{AGN}).

We conclude that there is weak evidence of inverse correlations of $\frac{(dM/dt)_{out}}{(dM/dt)_{acc}}$ with M_{BH} and Eddington ratio. If such correlations exist, then one consequence could be that relative feedback (gas out on large scales over gas in at small scales) is higher in systems with lower Eddington ratio and lower black hole mass. Alternatively, it could be that the assumption of a constant radiative efficiency from accretion (how well the black hole converts accretion energy into luminosity) is incorrect. Instead, the efficiency may be higher in higher-mass black holes (Davis & Laor 2011). Higher radiative efficiency means a lower accretion rate $(dM/dt)_{acc}$ produces the same luminosity L_{AGN} , which could remove any correlation of $\frac{(dM/dt)_{out}}{(dM/dt)_{acc}}$ with M_{BH} . A higher efficiency could result from higher black hole spin, since in standard thin-disk accretion (Shakura & Sunyaev 1973) the efficiency depends on the spin (Reynolds 2013). However, current measurements of black hole spin do not show higher spin in higher mass black holes (Reynolds 2013).

The issue of timescale is also an important consideration. Quasar outflows are powered by current and past AGN activity. The dynamical timescales of these flows are of order 1–100 Myr, while AGN accretion may have a smaller duty cycle of ~ 0.1 Myr (e.g., Schawinski et al. 2015; King & Nixon 2015). Thus, the accretion rate (and thus the AGN luminosity and Eddington ratio) may change significantly on shorter timescales than the outflow. Some of the scatter (and the correlation itself) in the right panel of Figure 20 could result from short timescale variations of L_{AGN} if dM/dt_{out} and M_{BH}

indeed vary on longer timescales.

As with the other correlations found in this work, selection biases likely exist, and larger samples are needed. For instance, the lower regions of Figure 20 could be occupied by galaxies with lower mass outflow rates but similar accretion rates and black hole masses (e.g., the radio-mode feedback regime in radiatively-inefficient accretion modes), which could also fill in other parts of Figures 14–16. An open question is whether the distributions in outflow properties, taken over all galaxies with accreting black holes, are continuous or significantly bimodal. For instance, in a hypothetical on-or-off model, outflows are either present and look like the ones present here, or they are absent and any outflow rates are exactly zero. The result would be a bimodal distribution in outflow rates. In this on-or-off model, the correlations presented here may accurately describe active feedback modes.

5. SUMMARY

Quasar-mode feedback takes the form of kpc-scale, massive, high-velocity winds driven by radiation and energetic winds from the hearts of radio-quiet quasars. These winds potentially play a crucial role in feedback that regulates the growth of supermassive black holes and star formation in galaxies. This study reports on the first multiphase study of such winds in a sample of nearby Type 1 quasars. The subsample, which is selected from the QUEST sample of optically- and IR-selected quasars, consists of 10 quasars with $z < 0.3$. The quasar PSF is carefully removed using a robust spectral method

that includes iterative fitting to each spaxel of a scaled PSF, a stellar host continuum, multicomponent emission lines, and multicomponent interstellar absorption lines. This method recovers a high spatial resolution PSF and stellar, emission, and absorption line properties even at radii less than the PSF FWHM.

Outflows of ionized and/or neutral gas are revealed by the presence of broad, blueshifted absorption lines and broad, blueshifted emission lines. Kpc-scale outflows (maximum size 3–12 kpc, with the size measurement frequently limited by the instrument FOV) are found in the entire sample. By phase, 70% have ionized outflows, 80% have neutral outflows, and 50% have both. The outflows are oriented preferentially along the galaxy minor axes, and their properties are most consistent with being powered by the central AGN. The ionized outflows typically show a mix of stellar photoionization with AGN photoionization, but shocks also sometimes play a role. The quasar with the most massive and energetic outflow (PG1700+518) arises due to a kpc-scale radio jet, though the system is not formally radio-loud.

There is a wide range of typical outflow velocities. Spatially-averaged maximum velocities ($\langle v_{98\%} \rangle$) are in the range 200 – 1300 km s⁻¹, while peak velocities (max. $v_{98\%}$) are 500 – 2600 km s⁻¹. A correlation with AGN luminosity may exist in samples with a larger dynamic range of L_{AGN} , but there is no such correlation in this sample.

Outflowing masses, momenta, and energies are computed using the single-radius free wind model. These data are combined with the results of molecular gas outflow measurements, previous IFS measurements of a few Type 2 quasars, and mass outflow rates from nearby Seyferts. Quasar mass outflow rates are in the range 1 to >1000 M_⊙ yr⁻¹. The quasar “momentum boosts” range from 0.01 to 20, with half of the sample having $(c \, dp/dt)/L_{\text{AGN}} \gtrsim 1$. Energy outflow rates are primarily in the range 0.002% to 2% of L_{AGN} . When compared with properties of the star forming hosts, and with other starbursts of similar mass, the data are most consistent with the outflows being driven by the central AGN rather than star formation (except in the lowest-velocity and lowest-energy cases).

Previous studies have focused on how kpc-scale outflow properties depend on host galaxy or AGN properties. The large range of black hole masses (three orders of magnitude) covered by the current subsample and previous studies of Seyferts allows an accounting of how large-scale outflow properties depend on black hole mass, and thereby accretion rate and Eddington ratio. Significantly, the total mass and energy outflow rates summed over phases correlate at 2σ with black hole mass according to $dM/dt \sim M_{\text{BH}}^{0.7 \pm 0.3}$ and $dE/dt \sim M_{\text{BH}}^{1.3 \pm 0.5}$. They correlate similarly with σ in a way that is consistent with the $M_{\text{BH}}-\sigma$ relation.

Despite these correlations, the present data are unable to constrain or distinguish among competing quasar wind models, and cannot provide strong conclusions about quasar-mode winds as AGN feedback. It is clear that the most massive black holes do have the most massive and energetic winds. A possible relative feedback measure, the mass outflow rate normalized to the accretion rate, decreases with increasing black hole mass and Ed-

dington ratio (though the correlation significance is low). However, these tentative correlations may be affected by variations of radiative efficiency with black hole mass or variations in the accretion rate on shorter timescales than the outflow dynamical time.

This study exemplifies the importance of deep, 3D observations of large-scale outflows in quasars for gaining a complete picture of their properties. Only by studying the multiphase (warm ionized+cool neutral with optical IFS, cold molecular with mm interferometry, and other phases) structure of these winds do we gain a full accounting of the phase space (velocity+spatial geometry) and mass, momentum, and energy budget of these winds. Furthermore, it demonstrates the power of high-fidelity IFS for probing the central regions of PSF-dominated systems.

Future work can improve on this study in several ways. (1) More IFS observations of quasars. It is clear that the error bars on the correlations presented here are limited by statistics – the combined quasar+Seyfert sample in this paper numbers only 23. (2) Deep, wide-field spectroscopy to determine the wind extents. Measurements of the full extent of the winds discussed here are largely limited by the GMOS FOV. (3) Adaptive optics IFS of the unresolved PSF. This study is limited to the large-scale outflows in these systems, but the unresolved PSF contains higher-velocity outflows that couple to these large-scale outflows. IFS observations at higher spatial resolution are necessary to connect these two phenomena.

The authors thank Yuval Birnboim, Françoise Combes, Annette Ferguson, Fred Hamann, Bernd Husemann, Dusan Keres, and James Turner for helpful comments and discussion. They also thank the referee for their careful reading of the manuscript and helpful comments to improve it. D.S.N.R. thanks Lisa Kewley and the GEARS3D group at Australian National University for its hospitality while this work was completed. The authors thank the Gemini Director and User’s Committee for awarding the observing time under which some of this data was obtained.

This work was based on observations obtained at the Gemini Observatory (program IDs GN-2003B-C-5, GS-2005B-Q-50, GN-2007A-Q-12, GS-2011B-Q-64, GN-2012A-Q-15, GN2013A-Q-51, and GN-2015A-DD-9), which is operated by the Association of Universities for Research in Astronomy, Inc., under a cooperative agreement with the NSF on behalf of the Gemini partnership: the National Science Foundation (United States), the National Research Council (Canada), CONICYT (Chile), Ministério da Ciência, Tecnologia e Inovação (Brazil) and Ministerio de Ciencia, Tecnología e Innovación Productiva (Argentina).

D.S.N.R. was supported in part by the J. Lester Crain Chair of Physics at Rhodes College and by a Distinguished Visitor grant from the Research School of Astronomy & Astrophysics at Australian National University. S.V. was supported in part by NSF grant AST1009583 and NASA grant ADAP NNX16AF24G.

The *HST* observations described here were obtained from the Hubble Legacy Archive, which is a collaboration between the Space Telescope Science Institute

(STScI/NASA), the Space Telescope European Coordinating Facility (ST-ECF/ESA) and the Canadian Astronomy Data Centre (CADC/NRC/CSA).

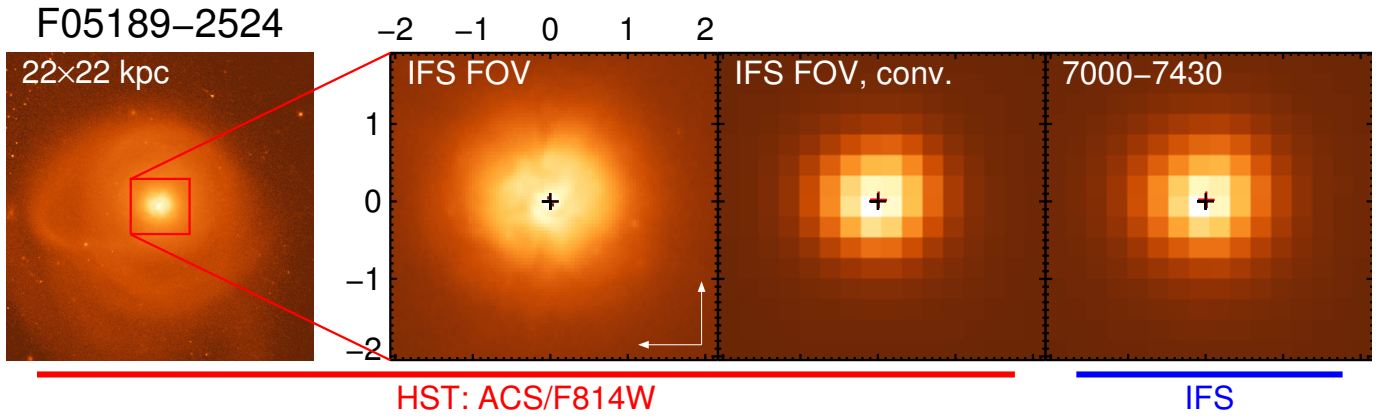
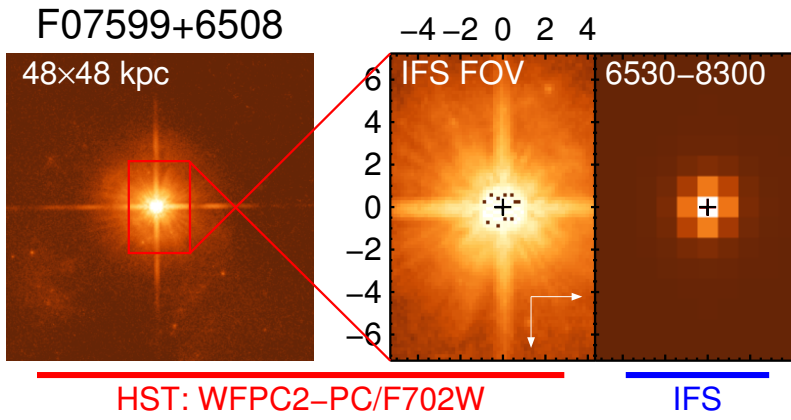
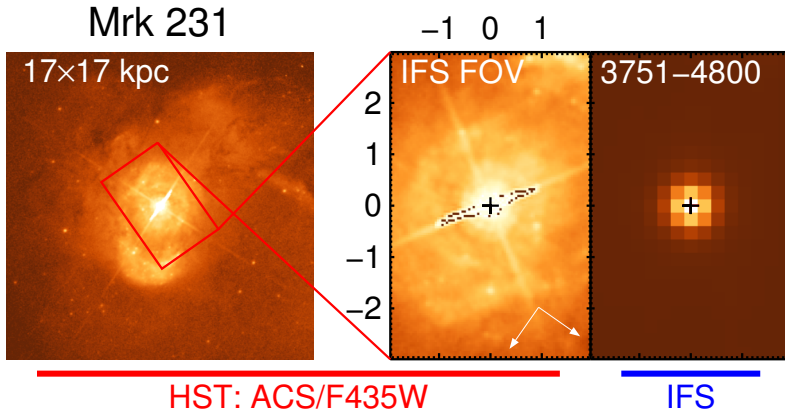
Revision 114 of the IFUDR GMOS package, based on the Gemini IRAF package, was provided by James Turner and Bryan Miller via the Gemini Data Reduction User Forum.

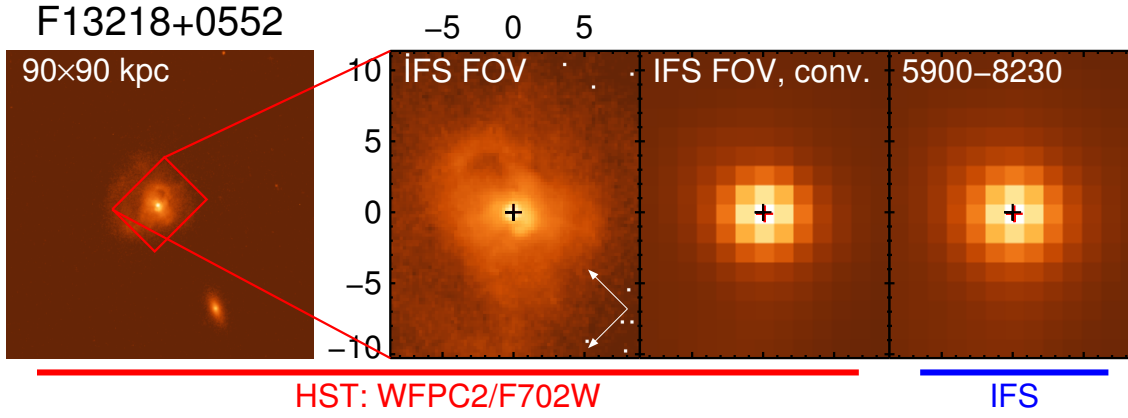
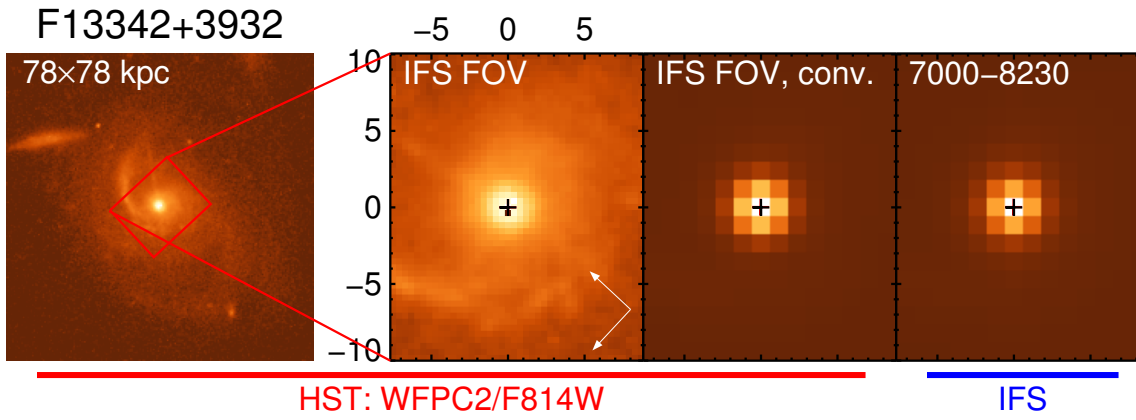
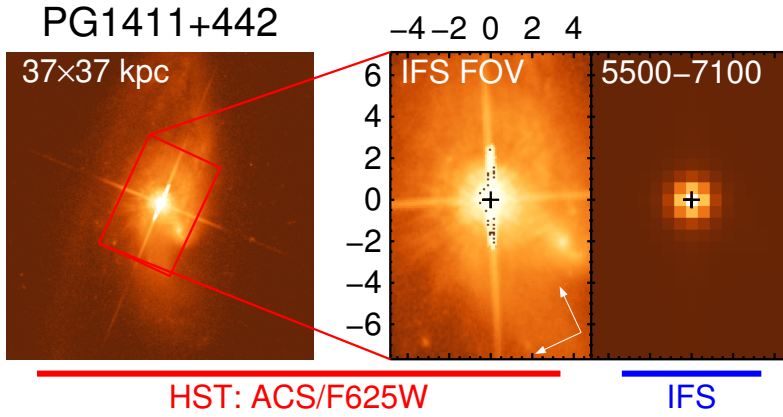
We acknowledge the usage of the HyperLeda database (<http://leda.univ-lyon1.fr>) and the AGN Black Hole Mass Database (<http://www.astro.gsu.edu/AGNmass/>; Bentz & Katz 2015).

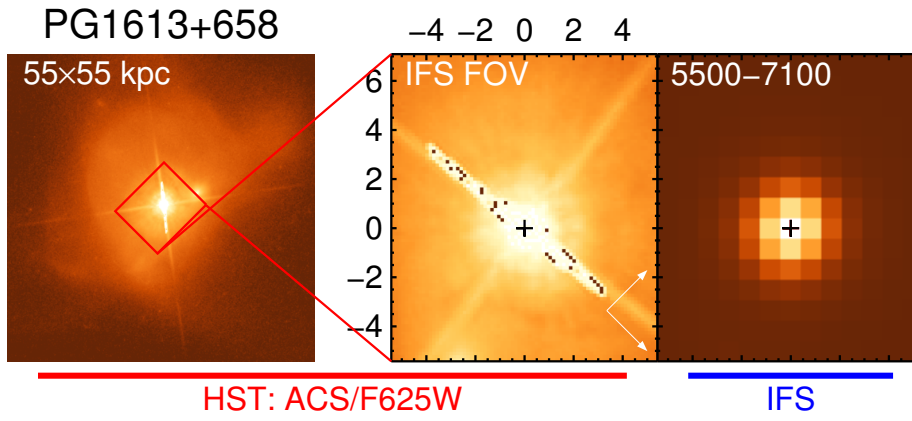
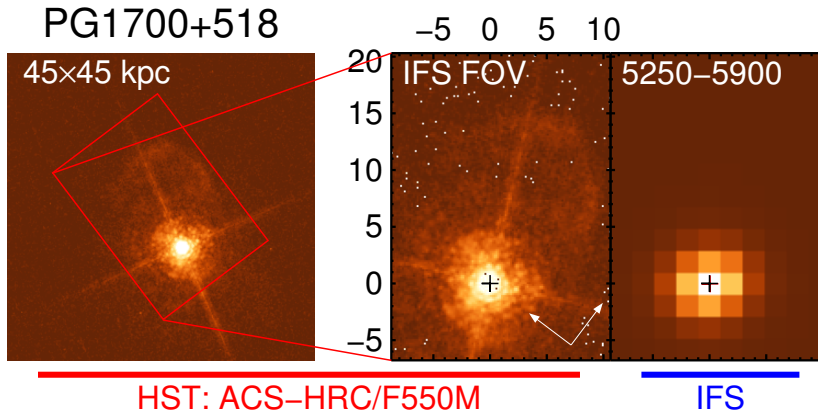
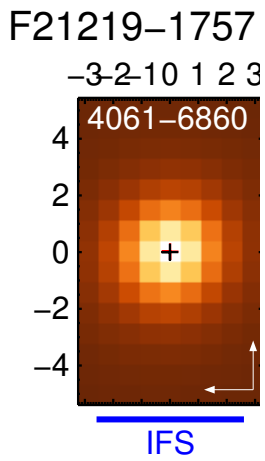
REFERENCES

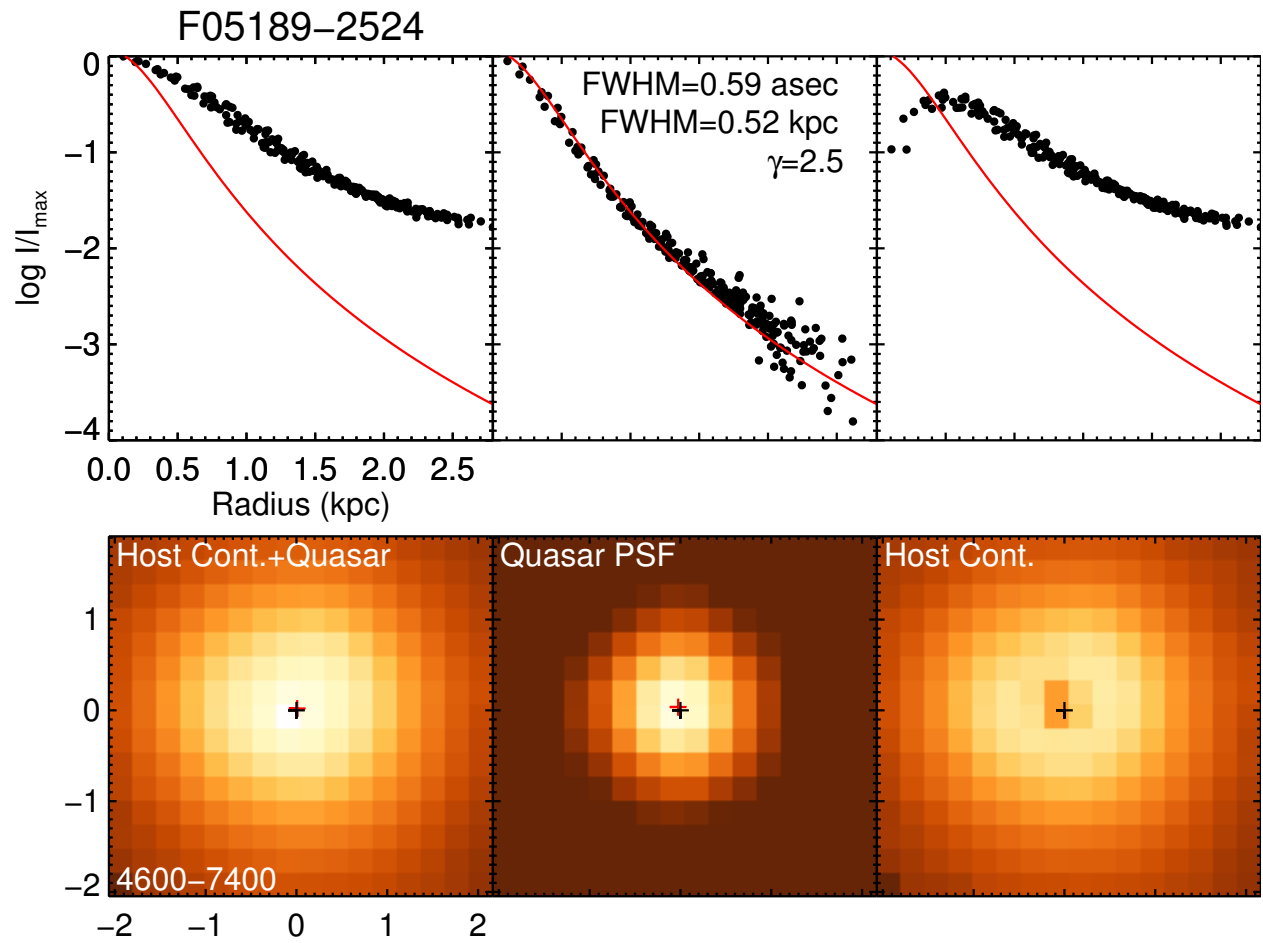
- Alatalo, K., et al. 2015, *ApJ*, 798, 31 [7]
- Allington-Smith, J., et al. 2002, *PASP*, 114, 892 [2.2]
- Anglés-Alcázar, D., Davé, R., Faucher-Giguère, C.-A., Özel, F., & Hopkins, P. F. 2017, *MNRAS*, 464, 2840 [4.3]
- Bae, H.-J., Woo, J.-H., Karouzos, M., Gallo, E., Flohic, H., Shen, Y., & Yoon, S.-J. 2017, *ApJ*, 837, 91 [1, 1, 3.1]
- Baron, D., Netzer, H., Poznanski, D., Prochaska, J. X., & Förster Schreiber, N. M. 2017, *MNRAS*, 470, 1687 [1]
- Barvainis, R., & Lonsdale, C. 1997, *AJ*, 113, 144 [1]
- Bentz, M. C., & Katz, S. 2015, *PASP*, 127, 67 [1, 5]
- Bentz, M. C., et al. 2006, *ApJ*, 651, 775 [7]
- . 2010, *ApJ*, 716, 993 [7]
- . 2013, *ApJ*, 767, 149 [7]
- Booth, C. M., & Schaye, J. 2009, *MNRAS*, 398, 53 [1]
- Boroson, T. A., & Meyers, K. A. 1992, *ApJ*, 397, 442 [2.1, 2.3.3]
- Brusa, M., et al. 2015, *MNRAS*, 446, 2394 [1]
- Cappellari, M. 2012, pPXF: Penalized Pixel-Fitting stellar kinematics extraction, Astrophysics Source Code Library, record ascl:1210.002 [2.3]
- Cappellari, M., et al. 2013, *MNRAS*, 432, 1709 [7]
- Cardelli, J. A., Clayton, G. C., & Mathis, J. S. 1989, *ApJ*, 345, 245 [2.3.2, 8, 3.2]
- Carilli, C. L., Wrobel, J. M., & Ulvestad, J. S. 1998, *AJ*, 115, 928 [1]
- Carniani, S., et al. 2015, *A&A*, 580, A102 [1]
- . 2016, *A&A*, 591, A28 [1]
- Cicone, C., et al. 2014, *A&A*, 562, A21 [1, 1, 3.3, 4.1, 4.2]
- Condon, J. J., Cotton, W. D., Greisen, E. W., Yin, Q. F., Perley, R. A., Taylor, G. B., & Broderick, J. J. 1998, *AJ*, 115, 1693 [1]
- Condon, J. J., Helou, G., & Jarrett, T. H. 2002, *AJ*, 123, 1881 [3.1]
- Condon, J. J., Helou, G., Sanders, D. B., & Soifer, B. T. 1990, *ApJS*, 73, 359 [1]
- Condon, J. J., Kellermann, K. I., Kimball, A. E., Ivezić, Ž., & Perley, R. A. 2013, *ApJ*, 768, 37 [3.1]
- Costa, T., Rosdahl, J., Sijacki, D., & Haehnelt, M. 2017, *arxiv:1703.05766* [4.2]
- Crenshaw, D. M., Fischer, T. C., Kraemer, S. B., & Schmitt, H. R. 2015, *ApJ*, 799, 83 [7]
- Dasyra, K. M., et al. 2006a, *ApJ*, 638, 745 [1]
- . 2006b, *ApJ*, 651, 835 [4.1]
- . 2007, *ApJ*, 657, 102 [1]
- Davies, R., et al. 2011, *ApJ*, 741, 69 [3.1]
- Davies, R. L., et al. 2016a, *MNRAS*, 462, 1616 [2.3.2, 3.1]
- . 2016b, *ApJ*, 824, 50 [3.1]
- Davis, S. W., & Laor, A. 2011, *ApJ*, 728, 98 [4.3]
- Davis, T. A., et al. 2012, *MNRAS*, 426, 1574 [7]
- Di Matteo, T., Springel, V., & Hernquist, L. 2005, *Nature*, 433, 604 [1]
- Dopita, M. A., & Sutherland, R. S. 1995, *ApJ*, 455, 468 [2.3.2, 3.1]
- Dopita, M. A., et al. 2006, *ApJS*, 167, 177 [2.3.2]
- Dubois, Y., Peirani, S., Pichon, C., Devriendt, J., Gavazzi, R., Welker, C., & Volonteri, M. 2016, *MNRAS*, 463, 3948 [1]
- Farrah, D., Surace, J. A., Veilleux, S., Sanders, D. B., & Vacca, W. D. 2005, *ApJ*, 626, 70 [2.3.1]
- Farrah, D., et al. 2012, *ApJ*, 745, 178 [1]
- Faucher-Giguère, C.-A., Quataert, E., & Murray, N. 2012, *MNRAS*, 420, 1347 [18, 4.2]
- Feruglio, C., Maiolino, R., Piconcelli, E., Menci, N., Aussel, H., Lamastra, A., & Fiore, F. 2010, *A&A*, 518, L155 [1, 4.1]
- Feruglio, C., et al. 2015, *A&A*, 583, A99 [1, 4.1]
- Fiore, F., et al. 2017, *A&A*, 601, A143 [1, 3.3, 4.1]
- Fischer, J., et al. 2010, *A&A*, 518, L41 [1, 4.1]
- Fischer, T. C., Crenshaw, D. M., Kraemer, S. B., & Schmitt, H. R. 2013, *ApJS*, 209, 1 [3.1, 3.2]
- García-Burillo, S., et al. 2014, *A&A*, 567, A125 [7]
- Gaspari, M., & Sądowski, A. 2017, *ApJ*, 837, 149 [4.2]
- González-Alfonso, E., et al. 2017, *ApJ*, 836, 11 [1, 1, 5, 6, 3.2, 4.1, 4.1, 8, 4.2]
- González Delgado, R. M., Cerviño, M., Martins, L. P., Leitherer, C., & Hauschildt, P. H. 2005, *MNRAS*, 357, 945 [4, 2.3.1]
- Greenhill, L. J., et al. 2003, *ApJ*, 590, 162 [7]
- Grier, C. J., et al. 2013, *ApJ*, 773, 90 [1]
- Groves, B. A., Dopita, M. A., & Sutherland, R. S. 2004, *ApJS*, 153, 75 [2.3.2]
- Gültekin, K., et al. 2009, *ApJ*, 698, 198 [7, 3.3, 17]
- Gurvich, A., Burkhart, B., & Bird, S. 2017, *ApJ*, 835, 175 [1]
- Harrison, C. M., Alexander, D. M., Mullaney, J. R., & Swinbank, A. M. 2014, *MNRAS*, 441, 3306 [1, 1, 3.1, 3.3, 4.1]
- Heckman, T. M., Alexandroff, R. M., Borthakur, S., Overzier, R., & Leitherer, C. 2015, *ApJ*, 809, 147 [4.1, 8]
- Ho, I.-T., et al. 2016, *MNRAS*, 457, 1257 [3.1]
- Hook, I. M., Jørgensen, I., Allington-Smith, J. R., Davies, R. L., Metcalfe, N., Murowinski, R. G., & Crampton, D. 2004, *PASP*, 116, 425 [2.2]
- Hopkins, P. F., & Elvis, M. 2010, *MNRAS*, 401, 7 [4.2, 19]
- Hopkins, P. F., Torrey, P., Faucher-Giguère, C.-A., Quataert, E., & Murray, N. 2016, *MNRAS*, 458, 816 [1, 4.2, 4.2, 19, 4.3]
- Husemann, B., Jahnke, K., Sánchez, S. F., Wisotzki, L., Nugroho, D., Kupko, D., & Schramm, M. 2014, *MNRAS*, 443, 755 [1]
- Husemann, B., Scharwächter, J., Bennert, V. N., Mainieri, V., Woo, J.-H., & Kakkad, D. 2016, *A&A*, 594, A44 [1]
- Husemann, B., Wisotzki, L., Sánchez, S. F., & Jahnke, K. 2013, *A&A*, 549, A43 [1, 3.1]
- Ishibashi, W., & Fabian, A. C. 2015, *MNRAS*, 451, 93 [4.2]
- Kauffmann, G., et al. 2003, *MNRAS*, 346, 1055 [10]
- Kaviraj, S., et al. 2017, *MNRAS*, 467, 4739 [1]
- Kelly, B. C. 2007, *ApJ*, 665, 1489 [14, 3.3]
- Kewley, L. J., Dopita, M. A., Sutherland, R. S., Heisler, C. A., & Trevena, J. 2001, *ApJ*, 556, 121 [10, 3.1]
- Kewley, L. J., Groves, B., Kauffmann, G., & Heckman, T. 2006, *MNRAS*, 372, 961 [2.3.2, 10]
- Kim, D.-C., & Sanders, D. B. 1998, *ApJS*, 119, 41 [2.1]
- Kim, D.-C., et al. 2013, *ApJ*, 768, 102 [2.3.1]
- King, A. 2003, *ApJL*, 596, L27 [1]
- King, A., & Nixon, C. 2015, *MNRAS*, 453, L46 [4.3]
- King, A. R., Zubovas, K., & Power, C. 2011, *MNRAS*, 415, L6 [4.2]
- Kukula, M. J., Dunlop, J. S., Hughes, D. H., & Rawlings, S. 1998, *MNRAS*, 297, 366 [1, 3.1]
- Kuo, C. Y., et al. 2011, *ApJ*, 727, 20 [7]
- Lehnert, M. D., & Heckman, T. M. 1996, *ApJ*, 462, 651 [3.1]
- Leitherer, C., et al. 1999, *ApJS*, 123, 3 [4.1, 8]
- Leung, G. C. K., et al. 2017, *ArXiv e-prints* [1]
- Liu, G., Zakamska, N. L., & Greene, J. E. 2014, *MNRAS*, 442, 1303 [1]
- Liu, G., Zakamska, N. L., Greene, J. E., Nesvadba, N. P. H., & Liu, X. 2013a, *MNRAS*, 430, 2327 [1]
- . 2013b, *MNRAS*, 436, 2576 [1]
- Liu, X., Zakamska, N. L., Greene, J. E., Strauss, M. A., Krolik, J. H., & Heckman, T. M. 2009, *ApJ*, 702, 1098 [7]
- Lodato, G., & Bertin, G. 2003, *A&A*, 398, 517 [7]
- Lupton, R. H., Gunn, J. E., & Szalay, A. S. 1999, *AJ*, 118, 1406 [1]
- Makarov, D., Prugniel, P., Terekhova, N., Courtois, H., & Vauglin, I. 2014, *A&A*, 570, A13 [7]
- Marconi, A., & Hunt, L. K. 2003, *ApJL*, 589, L21 [1]
- Markwardt, C. 2012, MPFIT: Robust non-linear least squares curve fitting, Astrophysics Source Code Library, record ascl:1208.019 [2.3]
- McElroy, R., Croom, S. M., Pracy, M., Sharp, R., Ho, I.-T., & Medling, A. M. 2015, *MNRAS*, 446, 2186 [1, 1, 3.1, 3.3]
- Moorwood, A. F. M., Lutz, D., Oliva, E., Marconi, A., Netzer, H., Genzel, R., Sturm, E., & de Graauw, T. 1996, *A&A*, 315, L109 [7]
- Morganti, R., Veilleux, S., Oosterloo, T., Teng, S. H., & Rupke, D. 2016, *A&A*, 593, A30 [1, 3.1, 4.1]
- Moster, B. P., Naab, T., & White, S. D. M. 2013, *MNRAS*, 428, 3121 [2.1]
- Müller-Sánchez, F., Prieto, M. A., Hicks, E. K. S., Vives-Arias, H., Davies, R. I., Malkan, M., Tacconi, L. J., & Genzel, R. 2011, *ApJ*, 739, 69 [7]
- Netzer, H., et al. 2007, *ApJ*, 666, 806 [2.1]
- Osterbrock, D. E., & Martel, A. 1993, *ApJ*, 414, 552 [7]

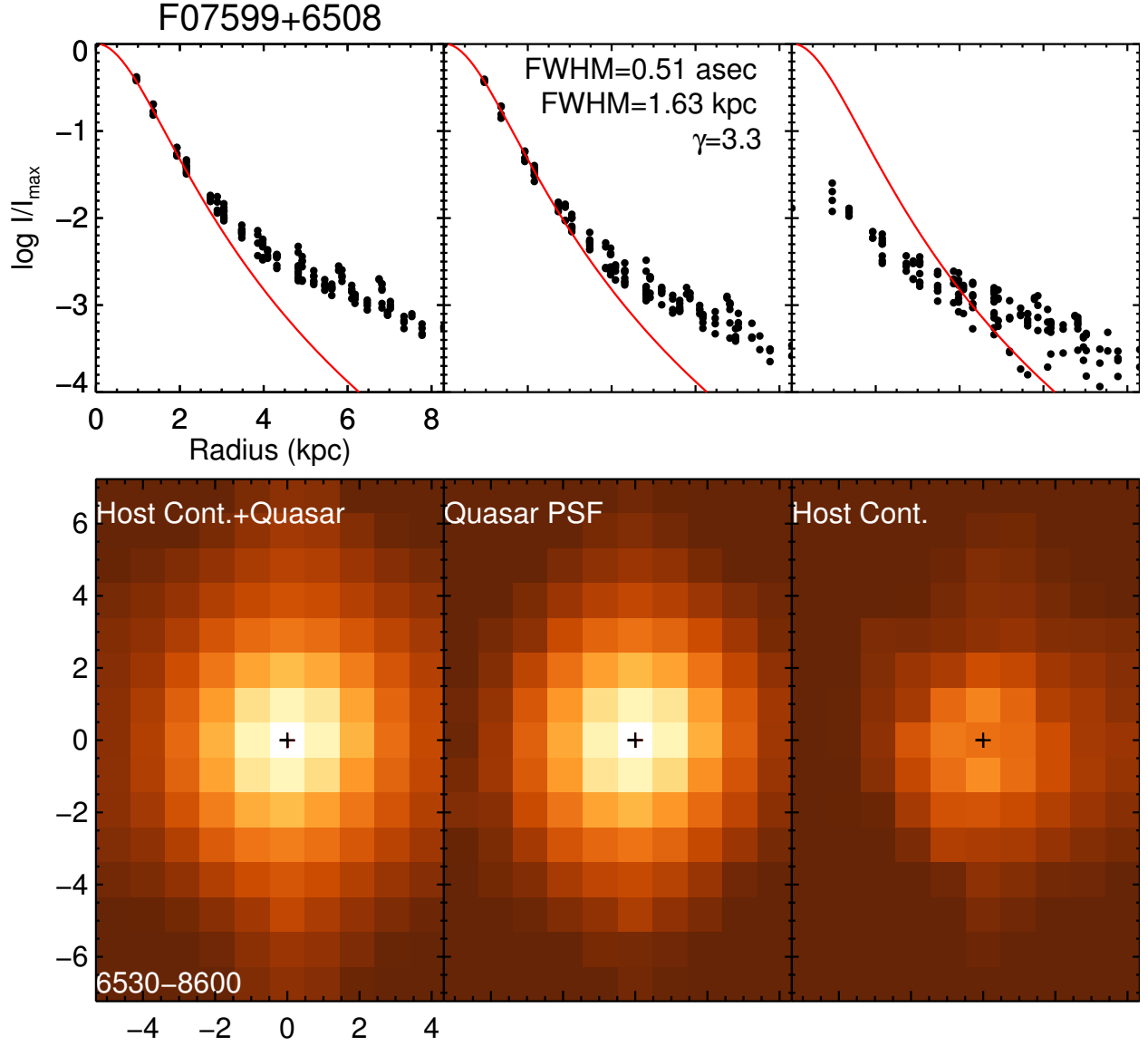
- Ott, T. 2012, QFitsView: FITS file viewer, Astrophysics Source Code Library, record ascl:1210.019 [2.2]
- Perna, M., et al. 2015, *A&A*, 574, A82 [1]
- Peterson, B. M., et al. 2004, *ApJ*, 613, 682 [7]
- Pontzen, A., Tremmel, M., Roth, N., Peiris, H. V., Saintonge, A., Volonteri, M., Quinn, T., & Governato, F. 2017, *MNRAS*, 465, 547 [1]
- Reynolds, C. S. 2013, *Classical and Quantum Gravity*, 30, 244004 [4.3]
- Rich, J. A., Kewley, L. J., & Dopita, M. A. 2011, *ApJ*, 734, 87 [2.3.2, 3.1]
- Richardson, M. L. A., Scannapieco, E., Devriendt, J., Slyz, A., Thacker, R. J., Dubois, Y., Wurster, J., & Silk, J. 2016, *ApJ*, 825, 83 [1]
- Riffel, R. A., Storch-Bergmann, T., Dors, O. L., & Winge, C. 2009, *MNRAS*, 393, 783 [7]
- Riffel, R. A., Storch-Bergmann, T., & Winge, C. 2013, *MNRAS*, 430, 2249 [7]
- Rivers, E., et al. 2015, *ApJ*, 815, 55 [7]
- Rothberg, B., Fischer, J., Rodrigues, M., & Sanders, D. B. 2013, *ApJ*, 767, 72 [1]
- Runnoe, J. C., Brotherton, M. S., & Shang, Z. 2012, *MNRAS*, 422, 478 [7]
- Rupke, D. S., Veilleux, S., & Sanders, D. B. 2005a, *ApJ*, 632, 751 [2.1, 2.3.3]
- . 2005b, *ApJS*, 160, 87 [2.3.3, 5, 3.2]
- . 2005c, *ApJS*, 160, 115 [3.2, 5, 3.2, 15, 4.1, 4.1]
- Rupke, D. S. N. 2014a, IFSFIT: Spectral Fitting for Integral Field Spectrographs, Astrophysics Source Code Library, record ascl:1409.005 [2.2]
- . 2014b, IFSRED: Data Reduction for Integral Field Spectrographs, Astrophysics Source Code Library, record ascl:1409.004 [2.3]
- Rupke, D. S. N., & Veilleux, S. 2011, *ApJL*, 729, L27 [1, 2.3.2, 2.3.3, 4.1]
- . 2013a, *ApJL*, 775, L15 [1, 2.3.2]
- . 2013b, *ApJ*, 768, 75 [1, 1, 2.2, 2.3.2, 3.1, 3.2, 5, 3.3, 14, 4.1, 17, 4.2]
- . 2015, *ApJ*, 801, 126 [2.2, 2.3.3, 3.1]
- Rupke, D. S. N., Veilleux, S., & Baker, A. J. 2008, *ApJ*, 674, 172 [4, 3.2, 17]
- Sanders, R. L., et al. 2016, *ApJ*, 816, 23 [2.3.2, 9]
- Scharwächter, J., Dopita, M. A., Zuther, J., Fischer, S., Komossa, S., & Eckart, A. 2011, *AJ*, 142, 43 [3.1]
- Schawinski, K., Koss, M., Berney, S., & Sartori, L. F. 2015, *MNRAS*, 451, 2517 [4.3]
- Schaye, J., et al. 2015, *MNRAS*, 446, 521 [1]
- Schmidt, M., & Green, R. F. 1983, *ApJ*, 269, 352 [2.1]
- Schmitt, H. R., Donley, J. L., Antonucci, R. R. J., Hutchings, J. B., Kinney, A. L., & Pringle, J. E. 2003, *ApJ*, 597, 768 [7]
- Schönnell, A. J., Riffel, R. A., Storch-Bergmann, T., & Winge, C. 2014, *MNRAS*, 445, 414 [7]
- Schönnell, Jr., A. J., Storch-Bergmann, T., Riffel, R. A., & Riffel, R. 2017, *MNRAS*, 464, 1771 [7]
- Schweitzer, M., et al. 2006, *ApJ*, 649, 79 [2.1]
- Shakura, N. I., & Sunyaev, R. A. 1973, *A&A*, 24, 337 [4.3]
- Sharp, R. G., & Bland-Hawthorn, J. 2010, *ApJ*, 711, 818 [3.1]
- Shih, H., & Rupke, D. S. N. 2010, *ApJ*, 724, 1430 [3.2, 5]
- Silk, J., & Rees, M. J. 1998, *A&A*, 331, L1 [1]
- Smith, P. S., Schmidt, G. D., Allen, R. G., & Angel, J. R. P. 1995, *ApJ*, 444, 146 [2.1]
- Somerville, R. S., Hopkins, P. F., Cox, T. J., Robertson, B. E., & Hernquist, L. 2008, *MNRAS*, 391, 481 [1, 2.1]
- Spoon, H. W. W., et al. 2013, *ApJ*, 775, 127 [1, 3.3, 4.1, 4.2]
- Stone, M., Veilleux, S., Meléndez, M., Sturm, E., Graciá-Carpio, J., & González-Alfonso, E. 2016, *ApJ*, 826, 111 [1, 3.3, 4.1, 4.2]
- Sturm, E., et al. 2011, *ApJL*, 733, L16 [1, 3.3, 4.1, 4.2]
- Sun, A.-L., Greene, J. E., & Zakamska, N. L. 2017, *ApJ*, 835, 222 [1, 3.3, 4.1]
- Taylor, P., & Kobayashi, C. 2015, *MNRAS*, 448, 1835 [1]
- Thompson, K. L. 1991, *ApJ*, 374, 496 [2.3.3]
- Thompson, T. A., Fabian, A. C., Quataert, E., & Murray, N. 2015, *MNRAS*, 449, 147 [4.2]
- Tombesi, F., Meléndez, M., Veilleux, S., Reeves, J. N., González-Alfonso, E., & Reynolds, C. S. 2015, *Nature*, 519, 436 [18]
- Turnshek, D. A., Monier, E. M., Sirola, C. J., & Espey, B. R. 1997, *ApJ*, 476, 40 [2.1]
- Veilleux, S., Bland-Hawthorn, J., Cecil, G., Tully, R. B., & Miller, S. T. 1999a, *ApJ*, 520, 111 [7]
- Veilleux, S., Cecil, G., & Bland-Hawthorn, J. 2005, *ARA&A*, 43, 769 [8]
- Veilleux, S., Cecil, G., Bland-Hawthorn, J., Tully, R. B., Filippenko, A. V., & Sargent, W. L. W. 1994, *ApJ*, 433, 48 [3.2]
- Veilleux, S., Kim, D.-C., & Sanders, D. B. 2002, *ApJS*, 143, 315 [2.3.1]
- Veilleux, S., Meléndez, M., Tripp, T. M., Hamann, F., & Rupke, D. S. N. 2016, *ApJ*, 825, 42 [2.1, 2.3.3]
- Veilleux, S., & Osterbrock, D. E. 1987, *ApJS*, 63, 295 [2.3.2]
- Veilleux, S., & Rupke, D. S. 2002, *ApJL*, 565, L63 [3.1]
- Veilleux, S., Sanders, D. B., & Kim, D.-C. 1999b, *ApJ*, 522, 139 [2.1, 2.3.1]
- Veilleux, S., et al. 2006, *ApJ*, 643, 707 [2.1, 2.1, 2.3.1]
- . 2009a, *ApJ*, 701, 587 [1, 2.1, 2.3.1]
- . 2009b, *ApJS*, 182, 628 [1, 2.1, 2.1, 4.1]
- . 2013a, *ApJ*, 776, 27 [1, 1, 3.3, 4.1, 4.2]
- . 2013b, *ApJ*, 764, 15 [2.3.3]
- Véron-Cetty, M.-P., & Véron, P. 2006, *A&A*, 455, 773 [7]
- Volonteri, M., Dubois, Y., Pichon, C., & Devriendt, J. 2016, *MNRAS*, 460, 2979 [1]
- Wagner, A. Y., Umemura, M., & Bicknell, G. V. 2013, *ApJL*, 763, L18 [4.2]
- Ward, M., Penston, M. V., Blades, J. C., & Turtle, A. J. 1980, *MNRAS*, 193, 563 [7]
- Westmoquette, M. S., Clements, D. L., Bendo, G. J., & Khan, S. A. 2012, *MNRAS*, 3173 [1]
- Wold, M., Lacy, M., Käufl, H. U., & Siebenmorgen, R. 2006, *A&A*, 460, 449 [7]
- Woo, J.-H., et al. 2010, *ApJ*, 716, 269 [1, 7]
- Wylezalek, D., & Zakamska, N. L. 2016, *MNRAS*, 461, 3724 [1, 1]
- Wylezalek, D., et al. 2017, *MNRAS* [1]
- Yang, J., Wu, F., Paragi, Z., & An, T. 2012, *MNRAS*, 419, L74 [3.1]
- Yesuf, H. M., et al. 2017, *ApJ*, 841, 83 [1]
- Zschaechner, L. K., et al. 2016, *ApJ*, 832, 142 [7]
- Zubovas, K., & King, A. 2012, *ApJL*, 745, L34 [1, 14, 17, 4.2, 4.2, 19]

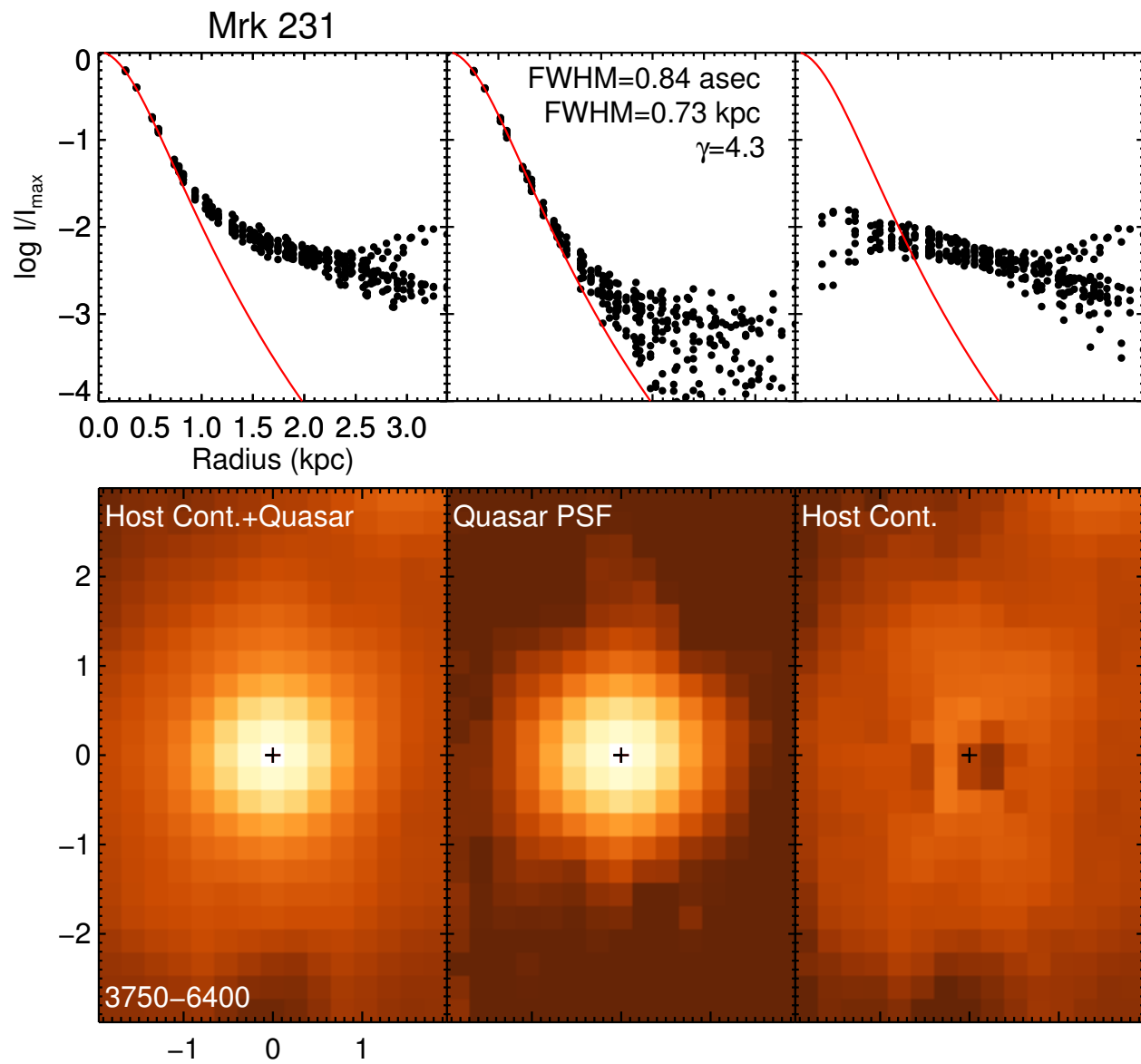
Figure 1. *Continued.*Figure 1. *Continued.*Figure 1. *Continued.*

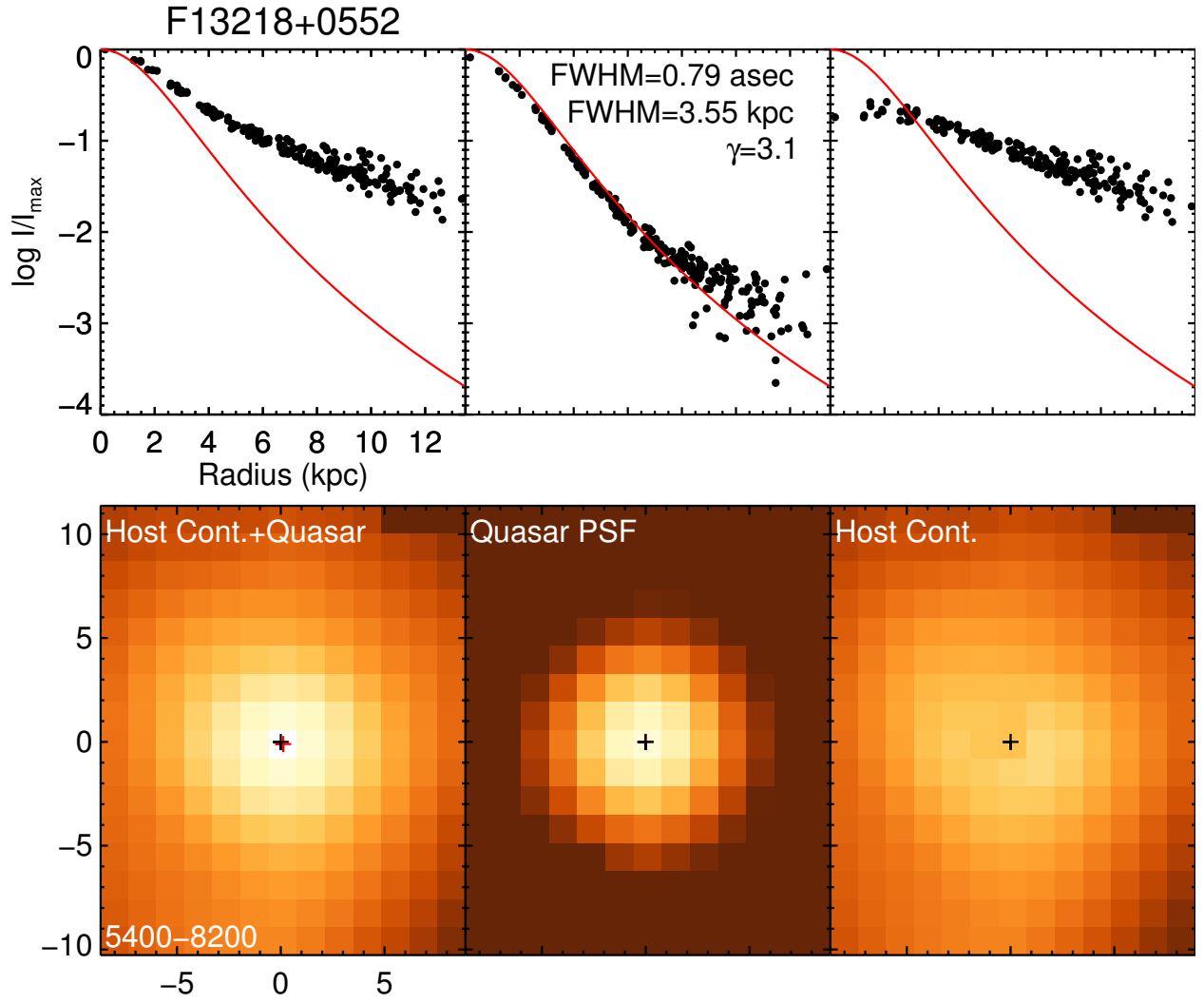

 Figure 1. *Continued.*

 Figure 1. *Continued.*

 Figure 1. *Continued.*

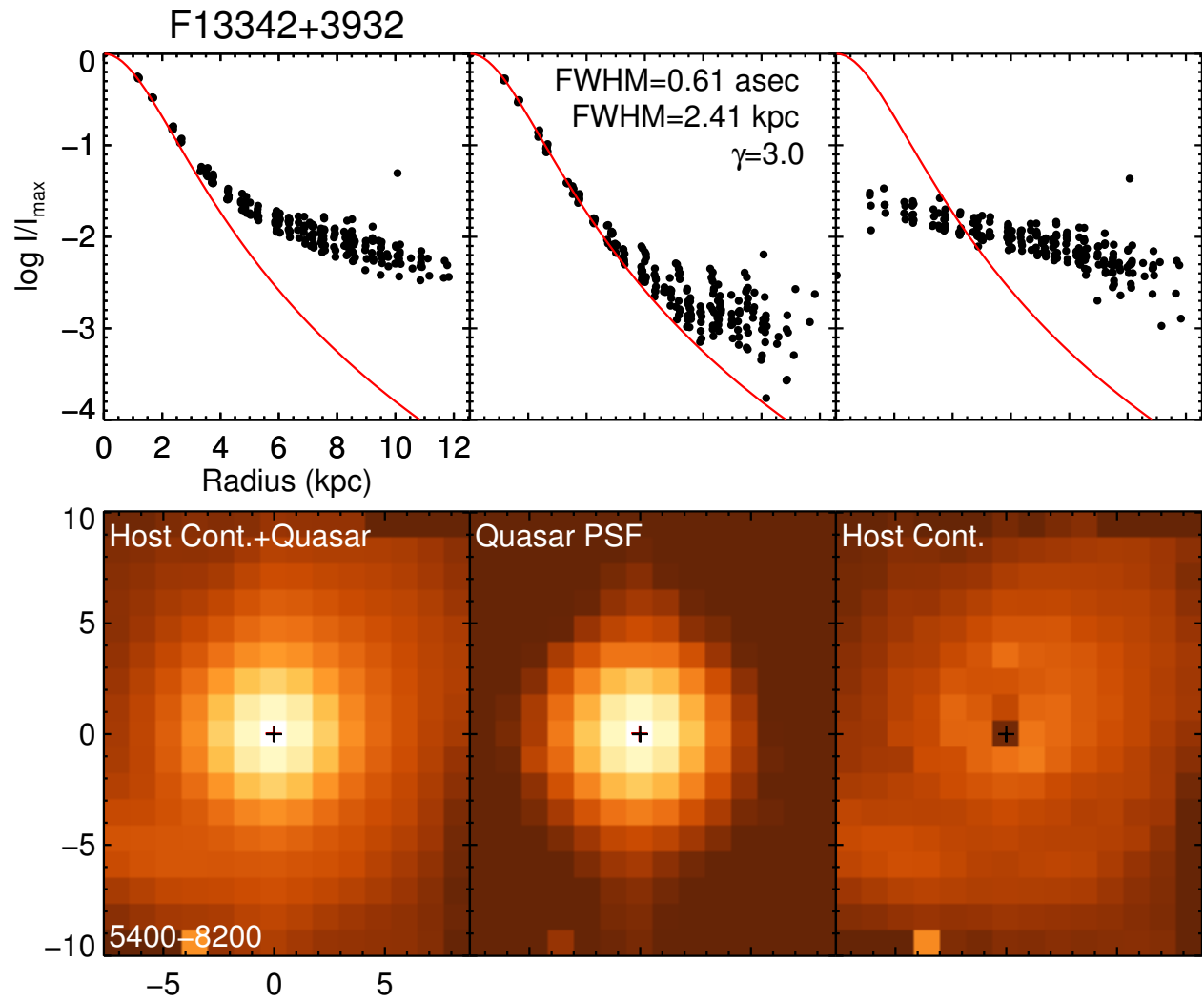
Figure 1. *Continued.*Figure 1. *Continued.*Figure 1. *Continued.*

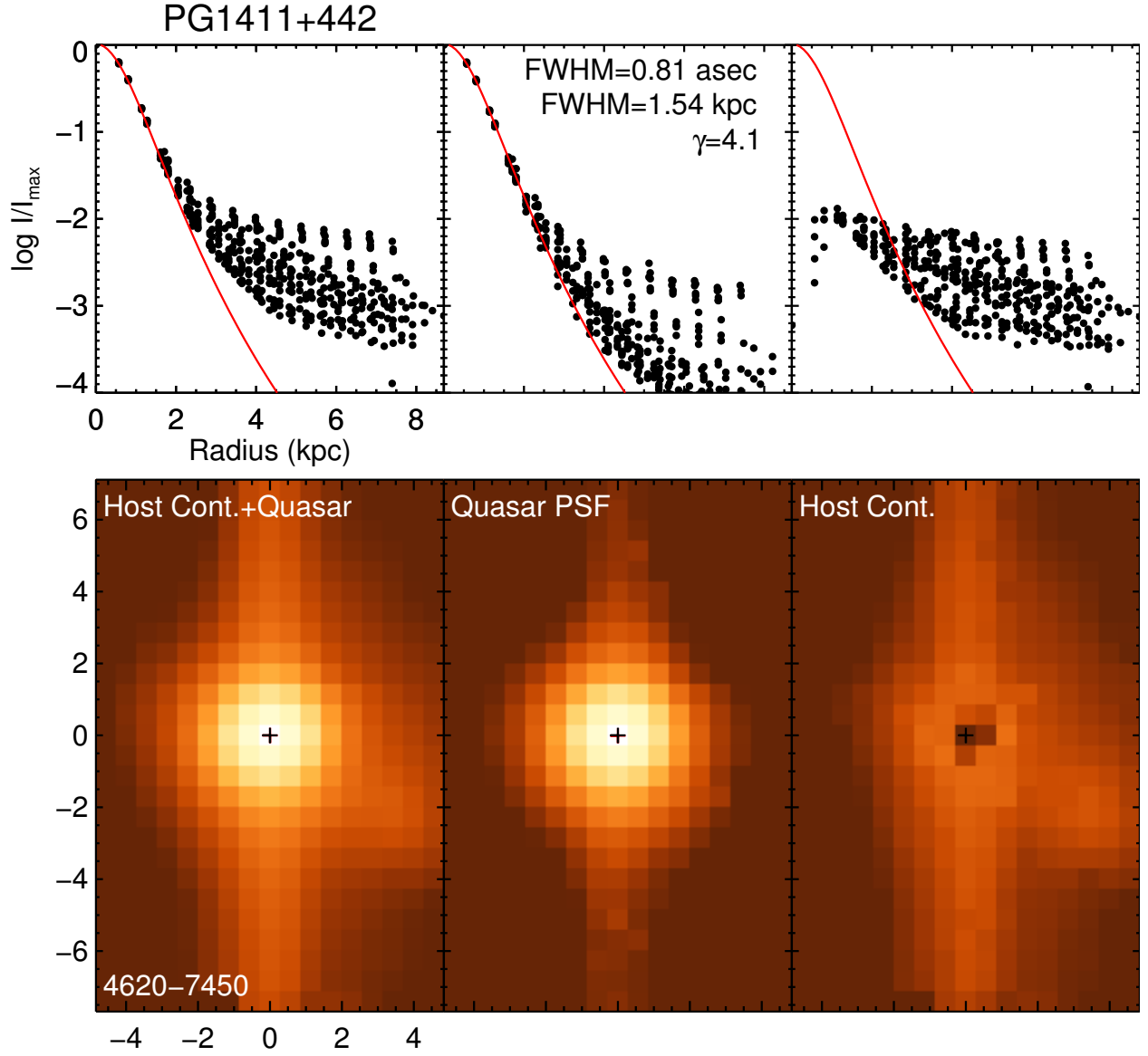
Figure 5. *Continued.*

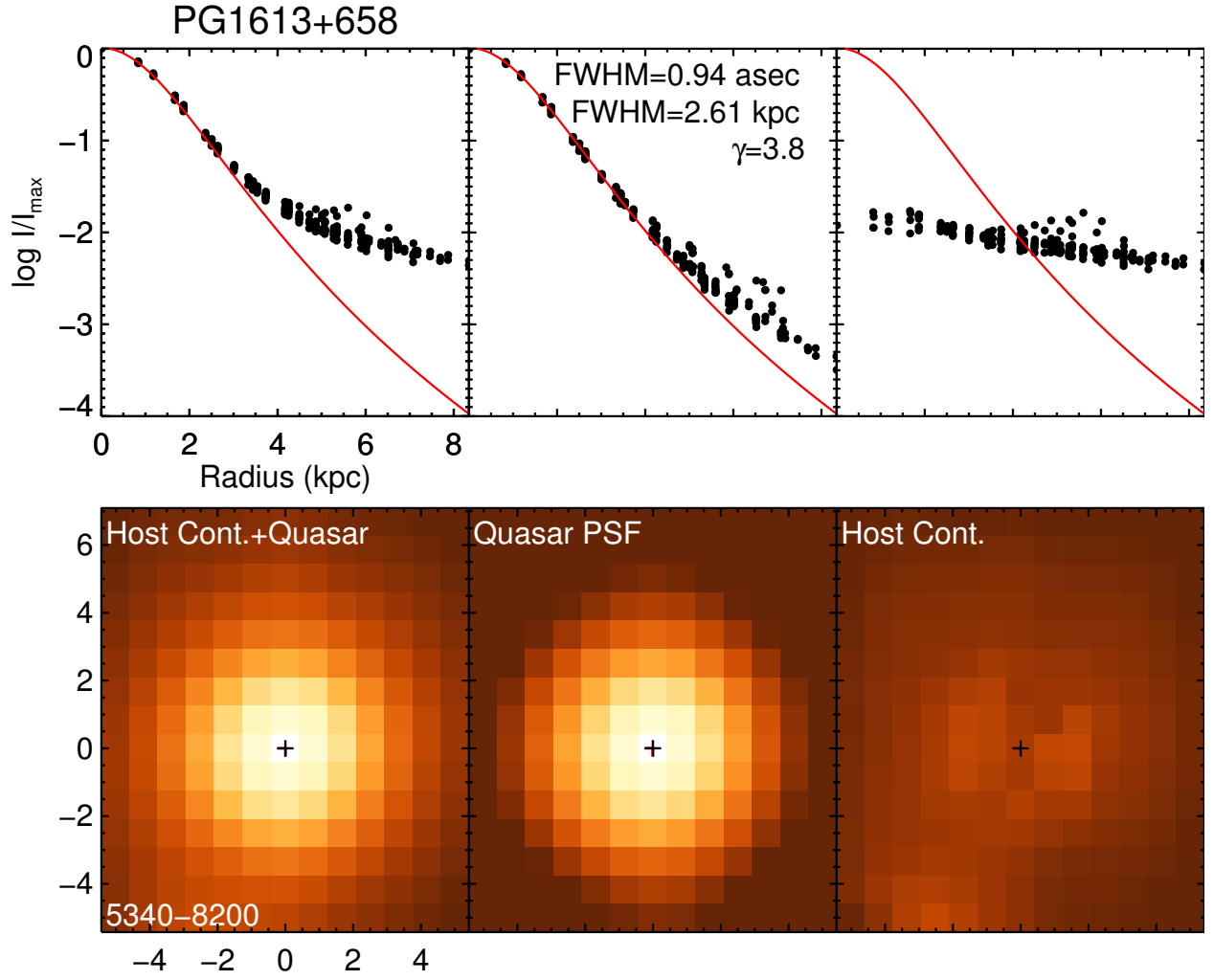

 Figure 5. *Continued.*

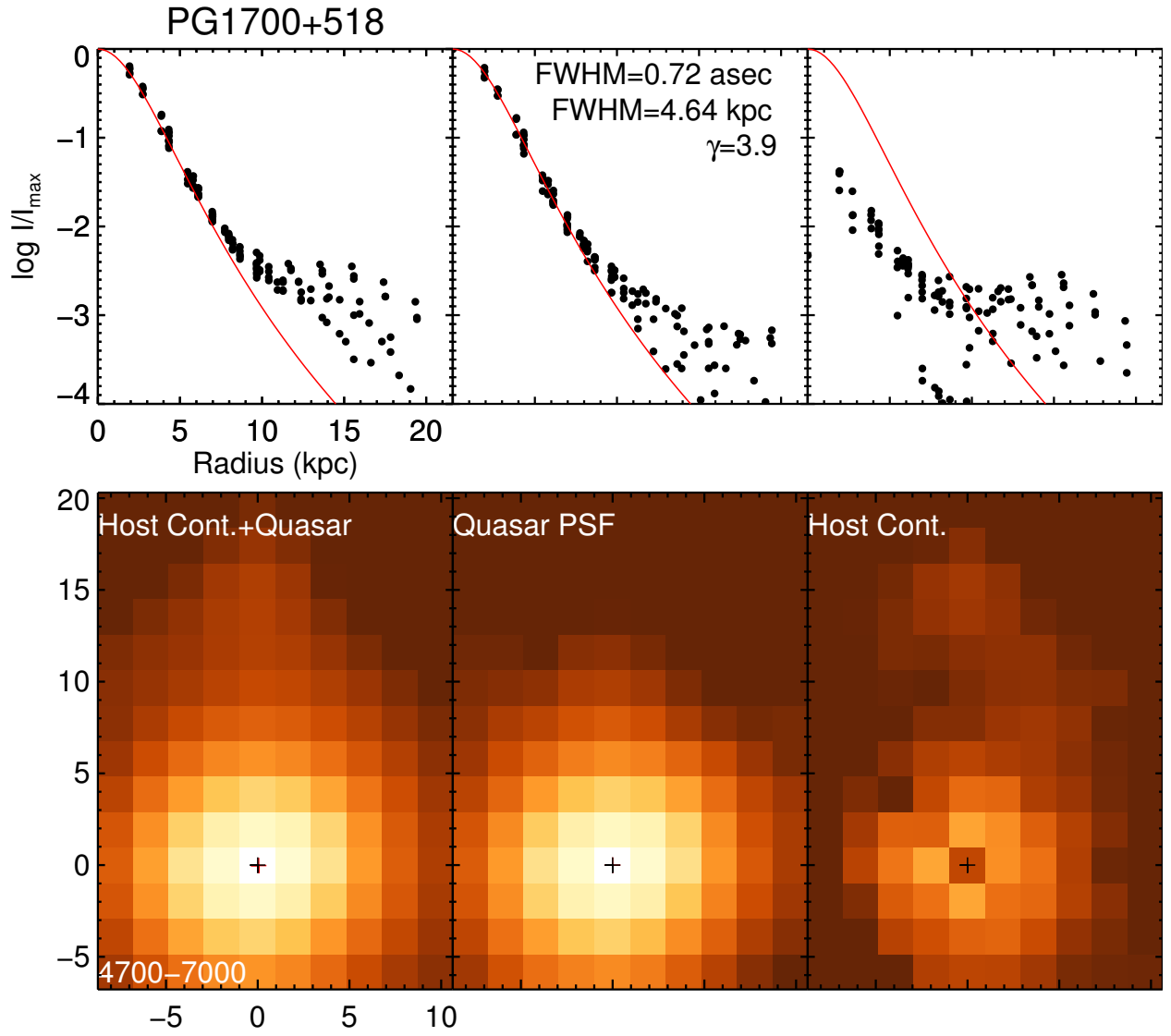
Figure 5. *Continued.*

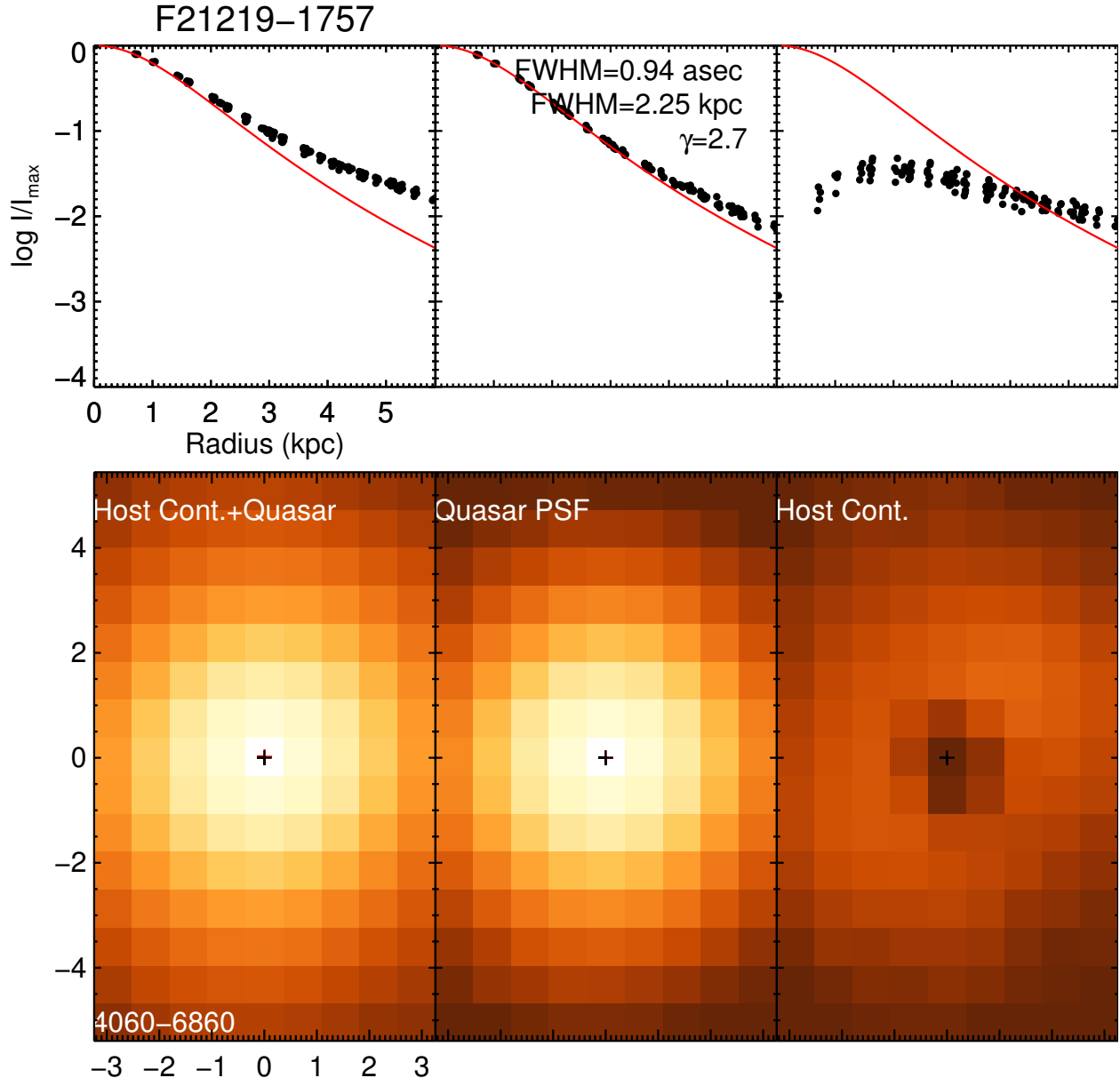

 Figure 5. *Continued.*

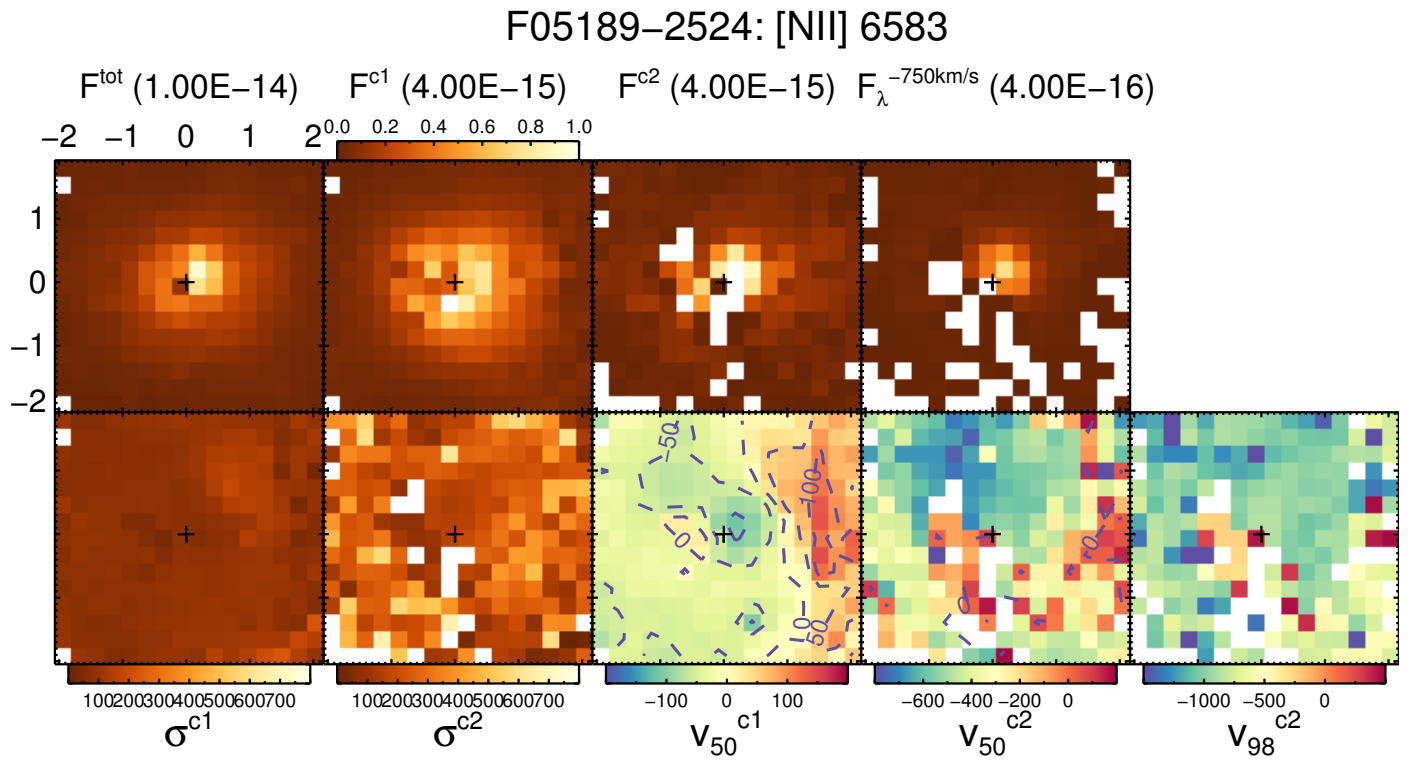
Figure 5. *Continued.*

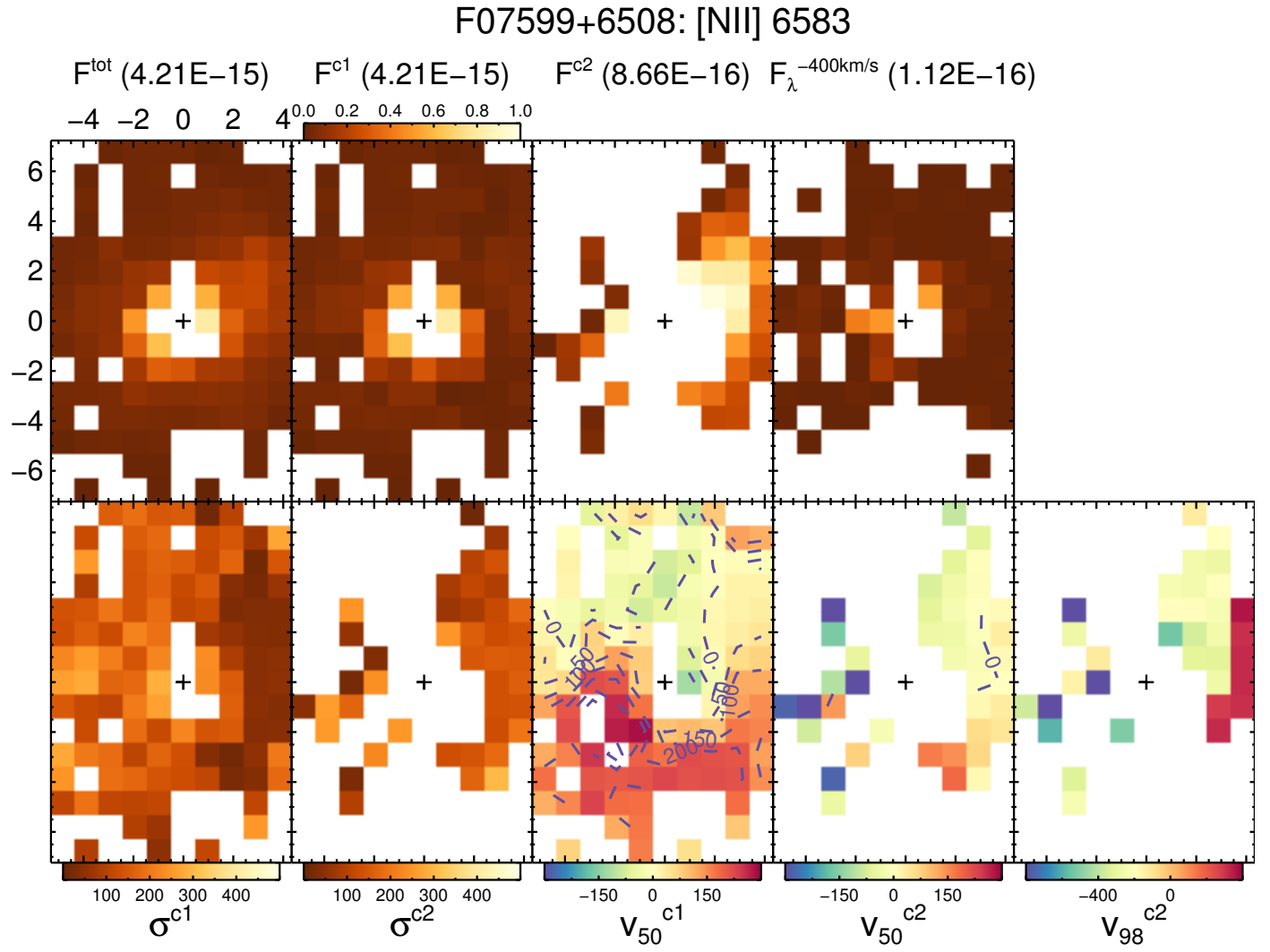

 Figure 5. *Continued.*

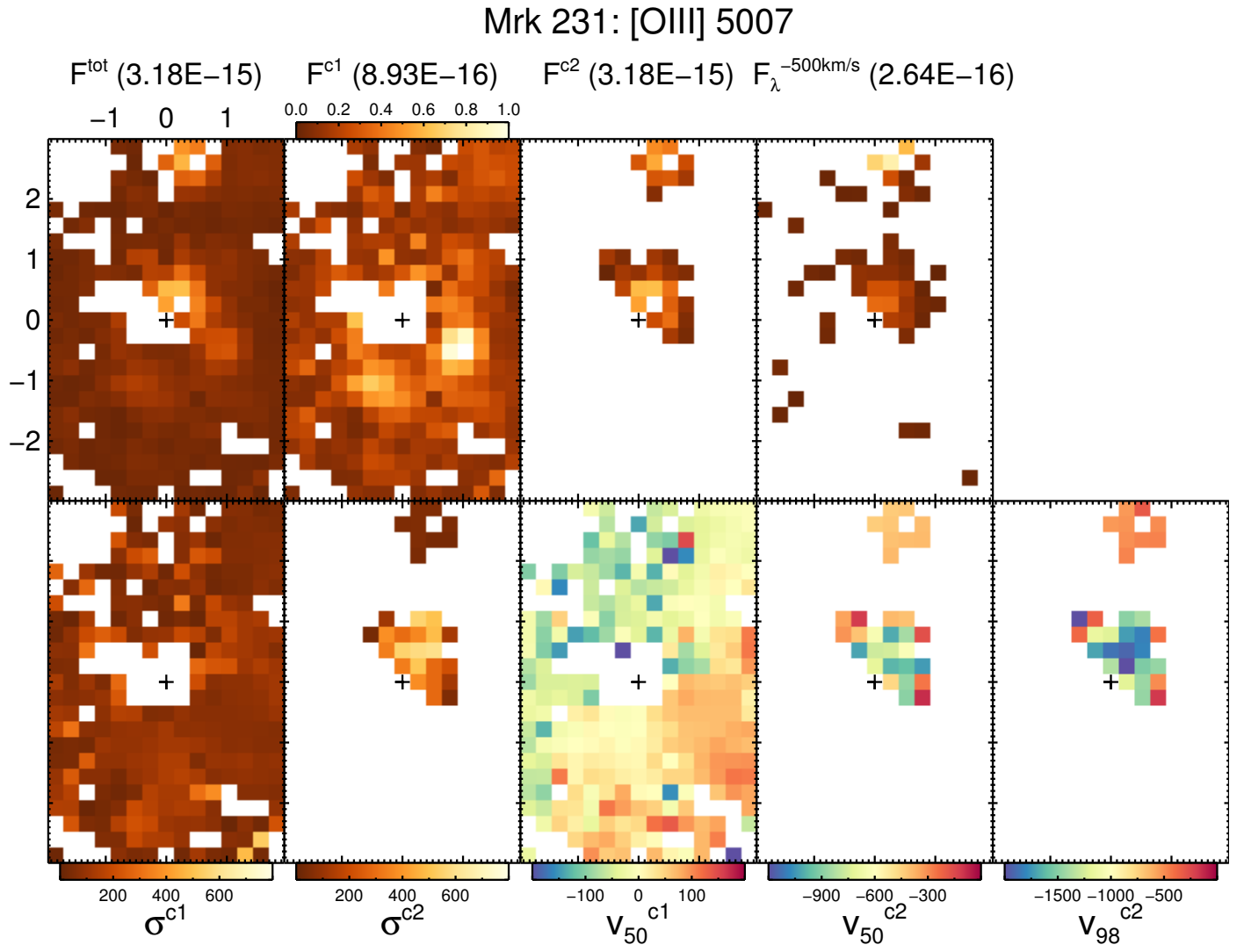
Figure 5. *Continued.*


 Figure 5. *Continued.*

Figure 5. *Continued.*


 Figure 7. *Continued.*

Figure 7. *Continued.*


 Figure 7. *Continued.*

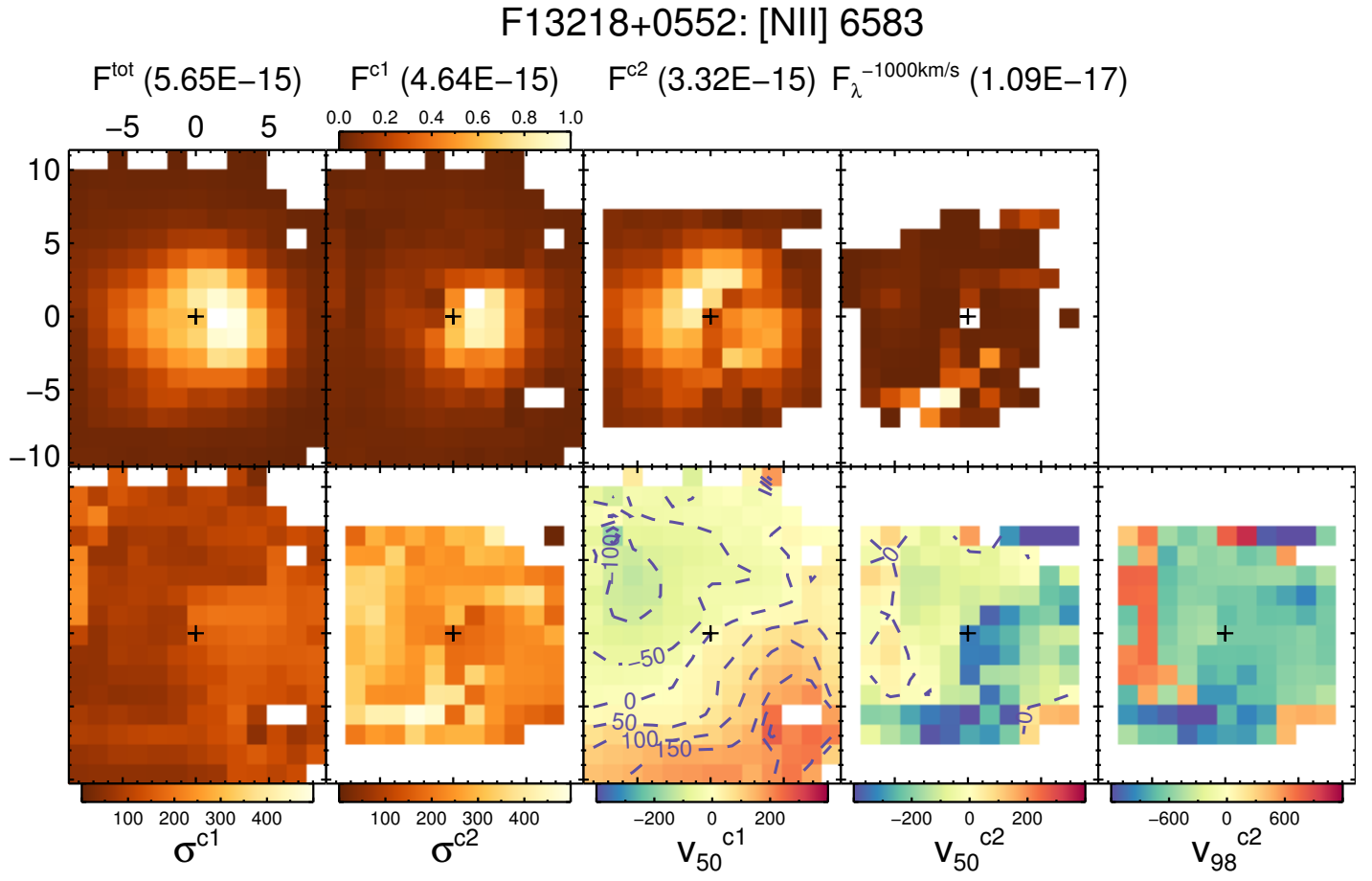
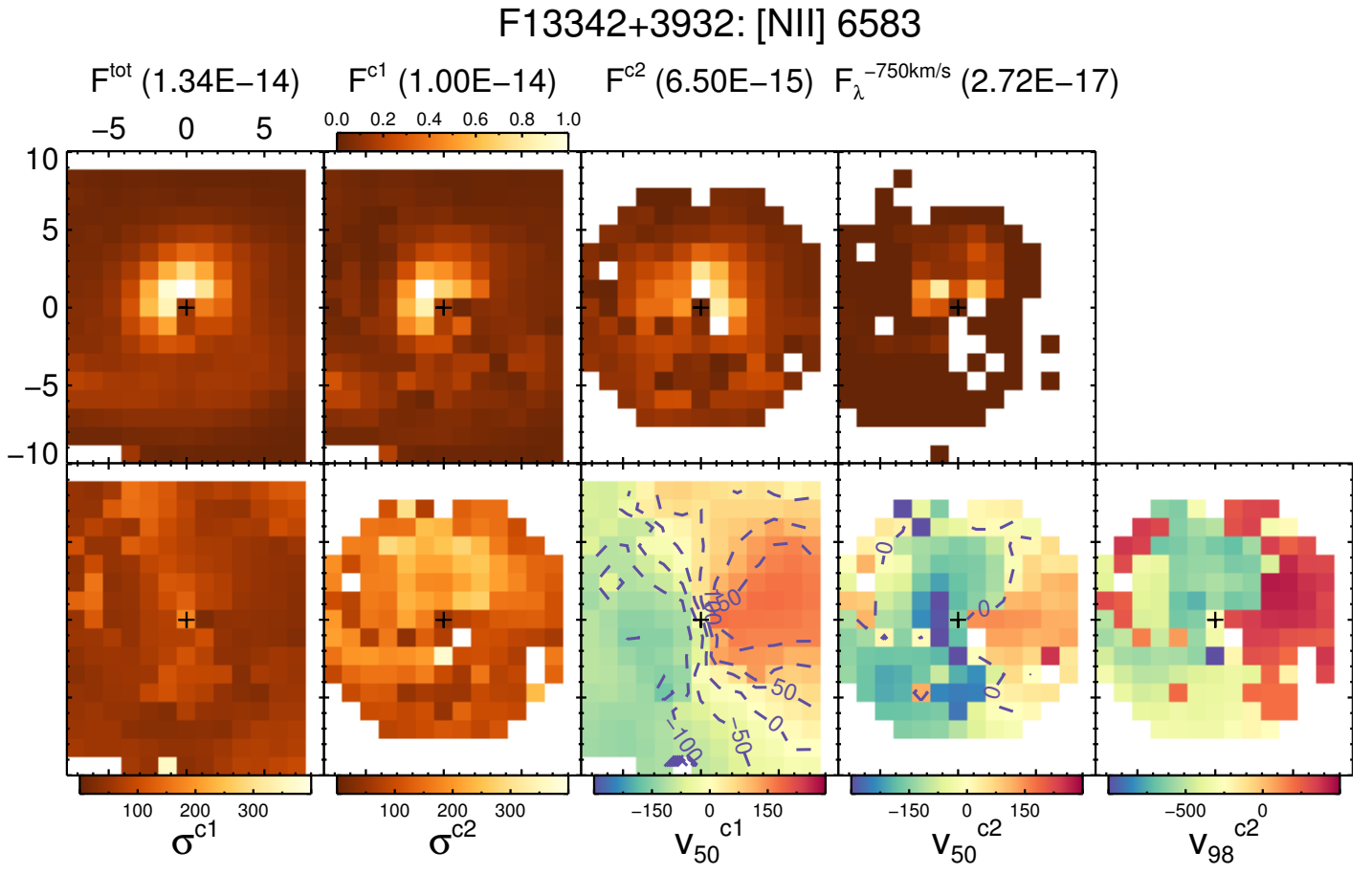
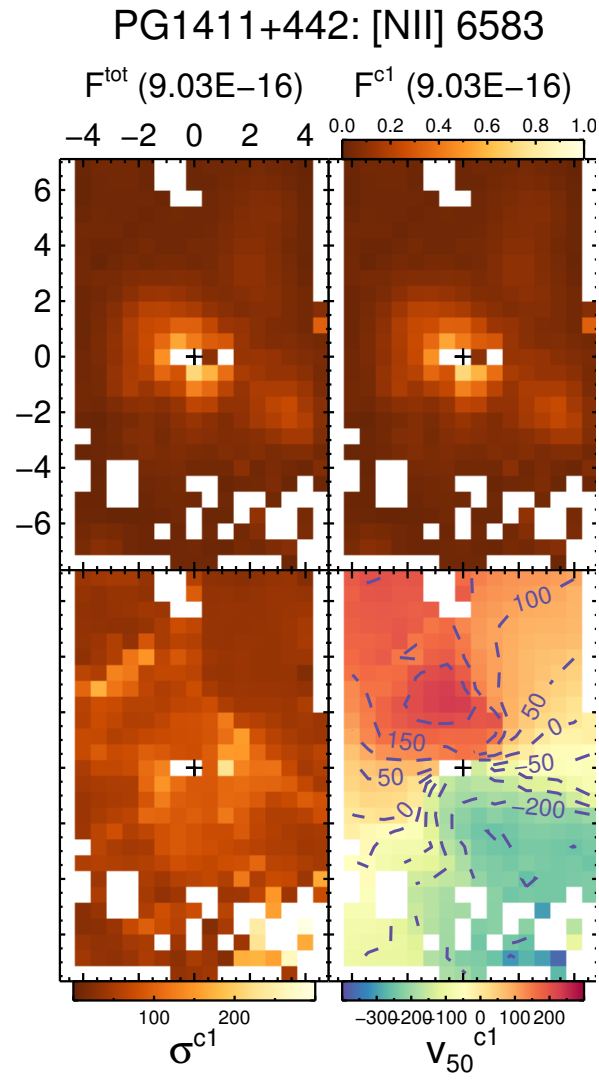
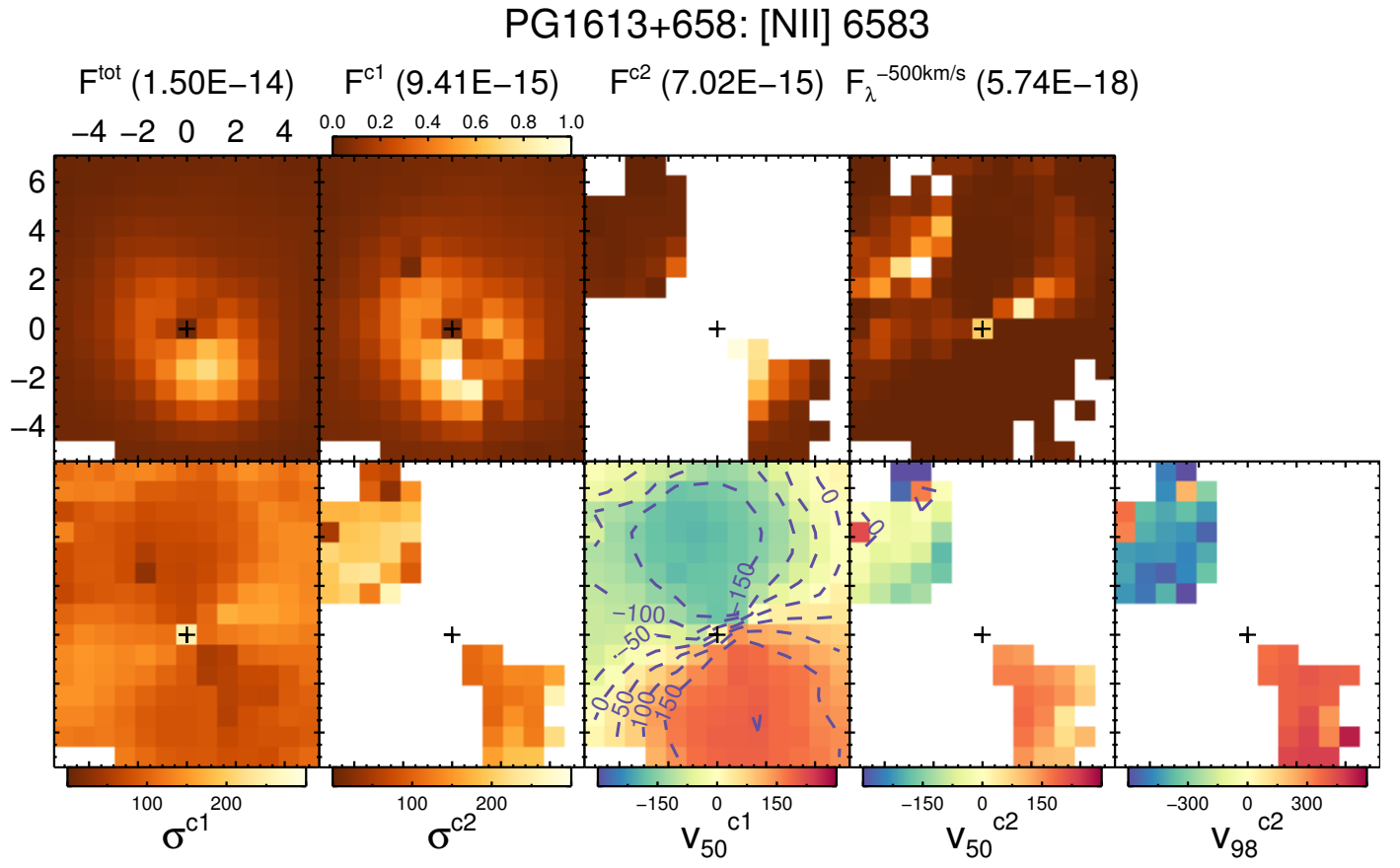
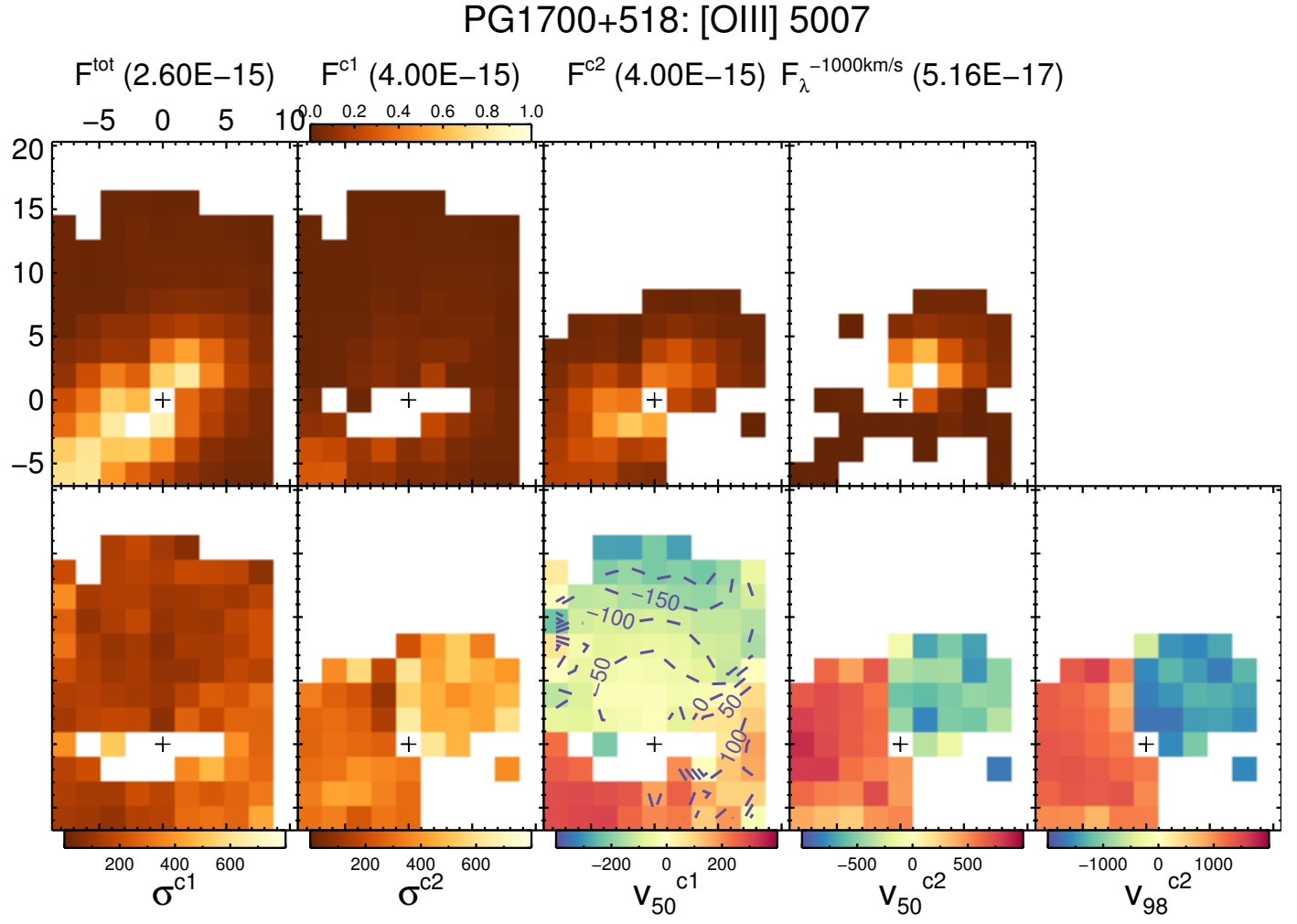


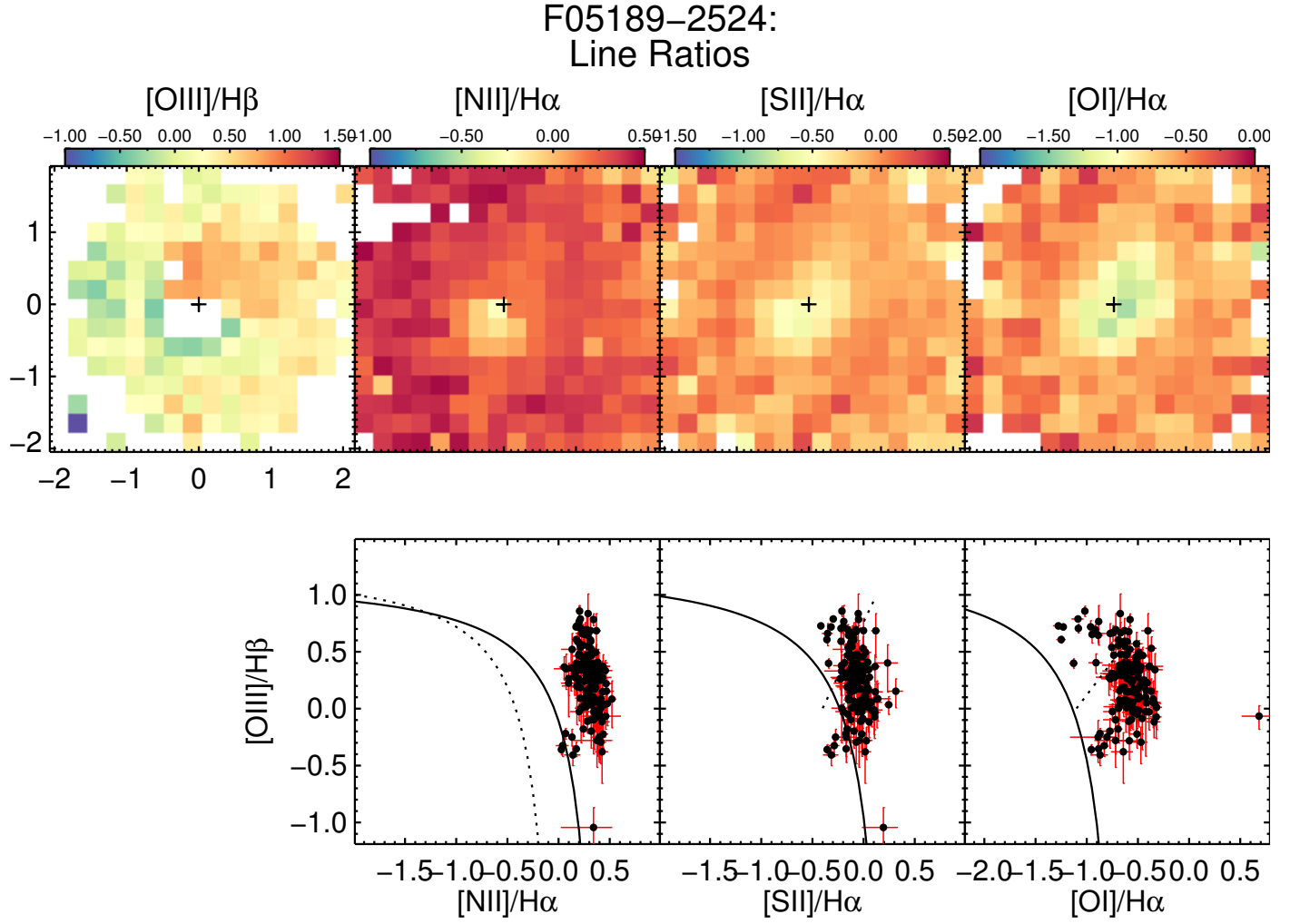
Figure 7. *Continued.*


 Figure 7. *Continued.*

Figure 7. *Continued.*


 Figure 7. *Continued.*

Figure 7. *Continued.*


 Figure 10. *Continued.*

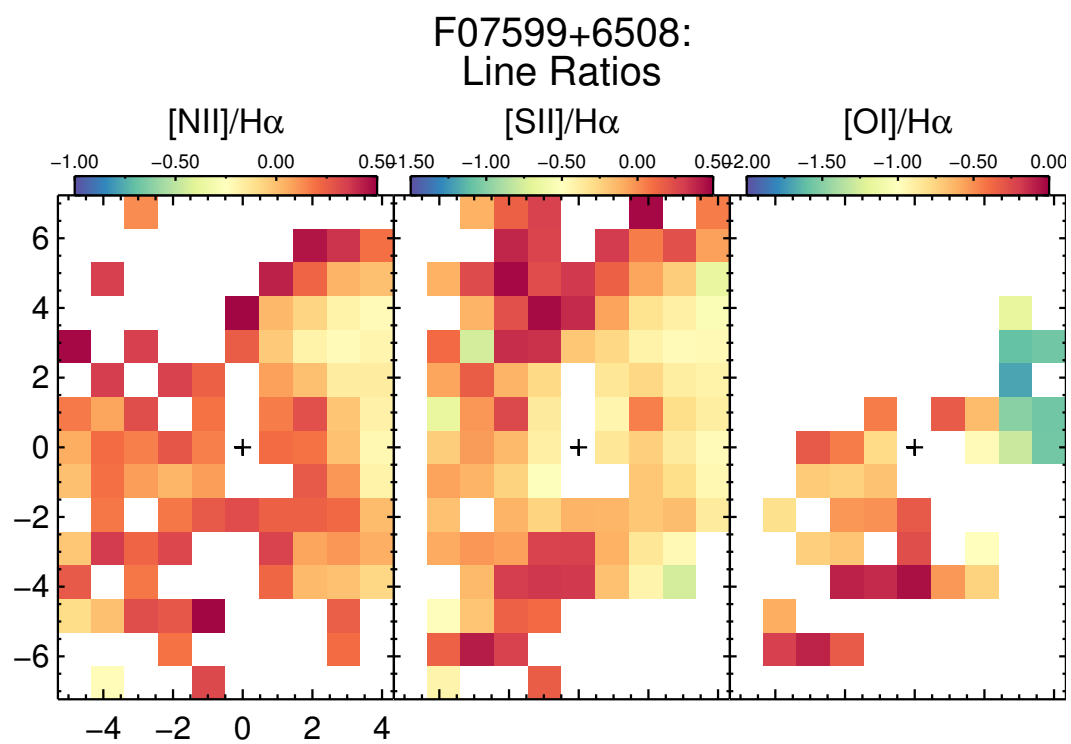


Figure 10. *Continued.*

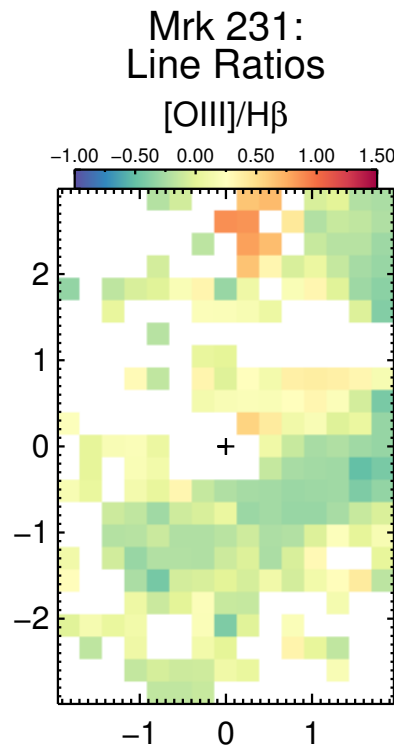
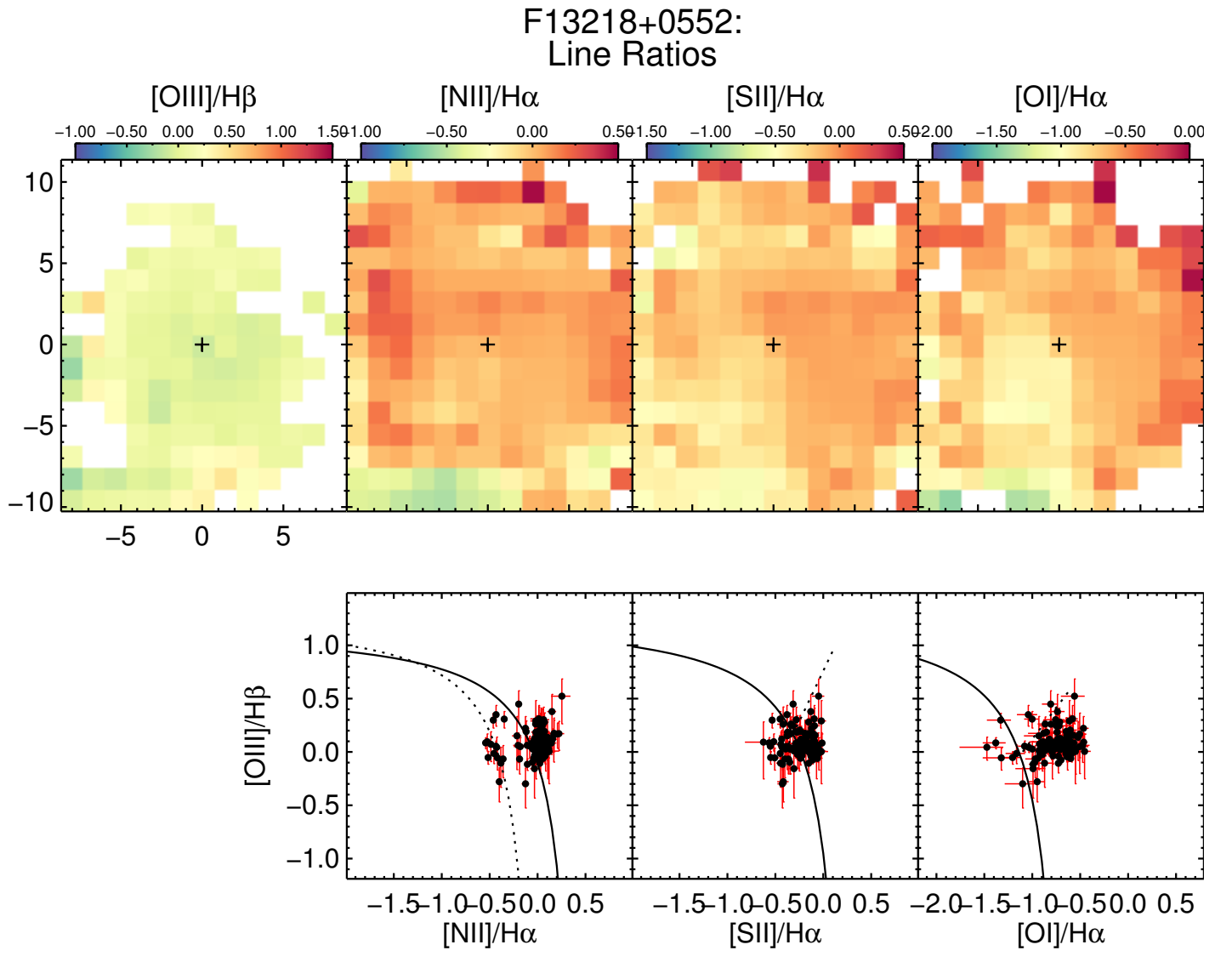


Figure 10. *Continued.*

Figure 10. *Continued.*

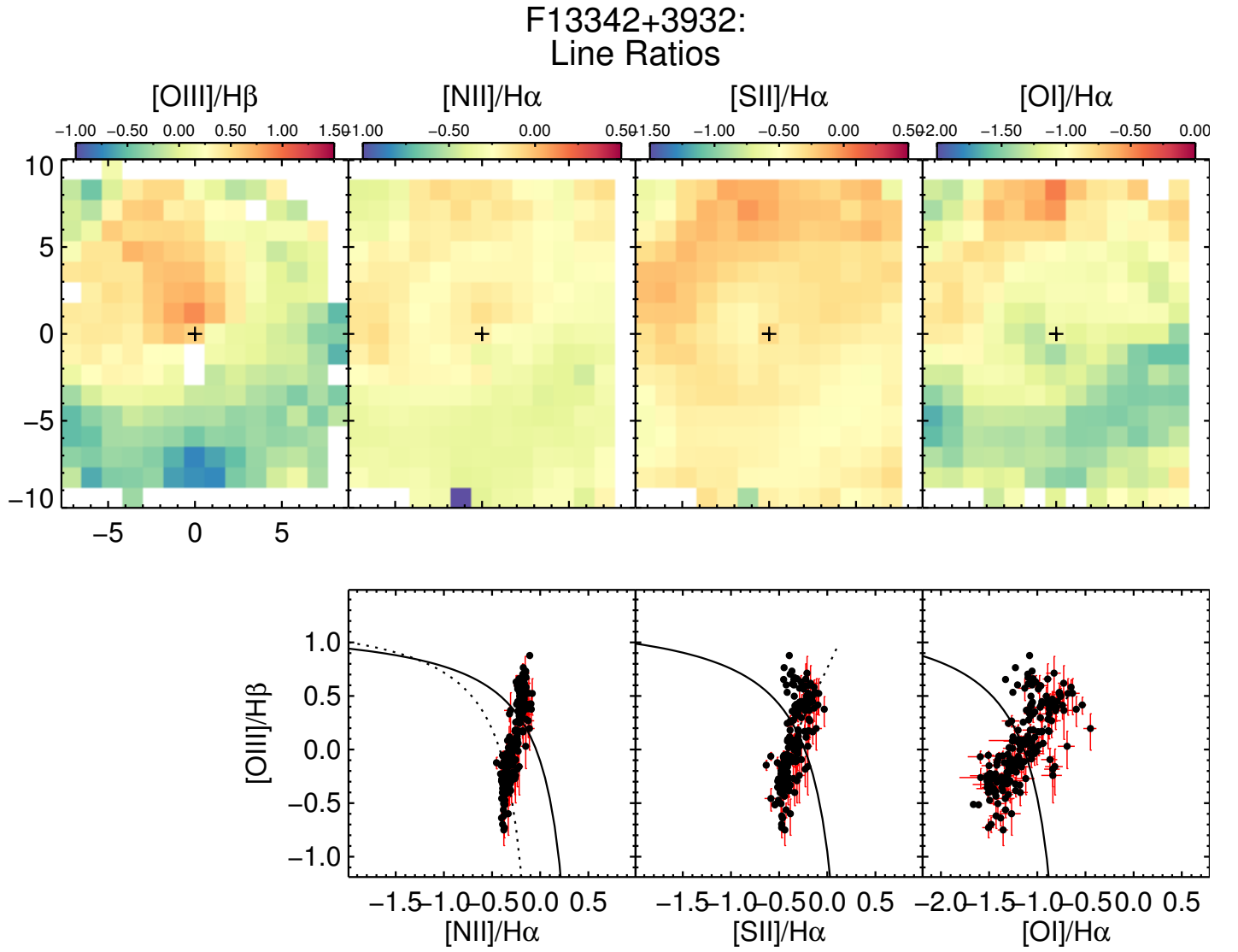
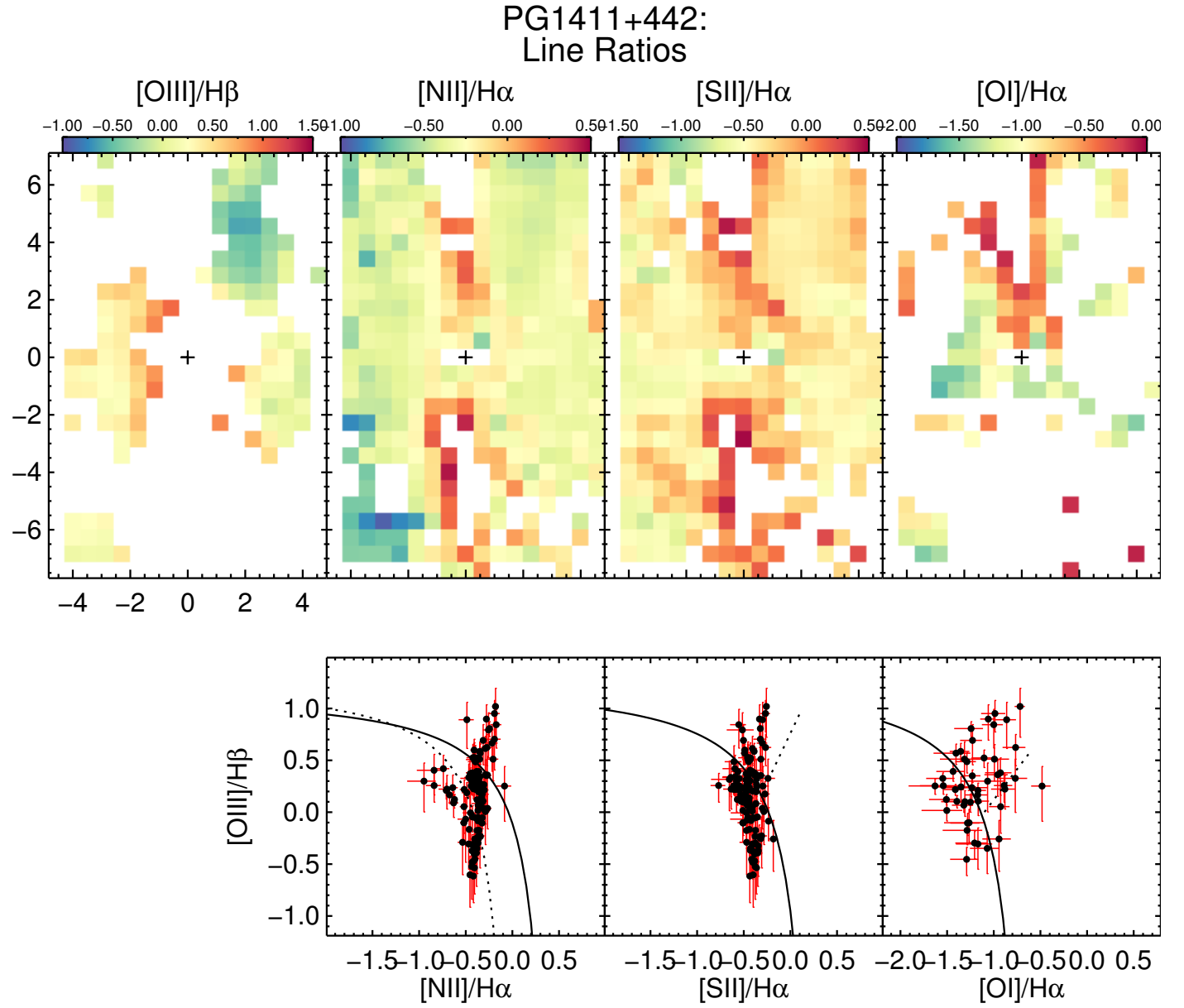
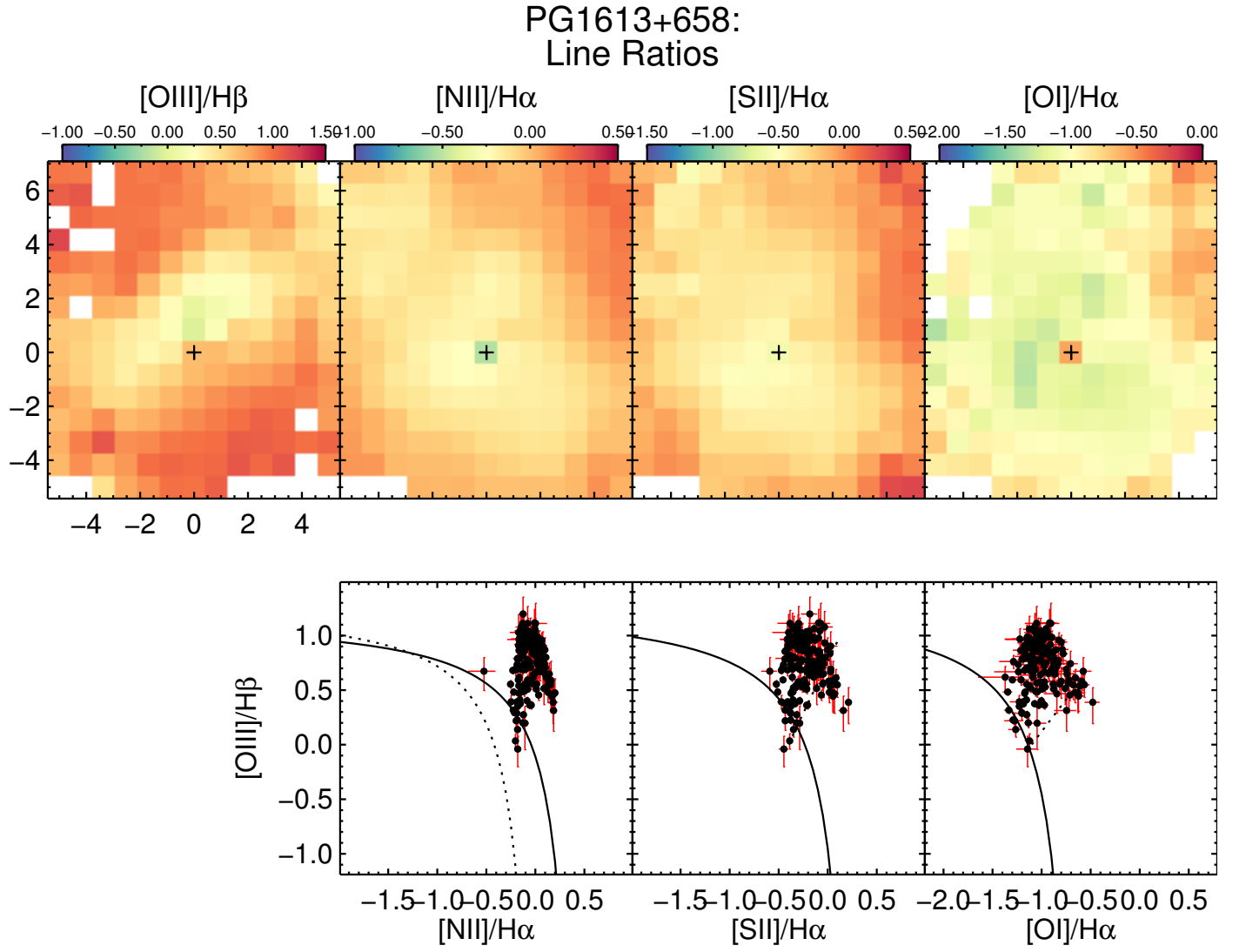


Figure 10. *Continued.*

Figure 10. *Continued.*


 Figure 10. *Continued.*

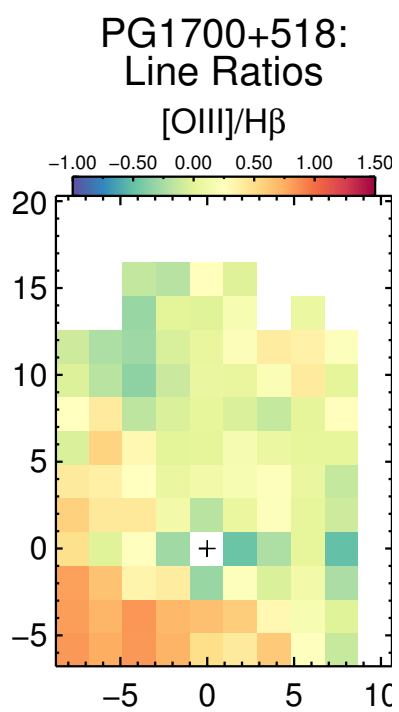
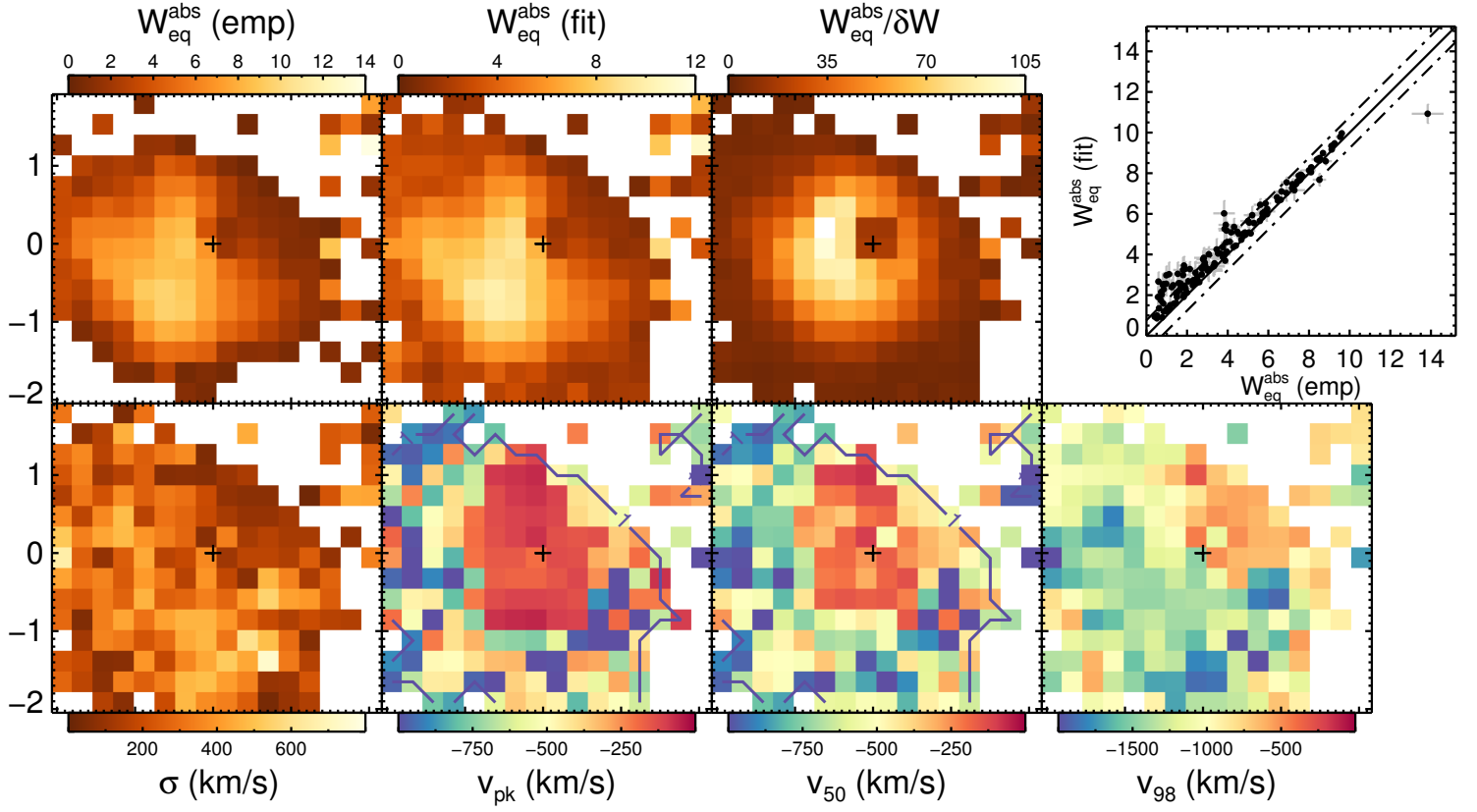
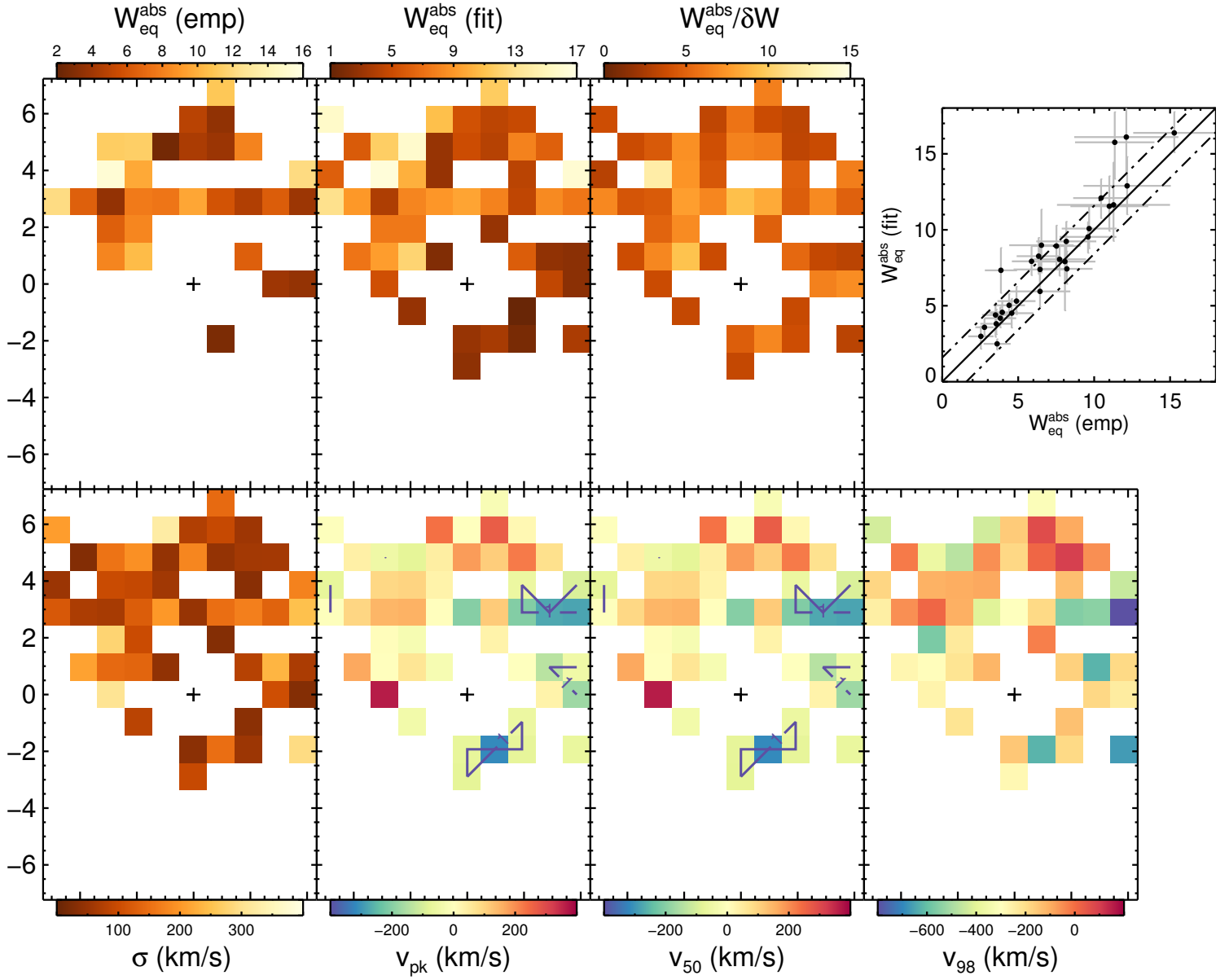


Figure 10. *Continued.*

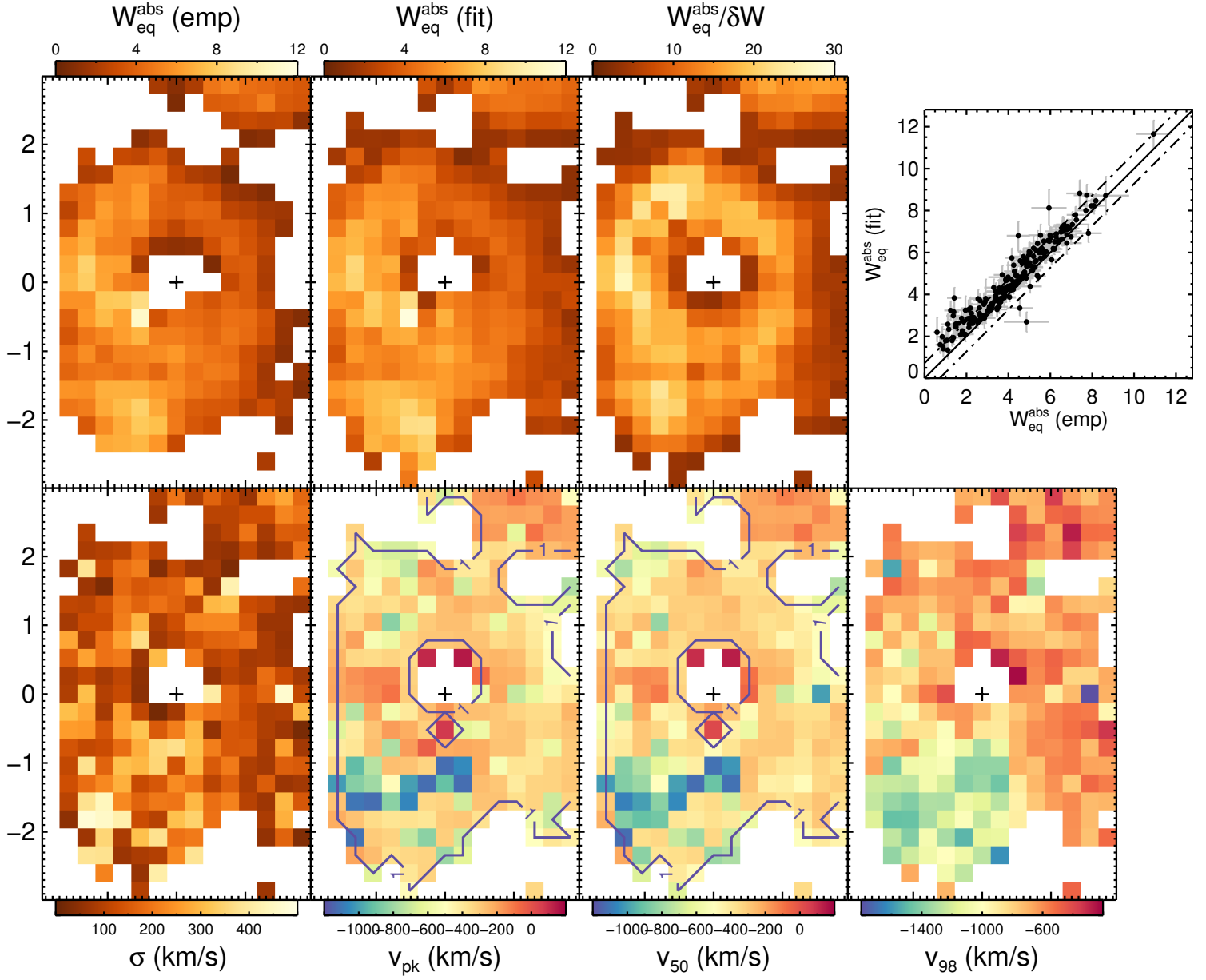
F05189–2524: NaI D absorption


 Figure 12. *Continued.*

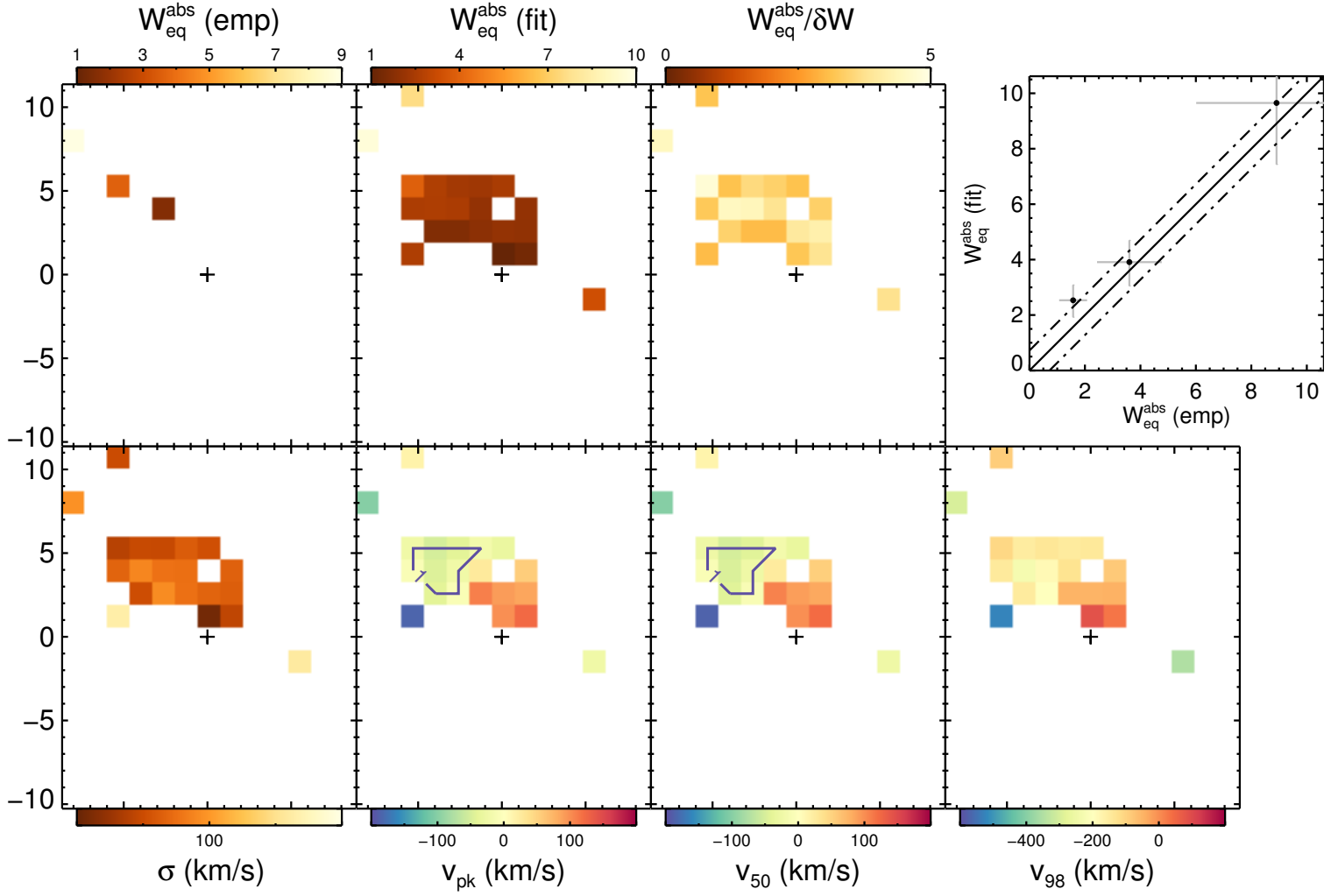
F07599+6508: NaI D absorption

Figure 12. *Continued.*

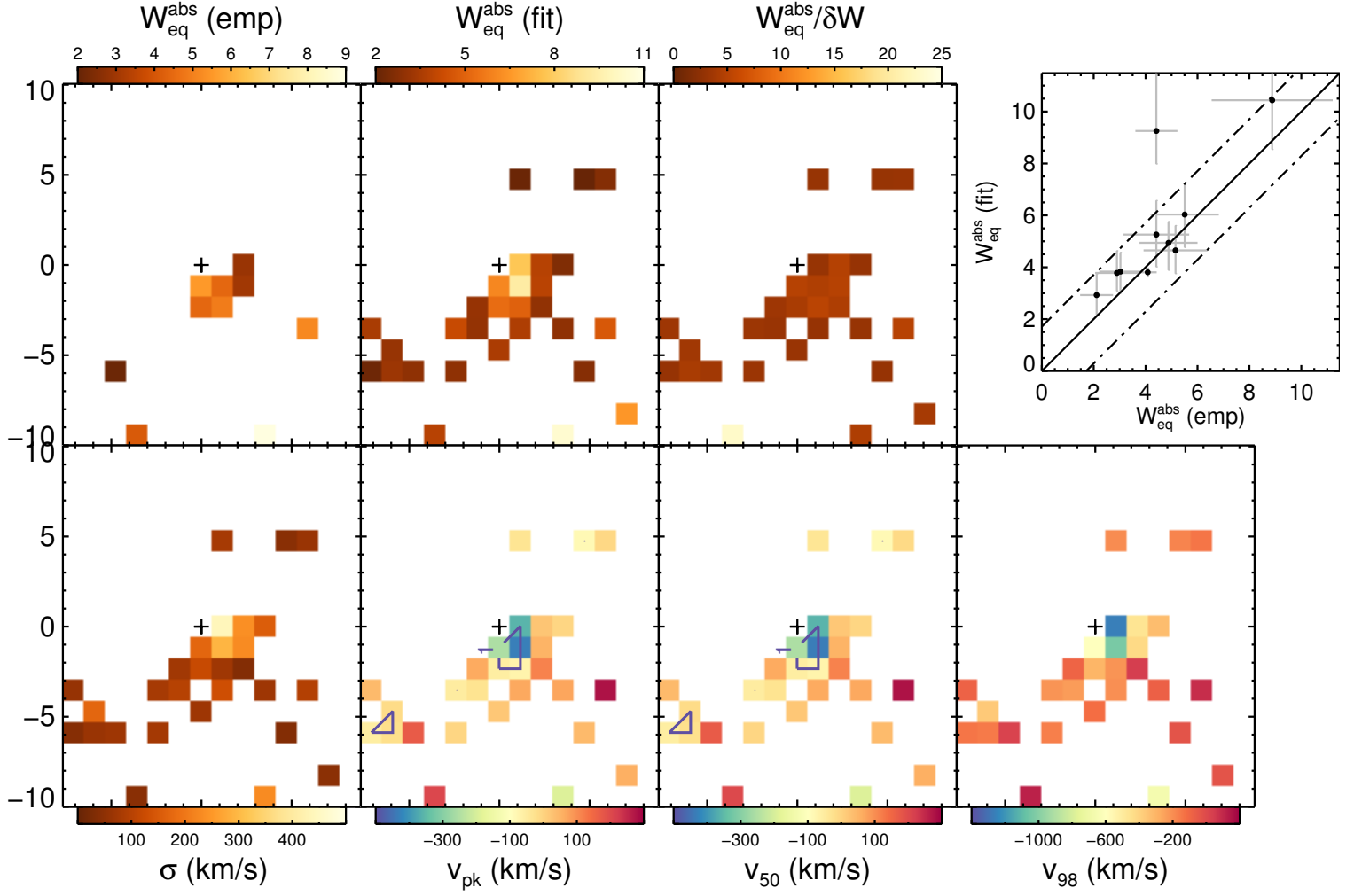
Mrk 231: NaI D absorption


 Figure 12. *Continued.*

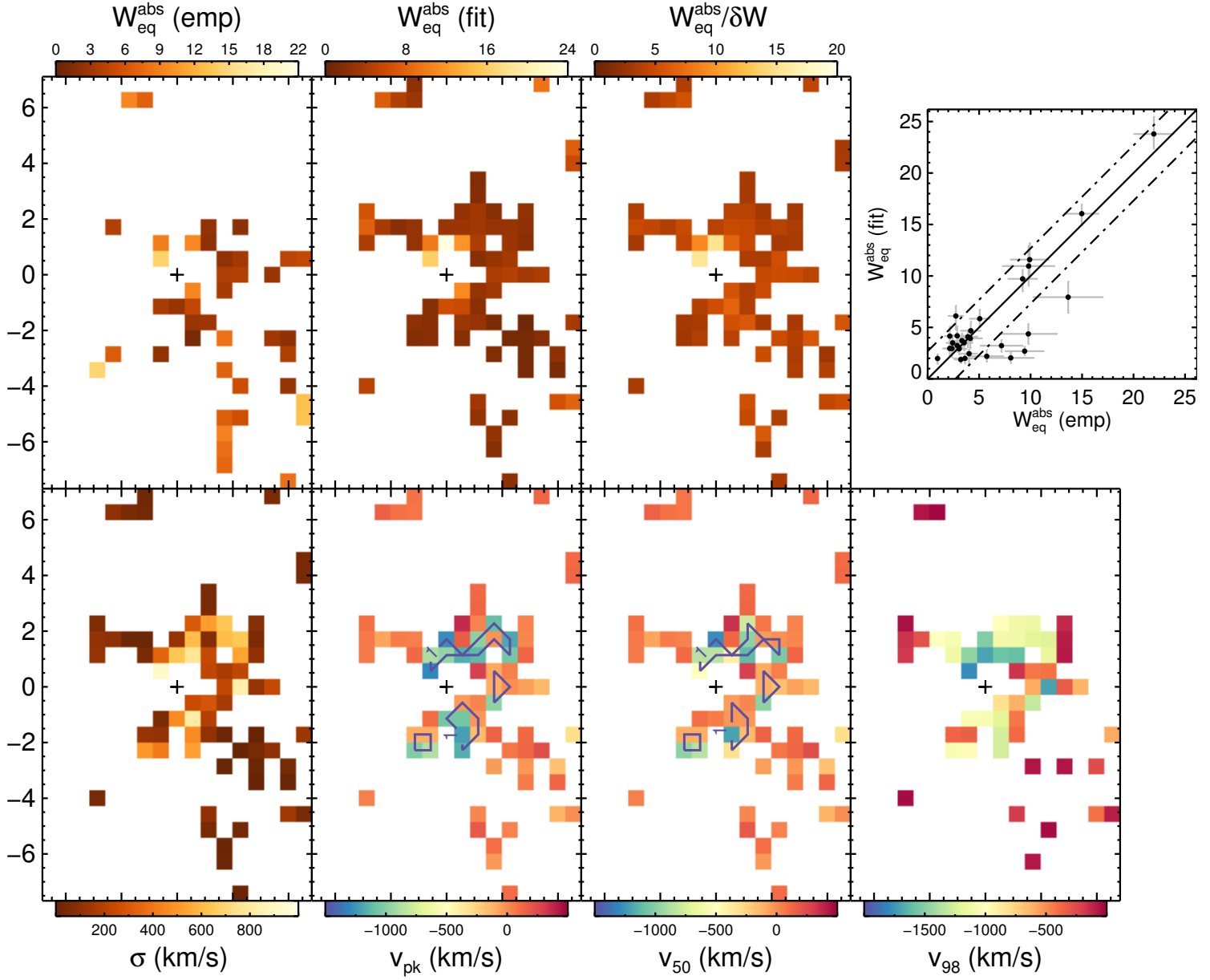
F13218+0552: NaI D absorption

Figure 12. *Continued.*

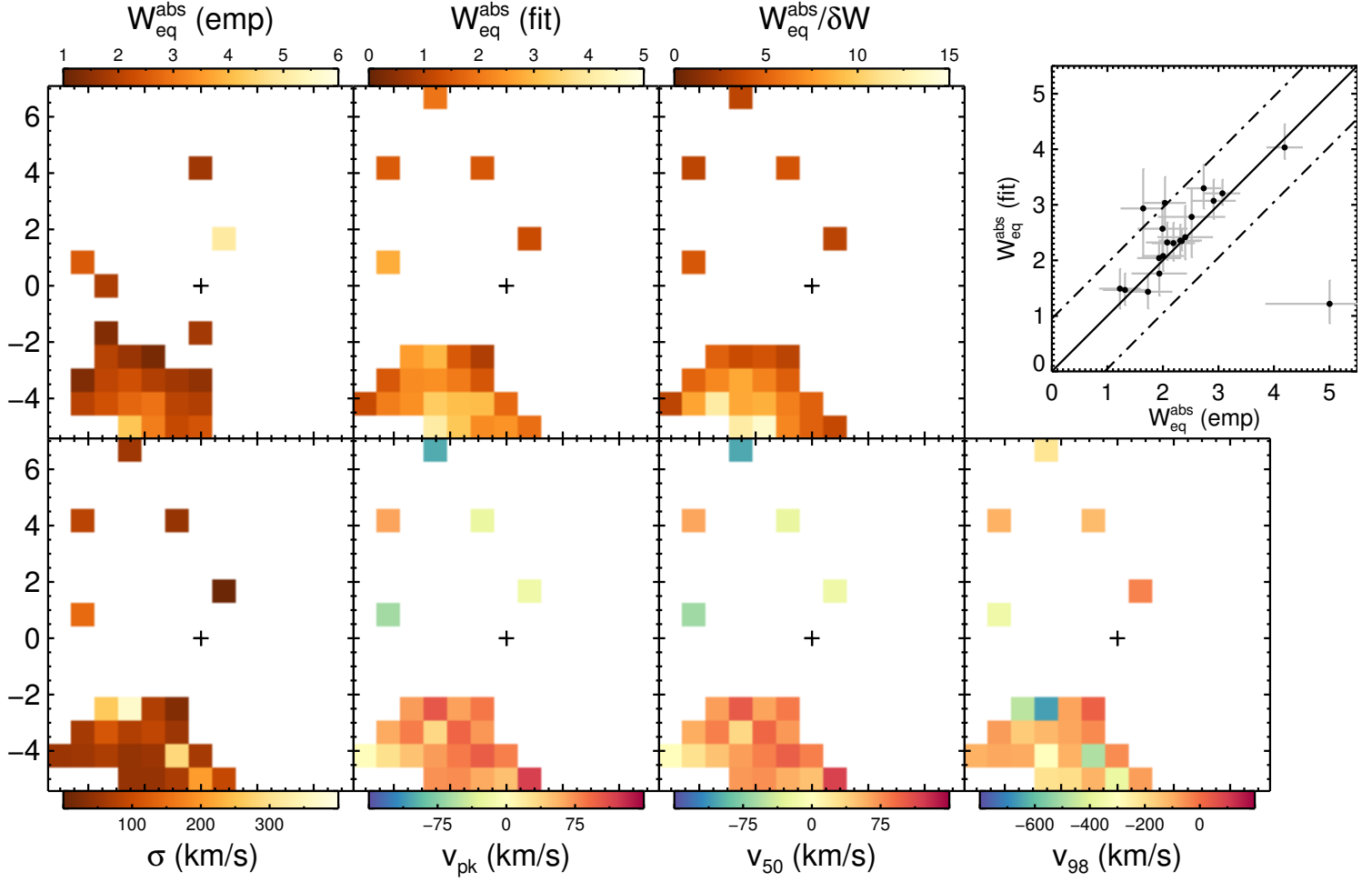
F13342+3932: NaI D absorption


 Figure 12. *Continued.*

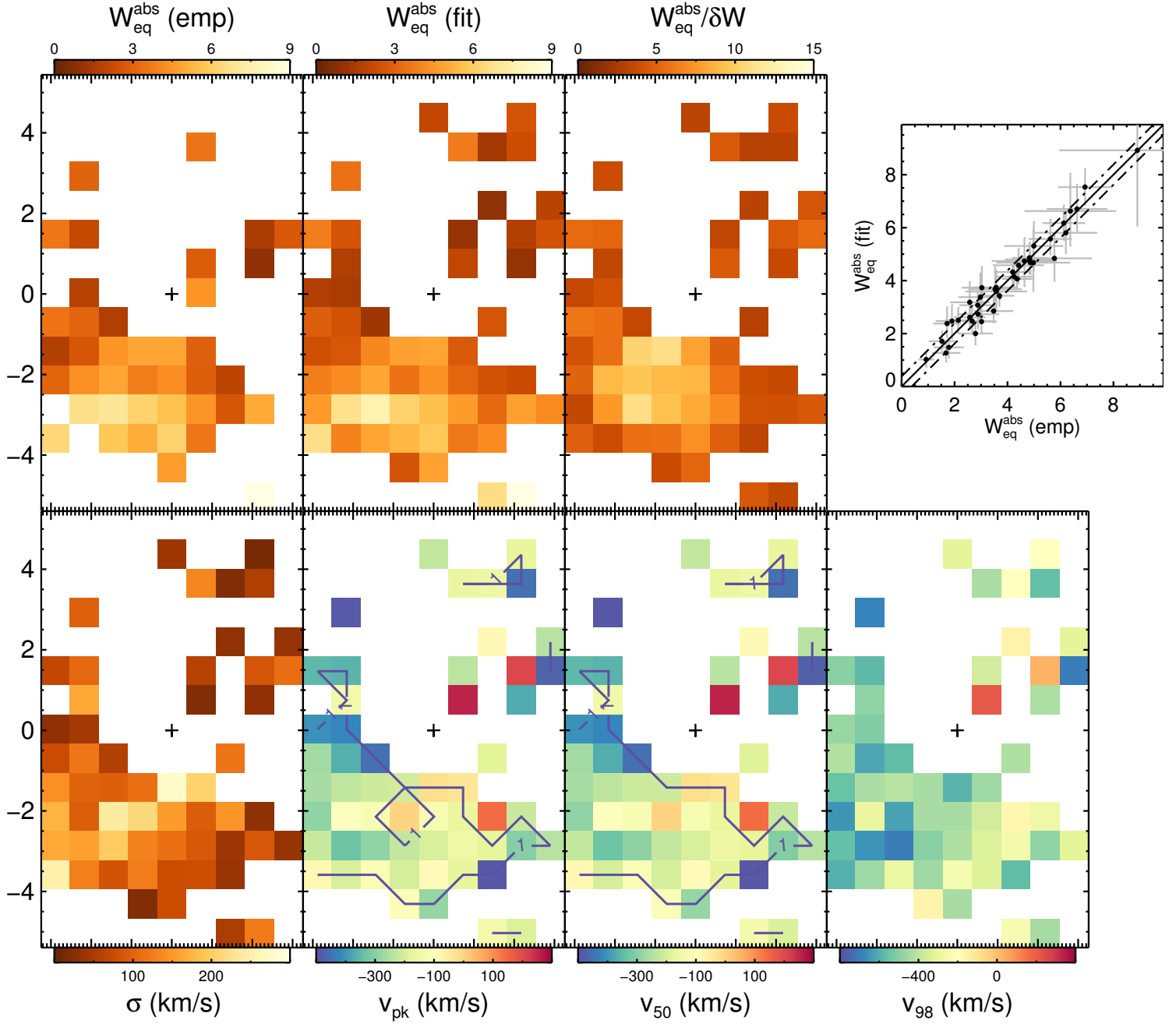
PG1411+442: NaI D absorption

Figure 12. *Continued.*

PG1613+658: NaI D absorption


 Figure 12. *Continued.*

F21219–1757: NaI D absorption

Figure 12. *Continued.*